


12-2017

Energy from Active Galactic Nuclei and the Effects on Host Spiral Galaxies

Amanda Schilling

University of Arkansas, Fayetteville

Follow this and additional works at: <http://scholarworks.uark.edu/etd>

 Part of the [Atomic, Molecular and Optical Physics Commons](#), [External Galaxies Commons](#), [Optics Commons](#), [Other Astrophysics and Astronomy Commons](#), [Other Physics Commons](#), [Physical Processes Commons](#), and the [Stars, Interstellar Medium and the Galaxy Commons](#)

Recommended Citation

Schilling, Amanda, "Energy from Active Galactic Nuclei and the Effects on Host Spiral Galaxies" (2017). *Theses and Dissertations*. 2599.

<http://scholarworks.uark.edu/etd/2599>

This Dissertation is brought to you for free and open access by ScholarWorks@UARK. It has been accepted for inclusion in Theses and Dissertations by an authorized administrator of ScholarWorks@UARK. For more information, please contact scholar@uark.edu, ccmiddle@uark.edu.

Energy from Active Galactic Nuclei and the Effects on Host Spiral Galaxies

A dissertation submitted in partial fulfillment
of the requirements for the degree of
Doctor of Philosophy in Physics

by

Amanda Schilling
University of Arkansas
Bachelor of Science in Physics, 2009
University of Arkansas
Master of Science in Physics, 2015

December 2017
University of Arkansas

This dissertation is approved for recommendation to the Graduate Council.

Dr. Julia Kenefick
Dissertation Director

Dr. Claud H. Lacy
Committee Member

Dr. William Oliver III
Committee Member

Dr. Paul Thibado
Committee Member

Dr. Tim Kral
Committee Member

Abstract

I have investigated the energy output of active galactic nuclei (AGN) in order to understand how these objects evolve and the impact they may have on host galaxies. First, I looked at a sample of 96 AGN at redshifts $z \sim 2, 3$, and 4 which have imaging and thus luminosity measurements in the *griz* and *JHK* observed wavebands. For these galaxies, I have co-epochal data across those bands which accounted for variability in AGN luminosity. I used the luminosity measurements in the five bands to construct spectral energy distributions (SED) in the emitted optical-UV bands for each AGN. I compared the SED to assumptions previously made about quasars and looked for correlations between SED and other AGN and galaxy properties. Second, I used spectra of the broad line region (BLR) of Type 1 AGN to estimate the mass of the central supermassive black hole (M_{BH}). I found a sample of Type 1 AGN that reside in spiral galaxies in order to explore the relationship between M_{BH} and pitch angle (ϕ), a measurement of how tightly wound the spiral arms are. Type 1 AGN offer a method to estimate M_{BH} at higher redshift than previous studies of the M_{BH} - ϕ relation. I was able to look at the evolution in the M_{BH} - ϕ relation which has implications for galaxy formation as well as AGN feedback.

Acknowledgements

I would like to thank my parents, Roy and Mary Schilling, for all of their encouragement and support that has brought me to this point in my journey: I am who I am in large part because of you both. You instilled in me a desire for knowledge and truth as well as justice and compassion — this world would be a better place if there were more people like you in it. I love you.

Thank you also to the rest of my family (I love you Angie, Jennifer, and Melinda!) and friends. Thank you for putting up with me over the last few years when I was stressed out and basically unavailable. I appreciate your understanding, particularly Tony Red who continuously reminded me that I was capable of getting this far.

Thank you to my fellow graduate students for studying with me and thank you for your friendship. Thank you to everyone in the AGES research group for exploring the universe with me especially Scott Barrows who taught me some of the nuts and bolts of analyzing AGN and galaxy data.

Thank you to everyone on my doctoral committee for your feedback, wisdom, and support. Dr. Oliver, you made me feel that I made you proud. Dr. Thibado, you insisted that I do my best work.

And above all, I want to thank my advisor, Dr. Julia Kennefick, for everything she has given me in the last several years. Not only did she share her knowledge of physics, astronomy, research, and academia but she let me find my own way. Under her guidance I learned to trust my own judgement. Under her care I came to believe I was capable ‘doing science’ and finally accepted that I am a scientist. Dr. Kennefick also helped me face my

shortcomings — I will never forget when you said to me “Well, don’t stress about stressing.” I may always be nervous and feel intimidated when I speak in front of people (especially about my research) but it is because of you that I know it is okay. I am forever grateful to you, Julia.

Contents

1	Introduction	1
1.1	Active Galactic Nuclei	2
1.1.1	Black Hole and Accretion Disk	3
1.1.2	Broad Line Region	4
1.1.3	Narrow Line Region	7
1.1.4	Spectral Energy Distribution	8
1.2	AGN and Host Galaxies	13
1.2.1	Spiral Galaxies and Density Wave Theory	15
1.2.2	Pitch Angle Measurement	17
1.3	Summary	19
	Bibliography	20
2	The Optical-UV Spectral Index of Quasars	22
2.1	Abstract	22
2.2	Introduction	22
2.3	Sample and Data	24
2.3.1	Observation and Image Reduction	25
2.3.2	Photometry	26
2.4	Optical-UV Spectral Index	28
2.5	Corrected M_i Absolute Magnitudes	34
2.6	Conclusion	36
	Bibliography	40

3	The Co-Evolution of Galaxy Disks and Type 1 AGN	41
3.1	Abstract	41
3.2	Introduction	41
3.3	Sample	44
3.4	Methods	47
3.4.1	Mass Estimates	47
3.4.2	Pitch-Angle Measurements	49
3.5	Results	52
3.5.1	The $M_{BH}-\phi$ Relation	54
3.5.2	The Fundamental Plane of Disk Galaxies	57
3.6	Discussion	60
3.6.1	What are we seeing?	60
3.6.2	Implications	64
3.7	Conclusion	65
	Bibliography	88
4	Conclusion	91
	Bibliography	94
	Appendix A Image Processing	95
A.1	Image Reduction	95
A.2	Astrometry	99
A.3	Photometry	101
	Bibliography	103

Appendix B Type 1 AGN Spectra	104
B.1 Flux Calibration	104
B.2 Measurements	107
B.3 Error Propagation	111
Bibliography	114

List of Figures

1.1	AGN Schematic	2
1.2	AGN optical-UV spectrum — Composite AGN spectrum assembled from quasars in the Sloan Digital Sky Survey.	4
1.3	Spectral Energy Distributions — the SED of two well studied AGN - 4C 34.47 (top) and Mrk 586 (bottom).	9
1.4	Power Law Spectrum from Synchrotron Emission — emission from a single electron (upper) and the sum from a distribution of synchrotron emitting electrons (lower).	11
1.5	Correcting for Redshift — response curve of the SDSS <i>r</i> -filter (right) and the effective filter after correcting for observing objects at $z = 1, 2,$ and 3 overlaid on a composite AGN spectrum.	13
1.6	Hubble’s Tuning Fork — classification of galaxies by morphology.	14
1.7	Local Mass-Pitch Angle Relation — established using a sample of 34 spiral galaxies with directly measured black hole mass.	15
1.8	Spiral Density Waves — left: NGC 3344 (Photo by Adam Block/Mount Lemmon SkyCenter/University of Arizona) compared to, right: cartoon of density wavefronts moving through a rotating disk.	16
1.9	Logarithmic Spiral in Polar Coordinates	17
1.10	2D FFT output — pitch angle as a function of inner radius for modes $m = 1 - 6$	18

2.1	Sampled wavebands — central wavelength of observed filters compared to the rest-frame wavebands in each redshift bin. The emitted B -band is marked for each redshift.	24
2.2	Distribution of spectral index for the co-epochal sample (left) and the SDSS–2MASS sample (right)	29
2.3	Distribution of α_o in each redshift bin in the co-epochal sample. The bold line represents the median, the box ends are the Q_1 and Q_3 quartile points, the bars are the most extreme points that are not outliers, and the points are the outliers; an outlier is defined as any point whose value is more than $3/2$ the interquartile range, $IQR = Q_3 - Q_1$	31
2.4	Spectral Index as a Function of Redshift — α_o measurements of the 95 quasars in this sample as well as 45 quasars from KB08; the average from each redshift bin are shown as a black triangles and are $\alpha_o(z = 1.88) = -0.62$, $\alpha_o(2.80) = -0.61$, and $\alpha_o(4.06) = -0.67$; the line is a least-squares fit with the equation shown at bottom-right.	32
2.5	Spectral Index as a Function of Redshift (all) — colored circles are quasars from the co-epochal sample and include KB08 data, black points are the SDSS–2MASS sample, bottom plot shows the distribution in redshift of quasars in the SDSS–2MASS sample.	33

2.6	Comparison i-band Magnitude Calculations — the x-axis is represents M_{i,α_o} , the magnitude calculated using α_o and the y-axis is $M_{i,\alpha_{0.5}}$, the magnitude calculated using the traditional value $\alpha = -0.5$; blue points are quasars in the $z \sim 1.88$ bin, green are $z \sim 2.80$, and red are $z \sim 4.07$; solid black line represents the $M_{i,\alpha_o} = M_{i,\alpha_{0.5}}$ line.	35
3.1	Redshift distribution — SDSS-selected sample with imaging and spectra from SDSS in salmon; SDSS-selected sample with imaging from WIYN and spectra from SDSS in green; <i>HST</i> sample in blue.	45
3.2	B-band image of NGC1337; left: observed image, center: semimajor axis aligned with the y-axis, right: deprojected image; ellipse and circle overlays are a visual aid only; i.e. not fit to galaxy	49
3.3	Examples of galaxies from this sample that show the difficulty of deprojection; note the prominence of the spiral arms and lack (above the sky) of light from the disk in all the images; objects clockwise from upper left: <i>HST</i> 14, <i>HST</i> 5, SDSS 7, and SDSS 3. See Table 3.3 for images of each galaxy in the sample	50
3.4	$M_{BH}-\phi$ — Mass as a function of pitch angle for all spiral, Type 1 AGN: triangles are from the SDSS-selected sample with imaging and spectra taken from SDSS, squares are from the SDSS-selected sample with imaging from WIYN and spectra from SDSS, circles are from the Hubble sample with imaging from HST and spectra from various sources (see Table 3.2) for details about sources); the solid line is a linear least-squares fit to the entire spiral-AGN sample.	53

3.5	$M_{BH}-\phi$ z-bins — mass as a function of pitch angle divided into three equal sized redshift bins; objects in each bin were fit to a weighted least squares fit.	55
3.6	$M_{BH}-\phi$ Local and AGN samples — Comparison of mass as a function of pitch angle for the two samples — black circles represent the Type 1 AGN and the purple squares represent the local sample.	56
3.7	$\Sigma_{H_I}(M_{bulge})$ — density of neutral hydrogen in the disk as a function of bulge mass for each redshift bin; solid lines were calculated by converting M_{BH} to M_{bulge} , using the $M_{BH}-\phi$ fits from Figure 3.4 to get pitch angle as a function of M_{bulge} , and using the fundamental plane to find disk density.	59
3.8	Pitch angle distribution — binned histogram of pitch angle measurements for the type I AGN sample: grey; the empirical density function for the Type 1 AGN sample: dashed, red line; for comparison, the probability density function (PDF) for a complete, local sample: solid, blue line.	61
3.9	Simulated Galaxies — galaxies created using GALFIT which were rotated and stretched and had Poisson noise added to simulate real galaxy properties.	63
3.10	Type 1 AGN spectra	80
3.10	Type 1 AGN spectra (continued)	81
3.10	Type 1 AGN spectra (continued)	82
3.10	Type 1 AGN spectra (continued)	83
3.10	Type 1 AGN spectra (continued)	84
3.10	Type 1 AGN spectra (continued)	85
3.10	Type 1 AGN spectra (continued)	86
3.10	Type 1 AGN spectra (continued)	87

A.1	Dark Frames — Turning on the detectors but not exposing them to light produces dark frames. Dark frames reveal the noise of the individual pixels. .	96
A.2	Sky Frames — Sky frames, ideally, should be images taken of the sky with no objects (such as stars) present in the field. In this case we averaged several frames that had objects in them to use as sky frames so long as the objects present were offset enough between frames to not survive in the averaging. .	97
A.3	Flat Frames — Flat frames, again ideally, are obtained by exposing the detector to a source of light with uniform, known energy. Flat frames reveal the gain ratio of photons hitting the detector to the number actually recorded for each pixel. As with the sky frames, we used object frames to make the flats by dividing each pixel in a frame by the median pixel value for that frame. (An actual flat frame is the average of many flats.)	98
A.4	Image Reduction — example of a raw frame (left) and the same frame after image reduction (right).	99
A.5	Combination of Dithered frames	100
B.1	Pseudo System for Flux Calibration — black, solid line: throughput curve for the DEIMOS spectrograph (https://www2.keck.hawaii.edu); red, dashed line: <i>R</i> -filter response curve from Canada-France-Hawaii Telescope CFH12k’s filter (http://www.cfht.hawaii.edu).	106

B.2 **Continuum plus emission line fit** — The spectrum data is in black, total model fit in red (continuum, two broad $H\beta$ Gaussians, one narrow $H\beta$, and two Gaussians for each of the [O III] lines), and, for emphasis, the two broad $H\beta$ components are plotted separately in blue and green. 111

Chapter 1

Introduction

By the beginning of the twentieth century astronomers were familiar enough with the spectra of galaxies (then identified only as nebula) to recognize them as the sum of the energy from all the stars in that galaxy (Fath, 1909). So when Seyfert (1943) began to look at a group of galaxies with powerful emission lines in their spectra, he realized they were unique objects. Seyfert galaxies, as they are now known, have a nucleus that emits as much energy as all stars in the galaxy and from an unresolved volume of space. Decades later, Maarten Schmidt (1963) solved a mystery that had been baffling astronomers - objects known to be radio sources and which appeared as stars (point like) emitted optical spectra with emissions lines that were not identifiable. What Schmidt realized is that one of these objects, 3C 273, is incredibly far away and thus the emission lines were not from some rare element but hydrogen Balmer lines redshifted by $z = 0.158$. 3C 273 belongs to a class of objects known as quasars – short for quasi-stellar radio sources – and, like Seyfert galaxy nuclei, are known for their high luminosity. Quasars emit hundreds of times the radiation of Seyfert galaxy nuclei and have been detected out to redshifts above $z \sim 7$ (Mortlock et al., 2011) but these objects are not found in the local Universe. Seyfert galaxy centers and quasars are two types of active galactic nuclei (AGN) and the discovery of these objects led to two important conclusions: (1) the amount of energy that is emitted from a small volume of space in AGN is powered by gravitational collapse, and (2) the fact that quasars were once abundant in the Universe but are not now shows that the Universe is changing with time. The evolution of the Universe as evidenced by changing quasar numbers led to

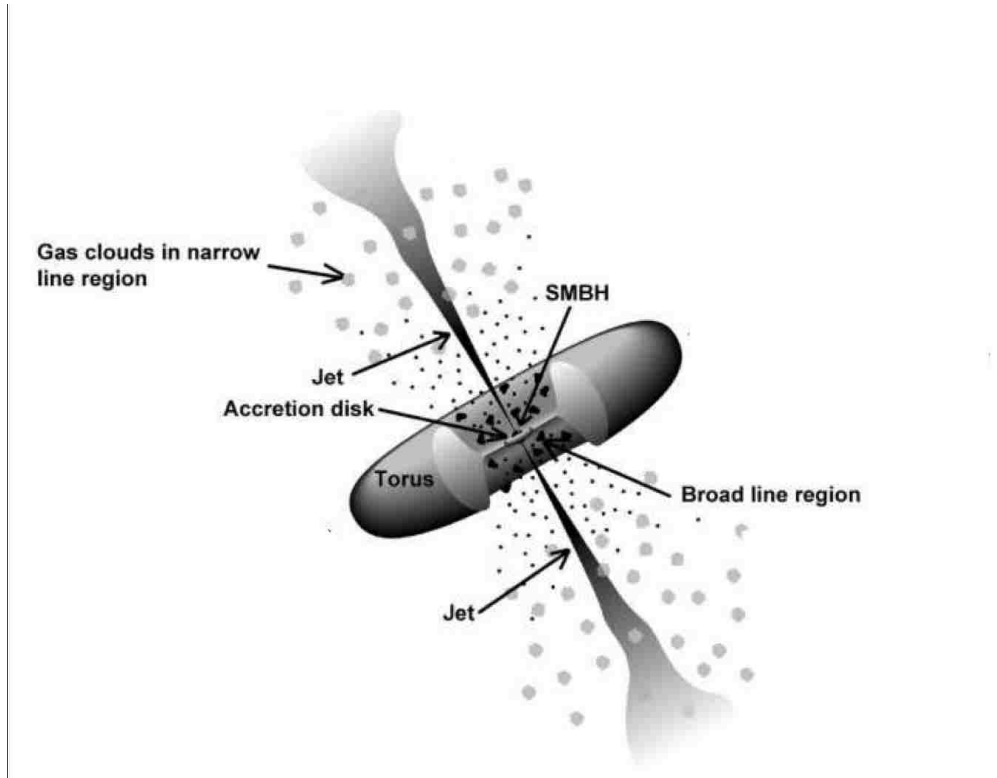


Figure 1.1: **AGN Schematic** — <https://fermi.gsfc.nasa.gov/science/eteu/agn/>

the dismissal of the the steady-state theory (Hoyle, 1948), a leading rival to the big-bang theory in the 1950s, which posited the perfect cosmological principle that the observable Universe is homogeneous, isotropic, and constant with time. Since these discoveries, AGN have been necessary in the narrative of cosmic and galaxy evolution and understanding the physical processes that govern AGN phenomenon has been a primary focus in astronomy.

1.1 Active Galactic Nuclei

Since Seyfert's and Schmidt's discoveries, studies have led to a consensus among astronomers that AGN, known for emitting large amounts of radiation from the centers of some galaxies, are supermassive black holes (SMBHs) in the process of accreting gas and other material from the galaxy. All of the radiation – radio wavelengths to X-rays and

γ -rays – can be explained as an effect of this accretion process. Figure 1.1 shows a schematic of the different components of an AGN - the black hole and accretion disk in the center surrounded by clouds of hot gas in the broad line region, a torus of cooler gas and dust that obscures some components of the AGN depending on the viewing angle, jets that extend out perpendicular to the accretion disk, and clouds of gas in the narrow line region. In this chapter, I will focus on several properties of AGN and galaxies and the theories and physical processes as they relate to this work.

1.1.1 Black Hole and Accretion Disk

We have found evidence for the existence of black holes at the center of almost every large galaxy that has been examined including the Milky Way and recently even at the center of some dwarf galaxies (Ahn et al., 2017). SMBHs are much larger than stellar black holes and are found to range in mass from around 10^6 to 10^{10} times the mass of the sun (M_{\odot}) and occupy a volume of space that has a radius of fractions of a parsec (10^{-6} to 10^{-5} pc). Compare this to the size of galaxies which are tens of kiloparsecs across.

The material falling into a SMBH will form an accretion disk. Observations of AGN spectra constrain the accretion disk to have a radius of around 10^{-3} to 10^{-2} pc. Due to the small size, it has been difficult if not impossible to resolve in most cases. Observed spectra can be explained as some combination of thermal and synchrotron radiation emitted from the disk. The thermal radiation is the result of viscosity in the disk which removes angular momentum from particles so that they can fall into the black hole. And the ionized plasma in orbital motion around the black hole will cause synchrotron radiation. The exact processes involved in accretion onto a SMBH are not presently well understood given the

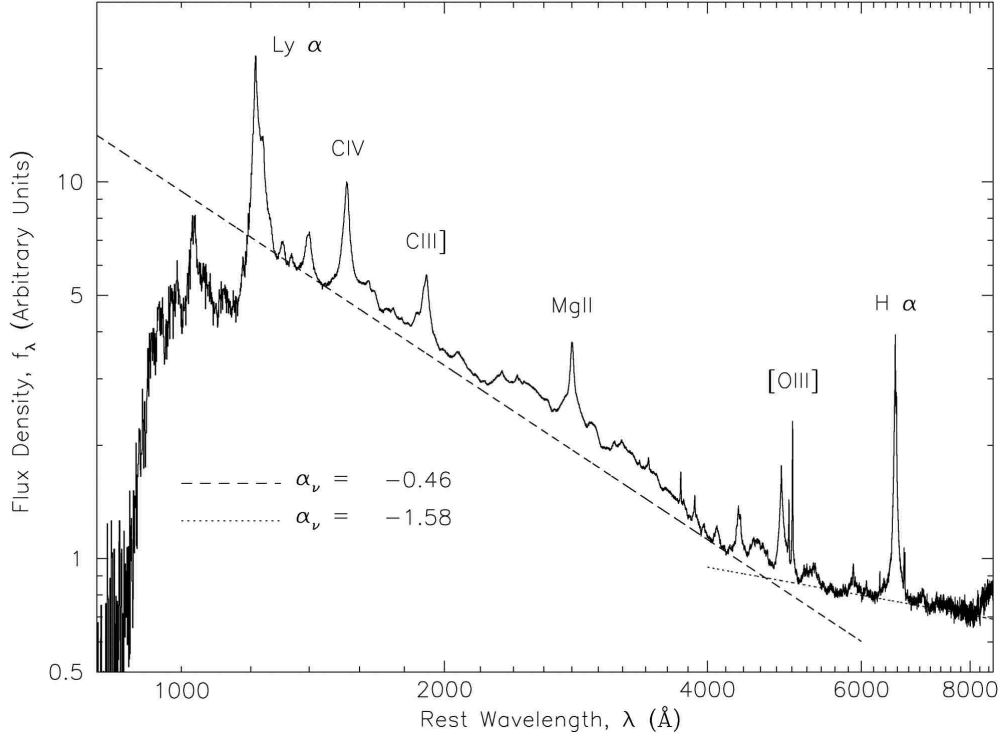


Figure 1.2: **AGN optical-UV spectrum** — Composite AGN spectrum assembled from quasars in the Sloan Digital Sky Survey (Vanden Berk et al., 2001).

lack of imaging – different models of an accretion disk depend on viscosity, thermal instabilities, types of photon scattering that occur, and also the shape and density of the disk itself.

1.1.2 Broad Line Region

The broad line region (BLR) contains clouds of dense gas that are gravitationally bound to the SMBH at a radius of 0.1 to 1pc. Ionizing radiation from the accretion disk is reprocessed in the BLR as evidenced in the broad emission lines of optical-UV spectra.

Figure 1.2 shows some common emission lines associated with the BLR - CIV, MgII, H α , and (not marked) FeII emission around the MgII and [OIII] lines. The broadening of the emission lines is assumed to be Doppler broadening - photons are redshifted as they move

away from our detectors and blueshifted as they move toward - due to orbital motion. Thermal broadening is small in comparison. BLR emission lines, traditionally reported as velocities of the full width at half maximum (FWHM), can range from 500 to 5000 km/s. In general, emission lines are fit with Gaussian profiles when the luminosity and/or width of the lines is of interest. This first approximation is adopted due to small signal to noise ratio in the spectra. The profile of the emission lines will depend on the shape of the BLR, distribution of gas clouds, and the presence of inflows or outflows. That being said, the emission line profiles are observed to not fall to zero as rapidly as a Gaussian. There has been luck in finding a good fit for this by using two coincident-peak Gaussians, one broader but with lower intensity. This suggests there is a component from the narrow line region or possible stratification of the BLR. Asymmetries are also common especially in CIV emission (e.g. Denney, 2012; Shin et al., 2017). The asymmetries are evidence of possible inflow, outflow, or other turbulence in the BLR and are also accounted for by fitting multiple Gaussians to any given emission line with offset central wavelength.

The broadened emission lines are a very useful tool in studying SMBH. Starting with the virial theorem which tells us the average potential energy of particles in the BLR is half the value of the kinetic energy, $\langle T \rangle = \frac{1}{2} \langle V \rangle$, it is straight forward to derive the relationship between the gas in the BLR and the mass of the black hole, M_{BH}

$$\frac{1}{2} m_{gas} v^2 = \frac{1}{2} G \left(\frac{M_{BH} m_{gas}}{R_{BLR}} \right)$$

where G is the gravitational constant, m_{gas} is the mass of the gas in the BLR, v is the

velocity of the gas, and R_{BLR} is the size of the BLR. Then we get that

$$M_{BH} = \frac{v^2 R_{BLR}}{G} \quad (1.1)$$

The velocity of the gas, v , can be measured from the width of the emission lines, the FWHM, while the size of the BLR can be found using a technique called reverberation mapping (Peterson, 1993; Denney et al., 2010; Edelson et al., 2015). AGN are known to be variable in energy output over time. When there is a change in the emission from the accretion disk, it can be observed in the continuum of optical-UV spectra. The radiation change will reach the BLR in time $t = r/c$ which can be detected as a change in flux of the emission lines. So if we can observe AGN at the time of the continuum variability and also after the light-travel time to reach the BLR, we can find the size, R_{BLR} . The reverberation mapping technique has been used to find M_{BH} for several AGN but the process is time consuming. The timescales for variability in the continuum of optical-UV spectra can range from days to weeks to months. Fortunately, this technique also led to the discovery of an empirical relationship between R_{BLR} and the luminosity (Wandel et al., 1999; Kaspi et al., 2000). This relationship gives us a way to measure M_{BH} using single-epoch spectra of AGN. Using Equation 1.1 and the R_{BLR} -luminosity relationship, scaling relations have been established for several broad lines. We use the following in this work – for $H\beta$ (Vestergaard & Peterson, 2006, eqn. 6)

$$\log(M_{BH}/M_{\odot}) = \log \left\{ \left[\frac{\text{FWHM}(H\beta)}{1000\text{km/s}} \right]^2 \left[\frac{L(H\beta)}{10^{44}\text{ergs/s}} \right]^{0.50} \right\} + 6.67 \quad (1.2)$$

Where $\text{FWHM}(H\beta)$ is the width of the $H\beta$ line and $L(H\beta)$ is the luminosity of the

emission line above the continuum. Similarly for $H\alpha$ (Greene & Ho, 2005a, eqn. 6):

$$\log(M_{BH}/M_{\odot}) = \log \left\{ \left[\frac{\text{FWHM}(H\alpha)}{1000\text{km/s}} \right]^{2.06} \left[\frac{L(H\alpha)}{10^{42}\text{ergs/s}} \right]^{0.55} \right\} + 6.30 \quad (1.3)$$

and $\text{MgII}\lambda 2800$ (McLure & Jarvis, 2002, eqn. 7):

$$\log(M_{BH}/M_{\odot}) = \log \left\{ \left[\frac{\text{FWHM}(\text{MgII})}{1000\text{km/s}} \right]^2 \left[\frac{\lambda L_{3000}}{10^{44}\text{ergs/s}} \right]^{0.47} \right\} + 0.53 \quad (1.4)$$

Note that for the scaling relation with MgII , M_{BH} was calibrated using the luminosity at 3000\AA .

1.1.3 Narrow Line Region

The narrow line region (NLR) extends out to hundreds of parsecs, close to the bulge of the host galaxy, and contains clouds of gas that are much less dense than those in the BLR.

Though the gas in the NLR is dominated by gravitational pull of the SMBH there are several ways in which the spectra differ from BLR spectra. First, as the name suggests, emission lines from the NLR are narrower – generally less than 500 km/s – suggesting lower orbital velocity. The lines are almost always asymmetric with a “blue wing” that is evidence of outflow from this region. Finally, it is almost exclusively forbidden lines that are observed in the NLR. Ionizing radiation from the accretion disk excites gas in the NLR, just as in the BLR, but because of low densities, collisional de-excitation is not probable.

The forbidden lines, e.g. $[\text{OIII}]\lambda\lambda 5007, 4959$ and $[\text{NII}]\lambda\lambda 6550, 6585$, are the result of excited electrons’ transitions from meta-stable energy states.

The narrow emission lines can be used to estimate M_{BH} just as with the BLR lines though not directly. A correlation between the velocity dispersion of stars in a galaxy

bulge, σ_* , and the M_{BH} has been used to probe SMBHs in galaxies (see Kormendy & Ho, 2013, for a recent review of the connection between bulges and black holes). However, because their luminosity can easily outshine the stars in the bulge, the presence of an AGN interferes with the measurement of σ_* . Greene & Ho (2005b) and Salviander & Shields (2013) demonstrate a relationship between the width of emission lines from the NLR and σ_* . We would expect such a connection given that the NLR and the bulge share the same gravitational potential.

In this work, we use the width of the [OIII] $\lambda 5007$ to estimate M_{BH} . The narrow emission lines are fit with two Gaussians - one for the core component (broadening due to orbital motion) and one that is blue-ward of the peak wavelength (to account for the outflow). The width of the core component is used as a proxy for $\sigma_* = \text{FWHM}([\text{OIII}])/2.35$ (Salviander & Shields, 2013) in the $M_{BH}-\sigma_*$ relation (Tremaine et al., 2002)

$$M_{BH} = (10^{8.13} M_{\odot}) \left(\frac{\sigma_*}{200 \text{ km/s}} \right)^{4.02} \quad (1.5)$$

1.1.4 Spectral Energy Distribution

Examining the overall output of radiation by AGN – the spectral energy distribution (SED) – can help in the detection of AGN, in understanding or constraining the physical processes, and to construct luminosity functions (number density of AGN at luminosity intervals) through cosmic time. Figure 1.3 shows the SED for two AGN in $\log(\nu L_{\nu})$ as a function of $\log(\nu)$ which are both roughly flat. The SED has traditionally been fit with a power law - flux, $F_{\nu} \propto \nu^{-\alpha}$ which implies a spectral index, $\alpha = 1$, for the flat SED in Figure 1.3. Of course AGN SED are not exactly flat and there are several physical

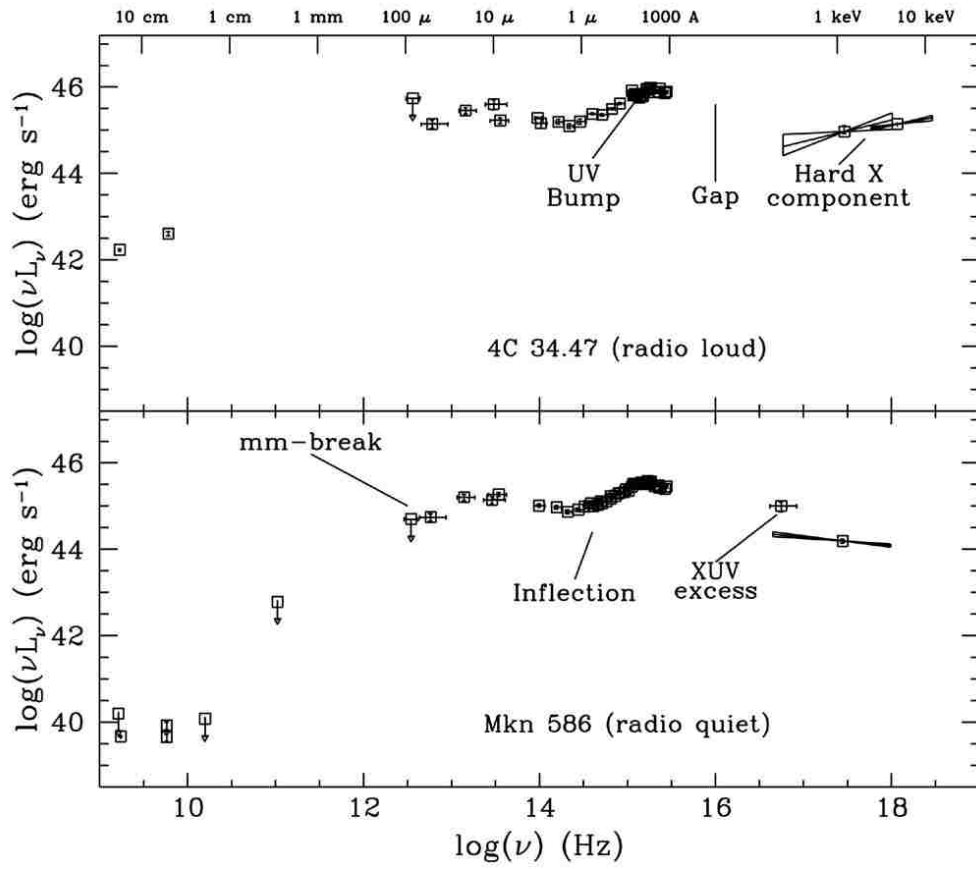


Figure 1.3: **Spectral Energy Distributions** — the SED of two well studied AGN - 4C 34.47 (top) and Mrk 586 (bottom) from Elvis et al. (1994).

processes that contribute to the emission.

There are two issues that make studying the total energy output of any particular AGN difficult, much less a large population of the objects. First, these objects occur at a large range of cosmological redshifts which means that any survey of a particular wave band could contain AGN at different emitted bands. Second, AGN emit significant amounts of radiation across a large range of wavelengths which requires multiple instruments for observation - radio, optical, X-ray, and space telescopes. Even for AGN that are observed with all these instruments, some parts of the spectrum will be hidden from observers confined to our Galaxy. Neutral hydrogen in the disk of the Milky Way absorbs photons from extragalactic sources between $\sim 100\text{\AA}$ and 1000\AA . This gap is obvious in Figure 1.3. Despite these difficulties, AGN SED have been studied for many objects giving astronomers a better idea of how the energy is produced. Though the exact mechanisms have not been pinned down to account for all of the radiation, it is helpful to examine some scenarios of accretion onto a SMBH. Given that we know there is ionized gas in the accretion disk, we expect synchrotron radiation to play a role. Figure 1.4 shows the spectrum of a single electron emitting due to synchrotron acceleration at top and the combined emission from particles in the accretion disk. The distribution of synchrotron spectra is expected to manifest as a power law, $F_\nu \propto \nu^{-\alpha}$, across several decades of the SED.

In order to explore the thermal emission from the disk, we start with the change in gravitational potential energy half of which is radiated away according to the virial theorem. So the luminosity of the disk is

$$L_{disk} = \frac{GM\dot{M}}{2r}$$

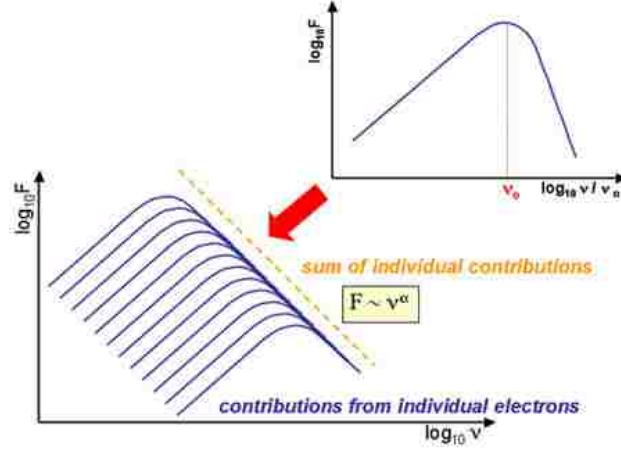


Figure 1.4: **Power Law Spectrum from Synchrotron Emission** — emission from a single electron (upper) and the sum from a distribution of synchrotron emitting electrons (lower).

We can first examine black-body radiation, B_ν , from the disk

$$B_\nu = \frac{2h\nu^3}{c^2} \frac{1}{e^{h\nu/kT(r)} - 1}$$

Then the luminosity from the disk will be

$$L_{disk} = \frac{GM\dot{M}}{2r} = 2\pi r^2 \sigma T^4$$

where the right side is the power emitted from a black body, the Stefan-Boltzman law. σ is the Stefan-Boltzman constant and the $2\pi r^2$ is the area of two sides of a disk. Solving for temperature

$$T = \left(\frac{GM\dot{M}}{4\pi\sigma r^3} \right)^{1/4}$$

We add a correction term for the energy dissipated through viscous torques (Peterson, 1997)

$$T(r) = \left[\frac{3GM\dot{M}}{8\pi\sigma r^3} \left\{ 1 - \left(\frac{R_{in}}{r} \right)^{1/2} \right\} \right]^{1/4}$$

and in terms of the Schwarzschild radius, R_S , the Eddington accretion rate, \dot{M}_E , and a typical black hole mass

$$T(r) \approx 6.3 \times 10^5 (\dot{M}/\dot{M}_E)^{1/4} (10^8 M_\odot)^{1/4} \left(\frac{r}{R_S} \right)^{-3/4} K$$

The maximum temperature will occur at the inner-most radius and peak of emission for this black-body radiation, $dB_\nu/d\nu = 0$,

$$\nu_{max} = \frac{2.8kT}{h} \approx 3.6 \times 10^{16} \text{Hz}$$

corresponding to wavelength $\lambda = 100\text{\AA}$, which implies that thermal emission is prominent in the UV-optical spectra of AGN. Of course the thermal emission from the accretion disk is superposition of several black-body curves showing different temperatures at different r_{disk} .

One of the main motivators to characterizing the shape of the SED is to ‘correct’ the brightness or magnitude observed in a particular wave band to a magnitude in the emitted band for an object. This is called K-correction and takes a magnitude in some observed band and corrects the measurement for the shifting of the wave band due to cosmological redshift as well as the change in flux due to the shrinking of the band (Hogg et al., 2002).

Figure 1.5 shows the response curve of the Sloan Digital Sky Survey r -filter and the effective responses for objects at a redshifts of 1, 2, and 3 — note that not only is the central wavelength shifted but the width is smaller. If the SED is consistent between objects, a measurement in one band is all that is necessary for a full description of the entire SED. Integrating over the SED will give the bolometric luminosity for individual AGN. K-corrections (Elvis et al., 1994; Wisotzki, 2000; Richards et al., 2006) and bolometric corrections (Runnoe et al., 2012; Lusso et al., 2012) are both computed by

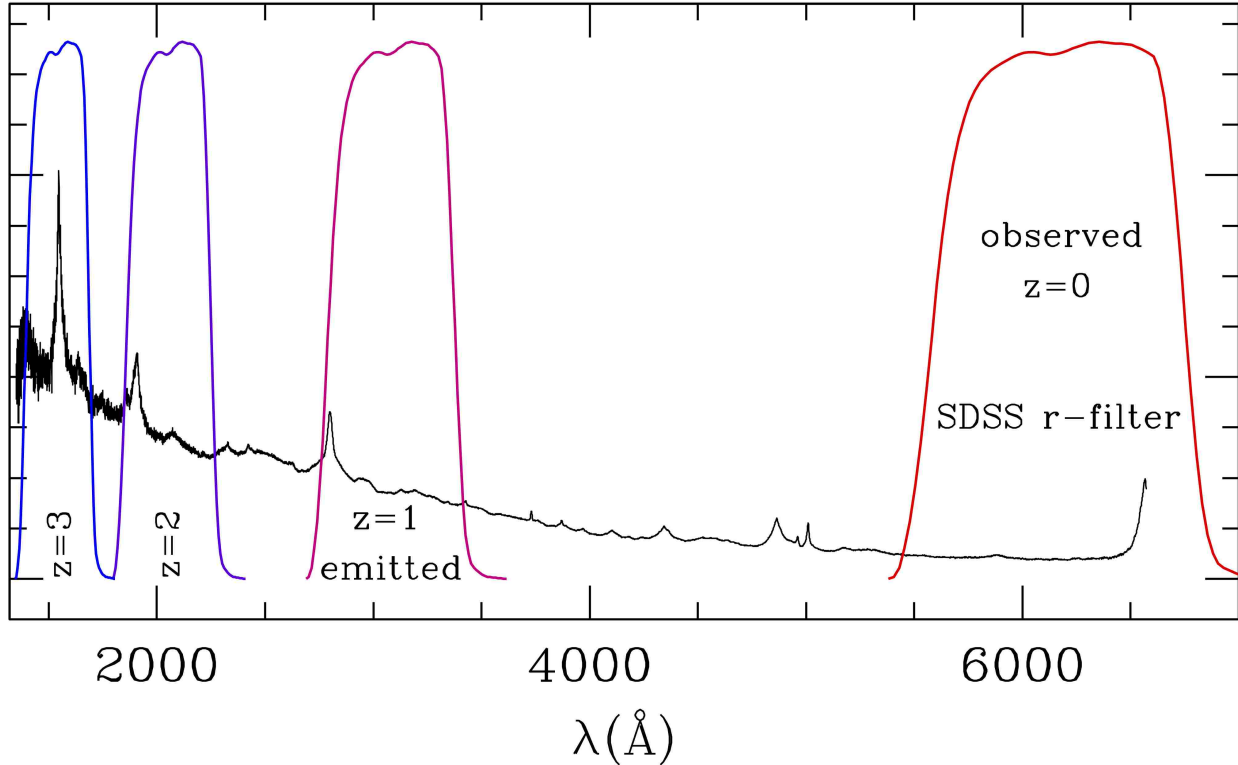


Figure 1.5: **Correcting for Redshift** — response curve of the SDSS *r*-filter (right) and the effective filter after correcting for observing objects at $z = 1, 2,$ and 3 overlaid on a composite AGN spectrum.

constructing average or composite SED from a sample of AGN that have measurements across the wave bands of interest. Under the assumption that all AGN SEDs are similar, the K-correction or bolometric correction can be applied to objects that have a limited number of measurements. The assumption that the SEDs of all AGN can be described by a single function, though known to be false, has been necessary until recently when large surveys have given data across the spectrum for large numbers of AGN.

1.2 AGN and Host Galaxies

The energy output of AGN, as previously noted, is large and in some cases can exceed the luminosity of the entire galaxy. It is easy to imagine that some of this energy will interact

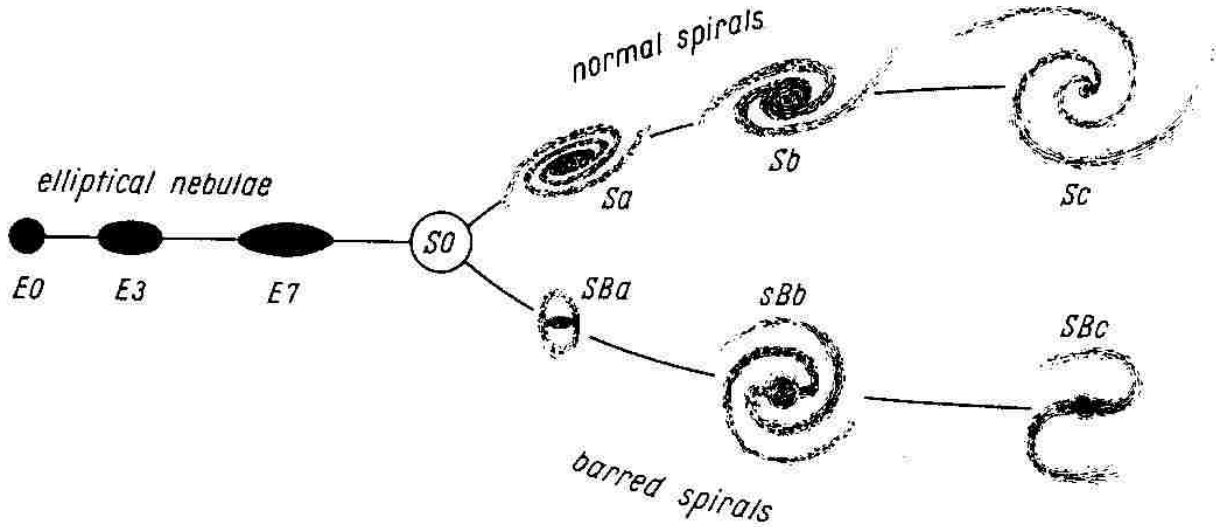


Figure 1.6: **Hubble's Tuning Fork** — classification of galaxies by morphology (Figure 1 from Hubble, 1936).

and possibly influence the host galaxy. In fact there have been several correlations found between the mass of SMBHs and larger structures of galaxies that suggest just such an interaction. A particularly tight correlation between the velocity dispersion of stars in a galaxy bulge, σ_* , and the black hole mass, M_{BH} , is well examined (e.g. Ferrarese & Merritt, 2000; Gebhardt et al., 2000; Gültekin et al., 2009; Woo et al., 2010) as well as correlations between M_{BH} and bulge mass (e.g. Magorrian et al., 1998; Häring & Rix, 2004) and bulge luminosity (e.g. Kormendy & Richstone, 1995; McLure & Dunlop, 2001; Wandel, 2002; Bentz et al., 2009). In fact the relationship between large galaxy components and the central region have been noted since Hubble's Tuning Fork diagram, Figure 1.6, related tightly wound spiral arms to brighter bulges. These relationships suggest that AGN are the drivers of the co-evolution. Silk & Rees (1998) describe a scenario in which a galaxy bulge will feed gas to an AGN until the black hole reaches some critical mass at which point an 'explosion' event happens. The winds from the AGN will act to expel gas out of the region and heat gas within the galaxy. Both would work to suppress star formation.

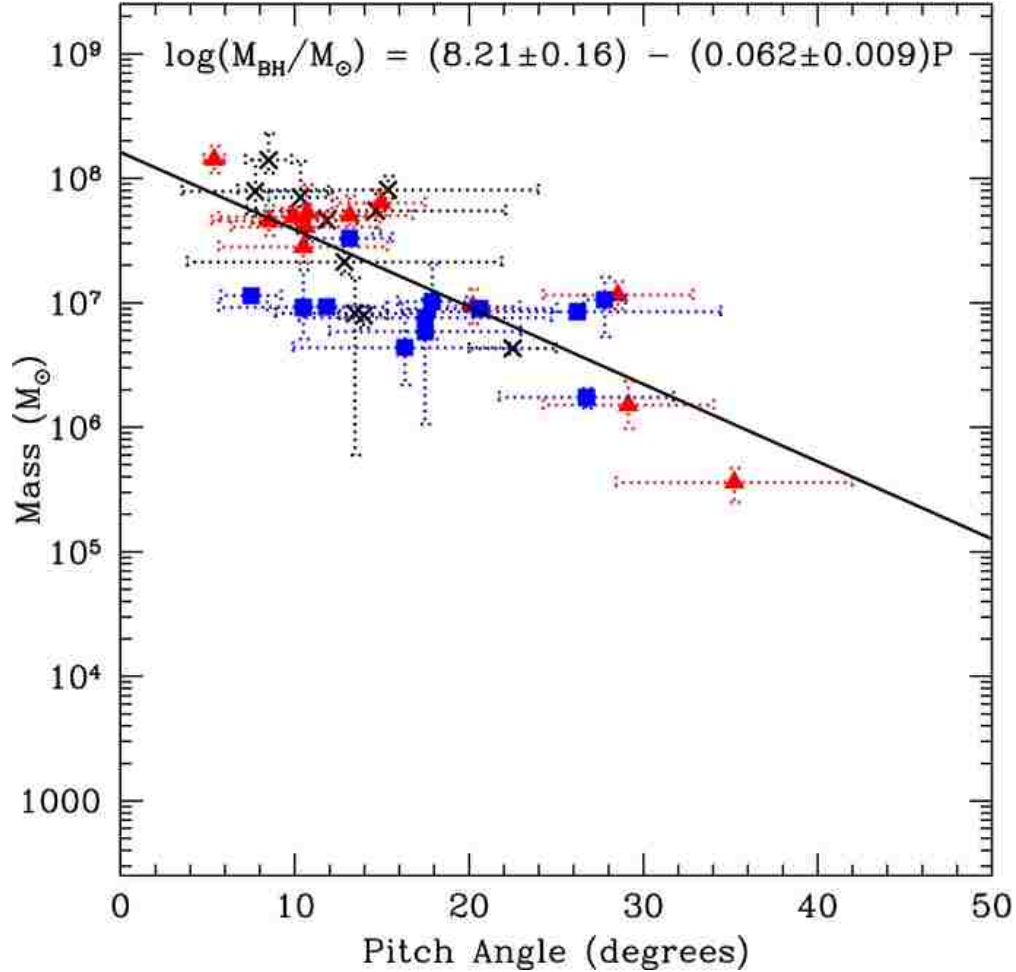


Figure 1.7: **Local Mass-Pitch Angle Relation** — established using a sample of 34 spiral galaxies with directly measured black hole mass (Berrier et al., 2013).

1.2.1 Spiral Galaxies and Density Wave Theory

The correlations between black holes and host galaxies that are suggestive of AGN feedback are robust for ellipticals and well studied in local epochs. The above mentioned correlations are not as strong for spiral galaxies but in this work we will explore a relationship exclusive to spirals galaxies – specifically the relationship between M_{BH} and the tightness of spiral arms in disk galaxies. Berrier et al. (2013) showed that tighter spiral arms, quantified as pitch angle (ϕ), correlate with higher mass black holes. See Figure 1.7. This relationship is a straightforward result of the density wave theory of spiral arm formation (Lin & Shu,



Figure 1.8: **Spiral Density Waves** — left: NGC 3344 (Photo by Adam Block/Mount Lemmon SkyCenter/University of Arizona) compared to, right: cartoon of density wavefronts moving through a rotating disk.

1966). The density wave theory describes waves which are regions of higher density that move through the disk of a galaxy sparking star formation. In Figure 1.8, the right panel shows wavefronts as they move radially out from the center of the galaxy through a rotating disk. The coincidence of these wavefronts are what cause the spiral pattern.

Density wave theory predicts that the pitch angle of spiral arms will be governed by

$$\tan(\phi) \propto \frac{\sigma_0 + F\sigma_{star}}{M_0} \quad (1.6)$$

where σ_0 represents the density of gas in the disk, σ_{star} the mass density of stars in the disk, and M_0 the mass of the galaxy bulge. The reduction factor, F , should be very small since the density wave will affect the gas primarily. The theory has a nice analog in standing waves on a string. The speed of a wave on a string is proportional to tension and inversely proportional to the density of the string itself. In the same way, the pitch angle depends on the tension in the disk, gravitational force from the center of the galaxy in this case, and the density of the medium it travels through, the gas density.

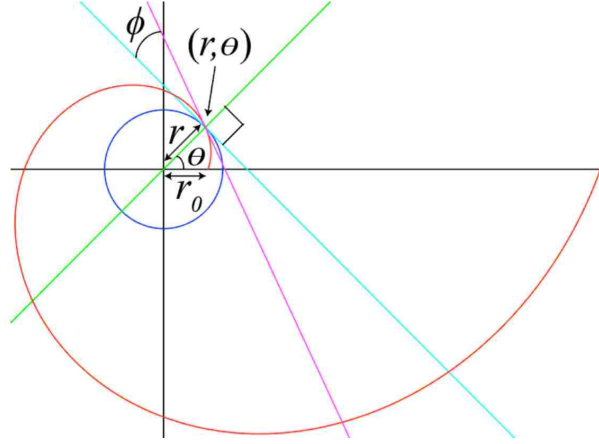


Figure 1.9: **Logarithmic Spiral in Polar Coordinates**

Density wave theory predicts logarithmic spirals quantified in polar coordinates as

$$r = r_0 e^{b\theta} \tag{1.7}$$

where $b = \tan(\phi)$ and ϕ is the pitch angle. Figure 1.9 shows ϕ as the angle between a line tangent to the spiral arm and a line tangent to a circle at that same point. Therefore ϕ describes how circular a spiral arm is and thus ranges from 0° , a perfect circle, to 90° , a straight line.

1.2.2 Pitch Angle Measurement

In this work we use a two-dimensional Fourier transform algorithm, 2DFFT to measure pitch angle (Saraiva Schroeder et al., 1994). The 2DFFT algorithm decomposes the signal from an image of a spiral galaxy into a superposition of logarithmic spirals of different pitch angle and mode. The mode of the galaxy refers to the symmetry and in most cases will indicate the number of arms. A 2DFFT user must first deproject a galaxy image to face-on then define the inner and outer radii of the disk. Davis et al. (2012) find that the measurement is very dependent on the choice of inner radius – a user could inadvertently

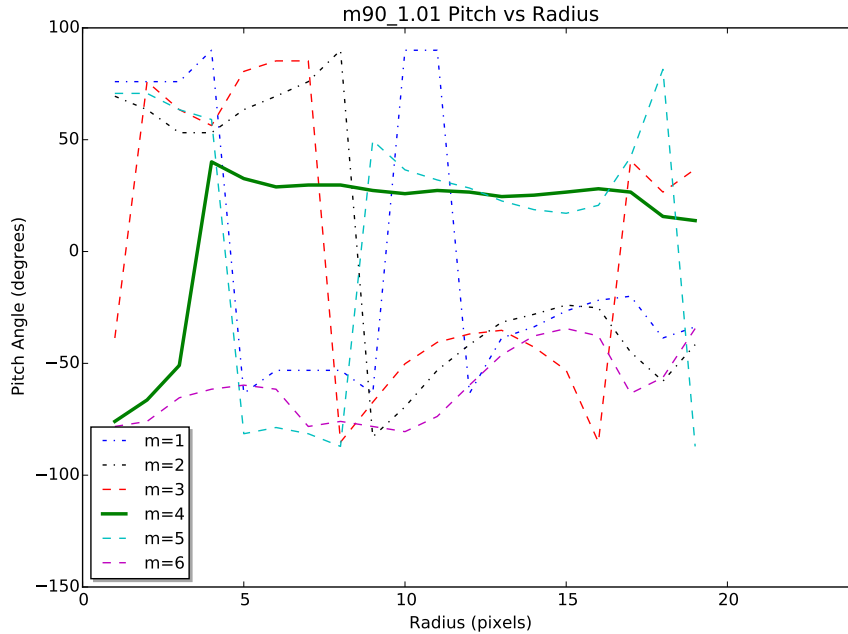


Figure 1.10: **2D FFT output** — pitch angle as a function of inner radius for modes $m = 1 - 6$.

include signal from the bright center of the galaxy or a bar feature. They find that if 2DFFT iteratively measures the galaxy with larger and larger inner radii, a user can pick out the appropriate radius from the 2DFFT output. Figure 1.10 is an example of the output from 2DFFT where the pitch angle is plotted as a function of the inner radius that was defined for each measurement. The thick green line shows the most likely pitch angle for this galaxy which is determined by first verifying that the galaxy is a $m = 4$ or four-arm galaxy and second recognizing that the algorithm was stable out past a radius of ~ 5 pixels. The pitch angle is reported as the average over this stable region.

1.3 Summary

In this dissertation, I will focus on previous assumptions made about the the shape of AGN SEDs and explore how AGN interact with spiral galaxies. In Chapter 2, I analyze the optical-UV SED of high-redshift AGN. The SED are constructed from magnitude measurements in *griz* and JHK bands of AGN at $z \sim 2, 3,$ and 4. I fit the SED to a power law, $f \propto \nu^{-\alpha}$, in order to determine the spectral index, α . I discuss the measurements as they relate to K-corrections and bolometric corrections. In Chapter 3, I present a sample of spiral galaxies that host AGN. These galaxies range in redshift from $z = 0.04$ to $z = 1.41$. I use this sample to explore the relationship between black hole mass and pitch angle in past epochs and investigate spiral galaxy formation and evolution.

Bibliography

- Ahn, C. P., Seth, A. C., den Brok, M., et al. 2017, *ApJ*, 839, 72
- Bentz, M. C., Peterson, B. M., Pogge, R. W., & Vestergaard, M. 2009, *ApJL*, 694, L166
- Berrier, J. C., Davis, B. L., Kennefick, D., et al. 2013, *ApJ*, 769, 17
- Davis, B. L., Berrier, J. C., Shields, D. W., et al. 2012, *ApJS*, 199, 20
- Denney, K. D. 2012, *ApJ*, 759, 44
- Denney, K. D., Peterson, B. M., Pogge, R. W., et al. 2010, *ApJ*, 721, 715
- Edelson, R., Gelbord, J. M., Horne, K., et al. 2015, *ApJ*, 806, 129
- Elvis, M., Wilkes, B. J., McDowell, J. C., et al. 1994, *ApJS*, 95, 1
- Fath, E. A. 1909, *Lick Observatory Bulletin*, 5, 71
- Ferrarese, L., & Merritt, D. 2000, *ApJ*, 539, L9
- Gebhardt, K., Bender, R., Bower, G., et al. 2000, *ApJL*, 539, L13
- Greene, J. E., & Ho, L. C. 2005a, *ApJ*, 630, 122
- . 2005b, *ApJ*, 627, 721
- Gültekin, K., Richstone, D. O., Gebhardt, K., et al. 2009, *ApJ*, 698, 198
- Håring, N., & Rix, H.-W. 2004, *ApJL*, 604, L89
- Hogg, D. W., Baldry, I. K., Blanton, M. R., & Eisenstein, D. J. 2002, *ArXiv Astrophysics e-prints*, astro-ph/0210394
- Hoyle, F. 1948, *MNRAS*, 108, 372
- Hubble, E. P. 1936, *Realm of the Nebulae* (New Haven: Yale University Press)
- Kaspi, S., Smith, P. S., Netzer, H., et al. 2000, *ApJ*, 533, 631
- Kormendy, J., & Ho, L. C. 2013, *ARA&A*, 51, 511
- Kormendy, J., & Richstone, D. 1995, *ARA&A*, 33, 581
- Krolik, J. H. 1998, *Active Galactic Nuclei: From the Central Black Hole to the Galactic Environment* (Princeton: Princeton University Press)
- Lin, C. C., & Shu, F. H. 1966, *PNAS*, 55, 229

Lusso, E., Comastri, A., Simmons, B. D., et al. 2012, MNRAS, 425, 623

Magorrian, J., Tremaine, S., Richstone, D., et al. 1998, AJ, 115, 2285

McLure, R. J., & Dunlop, J. S. 2001, MNRAS, 327, 199

McLure, R. J., & Jarvis, M. J. 2002, MNRAS, 337, 109

Mortlock, D. J., Warren, S. J., Venemans, B. P., et al. 2011, Nature, 474, 616

Osterbrock, D. E. 1989, Astrophysics of gaseous nebulae and active galactic nuclei (University Science Books)

Peterson, B. M. 1993, PASP, 105, 247

—. 1997, An Introduction to Active Galactic Nuclei (Cambridge University Press)

Richards, G. T., Strauss, M. A., Fan, X., et al. 2006, AJ, 131, 2766

Runnoe, J. C., Brotherton, M. S., & Shang, Z. 2012, MNRAS, 422, 478

Salviander, S., & Shields, G. A. 2013, ApJ, 764, 7

Saraiva Schroeder, M. F., Pastoriza, M. G., Kepler, S. O., & Puerari, I. 1994, A&AS, 108

Schmidt, M. 1963, Nature, 197, 1040

Seyfert, C. K. 1943, ApJ, 97, 28

Shin, J., nagao, T., & Woo, J.-H. 2017, ApJ, 835, 24

Silk, J., & Rees, M. J. 1998, A&A, 331, L1

Tremaine, S., Gebhardt, K., Bender, R., et al. 2002, ApJ, 574, 740

Vanden Berk, D. E., Richards, G. T., Bauer, A., et al. 2001, AJ, 122, 549

Vestergaard, M., & Peterson, B. M. 2006, ApJ, 641, 689

Wandel, A. 2002, ApJ, 565, 762

Wandel, A., Peterson, B. M., & Malkan, M. A. 1999, ApJ, 526, 579

Weedman, D. W. 1986, Quasar astronomy (Cambridge University Press)

Wisotzki, L. 2000, A&A, 353, 861

Woo, J.-H., Treu, T., Barth, A. J., et al. 2010, ApJ, 716, 269

Chapter 2

The Optical-UV Spectral Index of Quasars

2.1 Abstract

A common practice when formulating quasar luminosity functions (QLF) has been to adopt an average spectral index, α , for the sample even though it is well known that quasars exhibit a broad range of spectral energy distributions (SED). We have investigated the possible evolution of α as a function of redshift, as any evolution in this parameter would introduce or mask evolution in the QLF. We imaged 96 Sloan Digital Sky Survey (SDSS) quasars in the optical and near-infrared bands, near in time to mitigate the effects of variability, in three redshift bins centered at $z \approx 1.9$, 2.7, and 4.0, corresponding to look-back times of 10-12 billion years. We present restframe UV-optical SEDs and spectral indices and discuss possible evolution in our sample.

2.2 Introduction

Active Galactic Nuclei, AGN, emit significant amounts of radiation across the electromagnetic spectrum; i.e. from radio to X-ray. In order to understand AGN – the population as a whole and the physical processes that produce radiation in individual AGN – complete spectra from a large sample would be ideal. The difficulty lies in the fact that AGN are found at a range of redshifts. Even observing a population of AGN in a single band can mean the rest-frame band is very different depending on individual redshifts.

Two common ways to address this are through K-correction, the process of correcting an observed monochromatic luminosity to a rest-frame luminosity in another band, and

bolometric correction, the conversion of an observed monochromatic luminosity to a bolometric luminosity. Both of these corrections depend on knowledge about the spectral energy distribution, SED. There have been a number of studies of AGN with relatively complete spectra that are used to construct composite or average SED (e.g. Elvis et al., 1994; Shang et al., 2011). The composite or average SED are subsequently used to formulate the bolometric and K-corrections. Thus, for example, if one has a B-band measurement, the bolometric luminosity can be calculated under the assumption that the SED is similar to the composite SED. Or, for K-correction, the slope of the SED in the portion of interest. However, the composite and average SEDs should be used with caution. The sample size used to construct composite SEDs is limited because of the observing issues mentioned above and, even in small data sets, the variance in the SED of individual AGN is large.

The SEDs of quasars have been found to follow a power-law distribution in brightness, $f \propto \nu^\alpha$. In this paper, we construct SEDs in the emitted optical-UV region of 96 AGN from the SDSS quasar catalog in order to measure the slope or spectral index, α . This work is a follow-up to Kennefick & Bursick (2008) – KB08 from here on. The SED are constructed from quasi-simultaneous observations in the *griz* and JHK bands. The sample and observation program are presented in §2.3, the technique for constructing the SED and the results are in §2.4, and §2.5 contains analysis of the data including a comparison of spectral indices to other AGN properties.

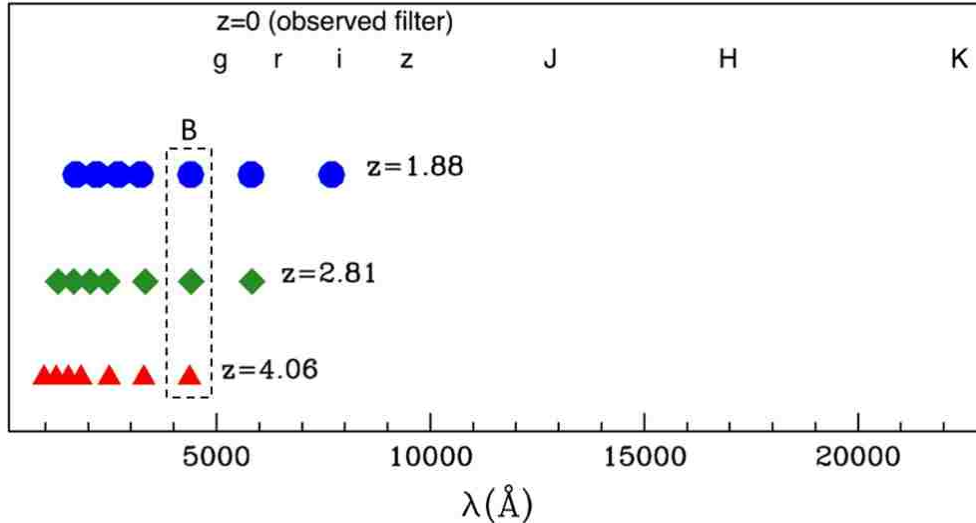


Figure 2.1: **Sampled wavebands** — central wavelength of observed filters compared to the rest-frame wavebands in each redshift bin. The emitted B -band is marked for each redshift.

2.3 Sample and Data

The sample was selected from the third edition of the Sloan Digital Sky Survey (SDSS) Quasar Catalog (Schneider et al., 2005). Objects were chosen by redshift so that the B -band, centered at 4400 \AA , samples the observed infrared J, H, and K bands, centered at $1.27 \mu\text{m}$, $1.67 \mu\text{m}$, and $2.21 \mu\text{m}$, respectively. The original purpose of this selection was to observe the flux from the emitted B -band of high redshift quasars without the need to use K-correction (KB08). We extend that work by observing quasars in the same redshift bins across the optical-UV spectrum in order to measure the spectral index, α_o , intrinsic to each object; i.e. we do not assume an average K-correction term. We construct the SED across the optical-UV band in order to measure the spectral index. The sample consists of 96 quasars – 31 at average redshift $\langle z \rangle = 1.88$, 31 at $\langle z \rangle = 2.80$, and 34 at $\langle z \rangle = 4.07$. Each quasar was observed in the optical $griz$ bands and the infrared JHK bands and therefore the rest-frame bands give us an optical-UV spectral energy distribution (SED) for each

quasar. In Figure 2.1 the central wavelength of the filters in the observed frame is compared to the wavelength of the emitted bands for each redshift bin shifted by $\lambda_{emit} = \lambda_{obs}/(1+z)$. Co-epochal measurements were taken across the wavelength range in order to reduce the effects of variability common in quasar luminosity.

2.3.1 Observation and Image Reduction

Observations were carried out at Kitt Peak National Observatory’s 2.1 meter telescope. Infrared images were taken with the Simultaneous Quad Infrared Imaging Device (SQIID) during 2005 November 4–10. A dithering program was used such that each object was imaged for 120 seconds in each of 5 offset positions. Also, 10 – 20 dark images were taken throughout each night. The IRAF package UPSQIID¹ was used for image reduction. We used the task `usqdark` to account for noise within the detector – pixel values of the dark images were averaged over a night to create dark frames. Flat frames, used to account for pixel to pixel variation in sensitivity, were created using `usqflat` and object images — first, the dark frame was subtracted from an image and then each pixel value was divided by the median pixel value in the image. The flat frames used were an average over a night of individual flats. The final type of processing image, the sky frame was created to account for noise in the sky since IR imaging is particularly sensitive to thermal emission in the atmosphere. Once again, object images were used with `movproc` to create sky frames by first flattening the raw frames and then averaging the six frames imaged closest in time to the frame being processed. Each object image was processed by subtracting off the dark frame, dividing by the flat frame, and subtracting off the flattened sky frame. Finally the

¹<https://www.noao.edu/kpno/sqid/upsqidpkg.html>

dithered frames were combined by applying spacial offsets. The task `xyget` identifies, with user input, common objects across dithered frames, applies the spacial offset, and then averages corresponding pixel values. For more details of the image reduction process in the IR see Appendix A.1.

Optical images were taken with the T2KB CCD during 2005 November 30–December 5. Each quasar was imaged in g, r & i for 60 or 90 seconds and in z for 120 or 180 seconds. Bias, dark, and dome flat images were taken each night. Image reduction was carried out using the IRAF package `CCDRED`. Zero-level images were created from the average of the bias and dark images over the entire run, flat images from the average of all dome flats, and sky images from the average of all the object images. The dark, bias, and sky images were subtracted and then the image was flattened using the flat image.

World coordinate system information was added to each image header using `IMWCS`.² Plate solutions are computed by starting with the approximate sky coordinate information in the header of an image and then matching point sources to a catalog – in this case from the Two Micron All Sky Survey (2MASS, Skrutskie et al., 2006)³ – with known coordinates.

2.3.2 Photometry

The uncalibrated instrument magnitudes were found via aperture photometry with an aperture size of twice seeing. We used `SExtractor` source-extraction software (Bertin &

²tdc-www.harvard.edu/software/wcstools/imwcs/imwcs.html

³This publication makes use of data products from the Two Micron All Sky Survey, which is a joint project of the University of Massachusetts and the Infrared Processing and Analysis Center/California Institute of Technology, funded by the National Aeronautics and Space Administration and the National Science Foundation.

Arnouts, 1996) to locate point sources and measure uncalibrated magnitudes for each. Point sources in the frame with the quasar were used to calibrate the instrument magnitude. By locating objects in each frame that have calibrated magnitudes in the literature, we are able to calculate the difference in the known magnitude and the instrument magnitude; i.e. find the zero-point offset, m_o .

$$m_{object} = m_{instrument} + m_o$$

where m_{object} is the calibrated, apparent magnitude of the object and $m_{instrument}$ is the magnitude recovered from SExtractor. We found point sources of known magnitude (also called calibration stars) in 2MASS for the JHK frames. And we used the SDSS Data Release 7 (Abazajian et al., 2009) to find calibration stars for the *griz* images. We matched the coordinates of the point sources found in each image to the 2MASS and SDSS catalogs using the US Virtual Astronomical Observatory’s Cross-Comparison Tool.⁴ The matched objects were examined to exclude faint objects, bright objects that saturated the detector, and close pairs. Once these cuts were made, each image had 10–20 calibration stars in the frame with the quasar. The instrument magnitude was subtracted from the magnitude reported in 2MASS or SDSS to give the zero-point offset, m_o , for each calibration star. An average offset was calculated for each frame and applied to the quasar’s instrument magnitude in order to get a calibrated apparent magnitude.

All magnitudes were converted to the AB magnitude system which is calibrated in units of absolute flux density, $m_{AB} = -5/2 \log(f_\nu) + 48.6$ with the zero-point calibrated for a flat source of $f_\nu = 3.631 \times 10^{-20}$ ergs/s/cm²/Hz (Oke, 1974). JHK band magnitudes were

⁴<http://www.usvao.org/science-tools-services/cross-comparison-tool/>

converted using the technique of KB08. The *griz* magnitudes were corrected using SDSS calibrations⁵ of $z_{AB} = z_{SDSS} + 0.02\text{mag}$ but no corrections are necessary for the other three bands. Finally, Galactic extinction correction was applied to each magnitude using the reddening maps of Schlegel et al. (1998).

2.4 Optical-UV Spectral Index

The SED for each quasar consists of magnitude measurements from the observed *griz* and JHK bands. In the rest frame of each quasar this means the optical-UV portion of the spectrum is being examined in the range $\sim 1000\text{\AA}$ to 10000\AA . The rest-frame wavebands sampled in each redshift bin are shown in Figure 2.1. In order to quantify the SED, we assume that $f_\nu \propto \nu^\alpha$, and calculate α .

The AB magnitudes are expressed as

$$m_{AB} = -2.5 \log(f_\nu) - 48.6 \quad (2.1)$$

And adopting $f_\nu = \nu^\alpha$,

$$m_{AB} = -2.5\alpha_o \log(\nu) - 48.6 \quad (2.2)$$

thus the slope of a linear fit to the SED is proportional to the spectral index. We used the linear regression routine FIT from Numerical Recipes to find the linear relation of m_{AB} as a function of $\log(\nu)$. The slope of the fit was used to calculate $\alpha_o = \text{slope}/-2.5$ for each quasar. The results are listed in Table 2.1. The error in α_o reflects the standard error from the regression fit. The average spectral index, $\langle \alpha_o \rangle$, of the entire sample is -0.673 and for

⁵<http://classic.sdss.org/dr7/algorithms/fluxcal.html>

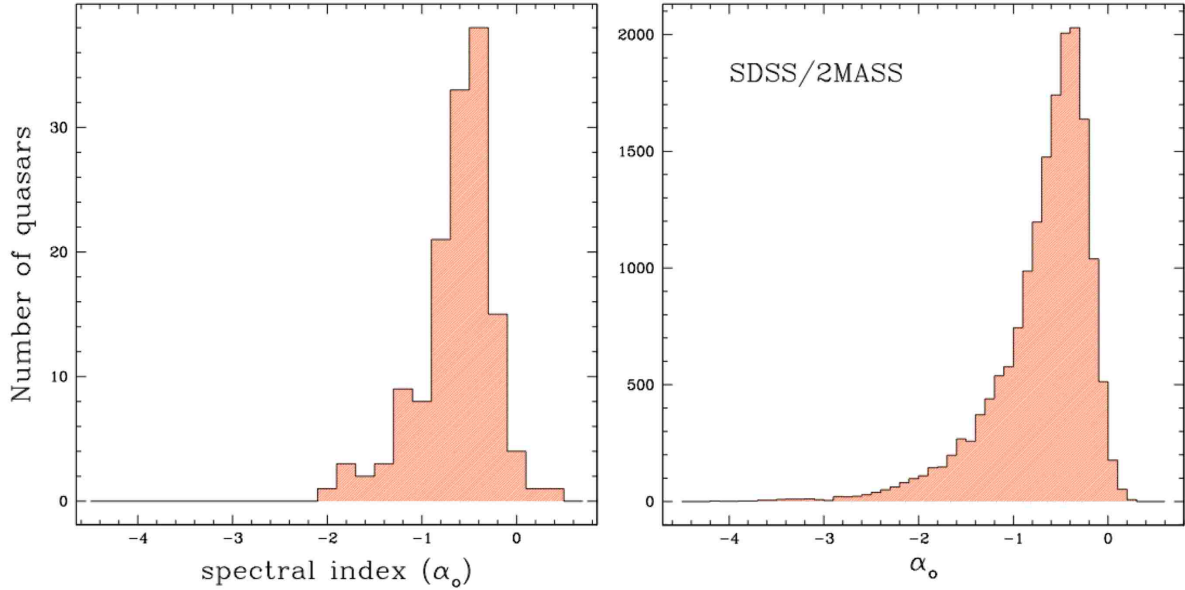


Figure 2.2: Distribution of spectral index for the co-epochal sample (left) and the SDSS–2MASS sample (right)

each redshift bin: $\langle \alpha_o \rangle = -0.574 \pm 0.362$ for $z = 1.88$, $\langle \alpha_o \rangle = -0.670 \pm 0.512$ for $z = 2.80$, and $\langle \alpha_o \rangle = -0.776 \pm 0.272$ for $z = 4.07$. As a comparison, spectral index was calculated using the above method for quasars that had measurements in the *griz* bands from the SDSS DR7 quasar catalog and in the JHK bands from 2MASS. It should be noted that these data differ from the co-epochal sample since the magnitude measurements were taken several years apart. There are 17,149 quasars in this SDSS–2MASS sample. Figure 2.2 shows the distribution of spectral index for both the co-epochal sample and the SDSS–2MASS sample.

Conversion of observed magnitudes to intrinsic (absolute) magnitudes for high redshift objects involves correcting for shifting out of the wavelength range of the detector as well as the effective squeezing of the band. These are both accounted for in the two-term

K-correction. For SED of the form $f_\nu \propto \nu^\alpha$,

$$K(z) = -2.5 \log(1+z) - \alpha 2.5 \log(1+z) \quad (2.3)$$

where $\alpha = -0.5$ is traditionally assumed based on composite quasar SED. The average spectral index in our sample is not consistent with this assumption - overall and in each redshift bin we find $\langle \alpha_o \rangle < -0.5$. The scatter in the measured spectral index of the co-epocal sample is represented in Figure 2.3 where the bold line represents the median, the box ends are the Q_1 and Q_3 quartile points, the bars are the most extreme points that are not outliers, and the points are the outliers. This scatter is also evident in Figure 2.2 and suggests that using a spectral index of $\alpha = -0.5$ when calculating K-correction could skew results.

We also find indications of a trend in α_o with redshift. The mean spectral index in each redshift; $\langle \alpha_o \rangle_{z=1.88} = -0.574$, $\langle \alpha_o \rangle_{2.80} = -0.670$, and $\langle \alpha_o \rangle_{4.07} = -0.776$ for $z = 4.07$; suggests α_o decreases as redshift increases. If we add the sample from KB08 which was measured in the same manner as the sample described here, the trend flattens. Figure 2.4 shows α_o as a function of redshift for the 96 quasars in this sample as well as 45 from KB08 where a linear fit results in $\alpha_o = -0.02z - 0.57$. We explore evolution in redshift of α_o further by looking at the two samples in Figure 2.2. The SDSS-2MASS sample peaks in redshift at $z \simeq 0.4$ but our sample extends far beyond that to $z \simeq 4.0$. A plot of α_o for both samples is shown in Figure 2.5 – the co-epochal sample is represented as filled circles and the SDSS-2MASS sample as black points; the redshift distribution of the SDSS-2MASS sample in the lower panel.

If there is some evolution in α_o with redshift, then we would expect the two samples,

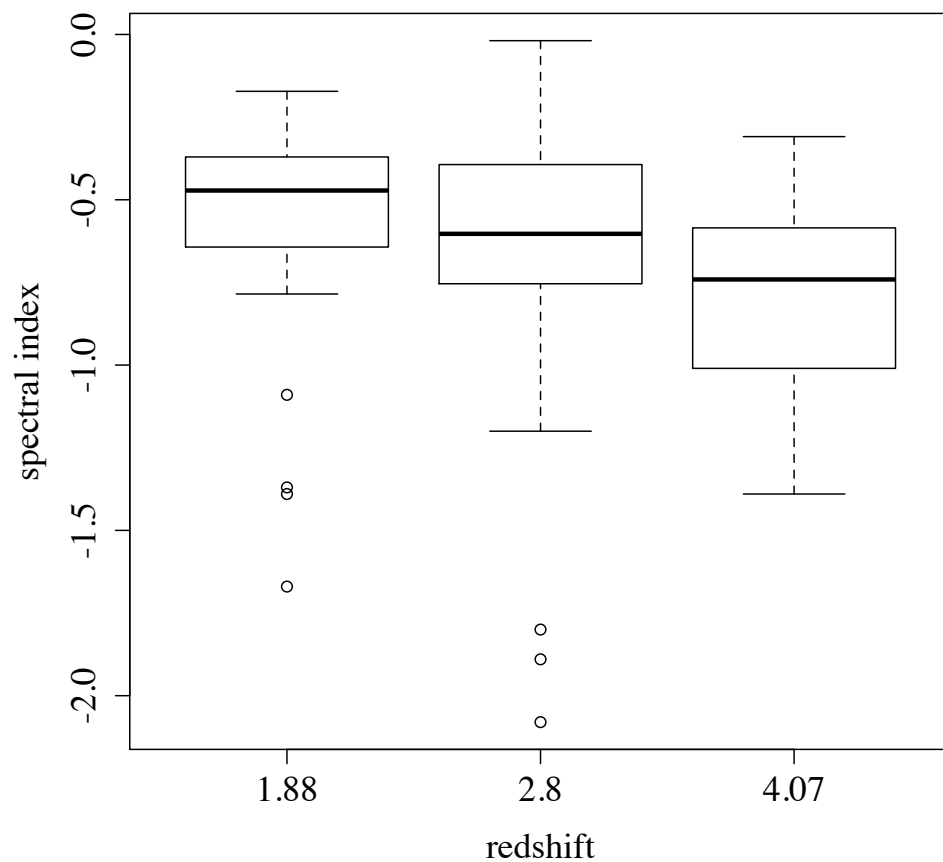


Figure 2.3: Distribution of α_o in each redshift bin in the co-epocal sample. The bold line represents the median, the box ends are the Q_1 and Q_3 quartile points, the bars are the most extreme points that are not outliers, and the points are the outliers; an outlier is defined as any point whose value is more than $3/2$ the interquartile range, $IQR = Q_3 - Q_1$

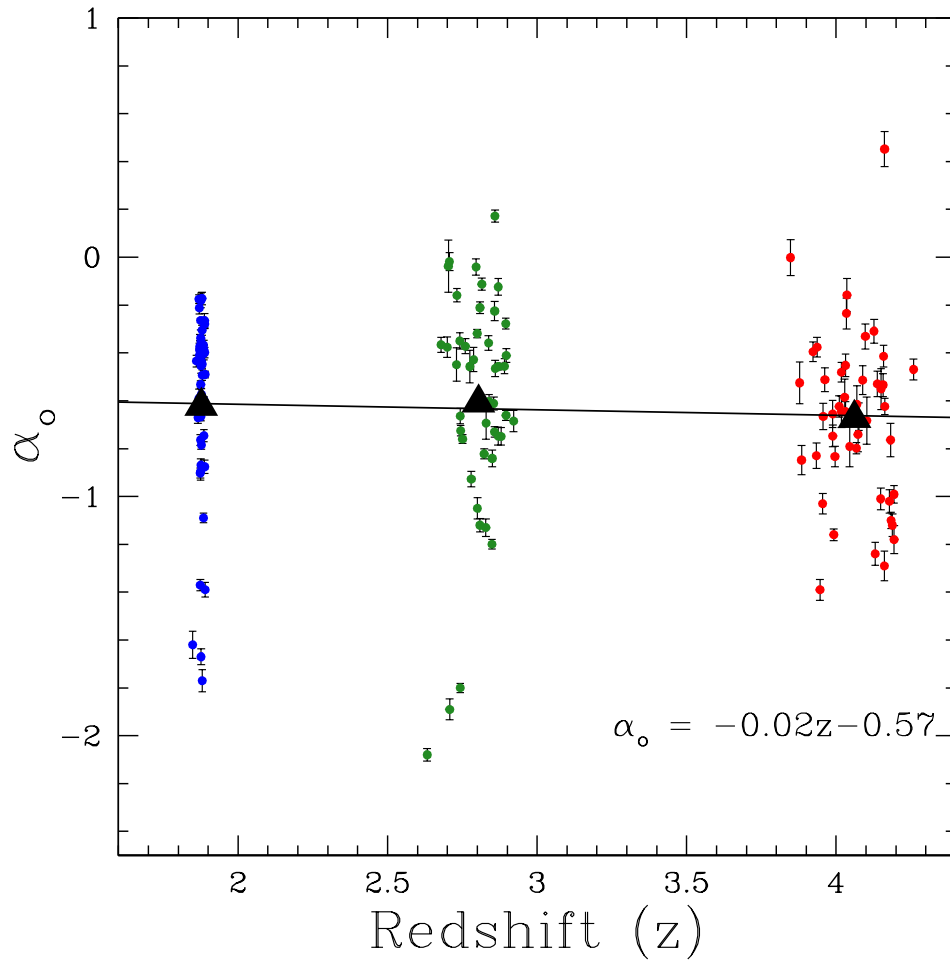


Figure 2.4: **Spectral Index as a Function of Redshift** — α_o measurements of the 95 quasars in this sample as well as 45 quasars from KB08; the average from each redshift bin are shown as a black triangles and are $\alpha_o(z = 1.88) = -0.62$, $\alpha_o(2.80) = -0.61$, and $\alpha_o(4.06) = -0.67$; the line is a least-squares fit with the equation shown at bottom-right.

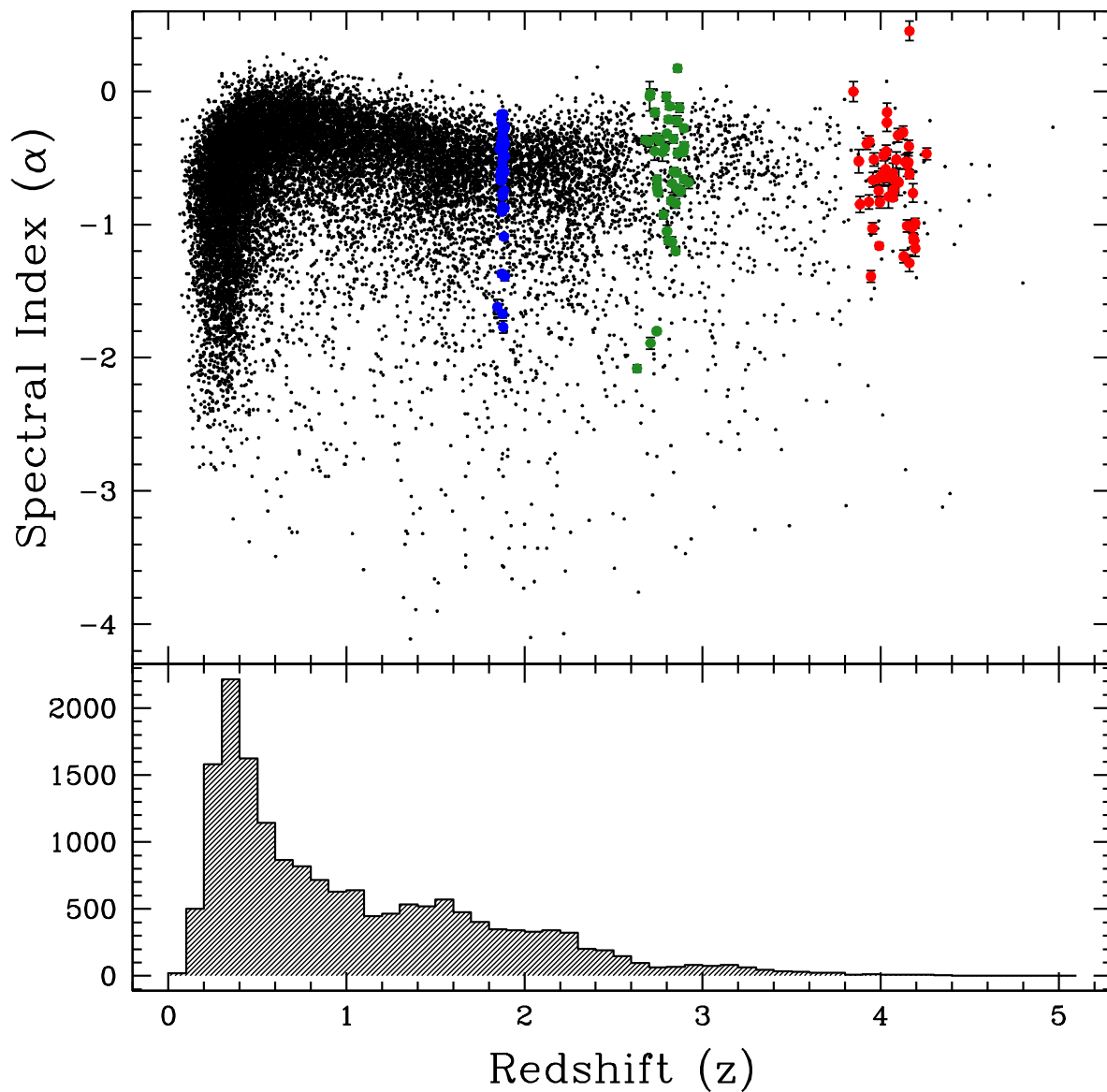


Figure 2.5: **Spectral Index as a Function of Redshift (all)** — colored circles are quasars from the co-epochal sample and include KB08 data, black points are the SDSS-2MASS sample, bottom plot shows the distribution in redshift of quasars in the SDSS-2MASS sample.

co-epochal and SDSS-2MASS, to have a different distribution. The mean of the distribution for the SDSS-2MASS sample is $\langle\alpha_o\rangle = -0.69$ and for the co-epochal plus KB08 sample, $\langle\alpha_o\rangle = -0.64$. We used a version of the Two-Sample Kolmogorov-Smirnov test to explore whether the samples come from the same distribution. The task `ks.boot` from the R package `Matching` is a bootstrap version of the traditional K-S test for samples that have repeated values. We used 1000 bootstraps which returned a p-value of 0.46 indicating that we can comfortably reject the hypothesis that α_o -distributions from the two samples are the same. This could indicate α_o changes on average with redshift or that there is some other physical difference between the two samples. One difference already noted is that quasars in the SDSS-2MASS sample were not imaged at the same time and so variability could play a role.

2.5 Corrected M_i Absolute Magnitudes

We use α_o from the co-epochal SED fit to find absolute i -band magnitudes from the observed magnitudes for each quasar

$$M_i = m_i - 5 \log(D_L/10\text{pc}) - K(z) \quad (2.4)$$

where $K(z)$ is the K-correction (Equation 2.3) and D_L is the luminosity distance which is the relationship between flux and luminosity, $L = (4\pi D_L^2 f)$. D_L is also a function of comoving distance and can be expressed as

$$D_L = \frac{c(1+z)}{H_0} \int_0^z \sqrt{(1+z')^2(1+\Omega_M z') - z'(2+z')\Omega_\Lambda} dz' \quad (2.5)$$

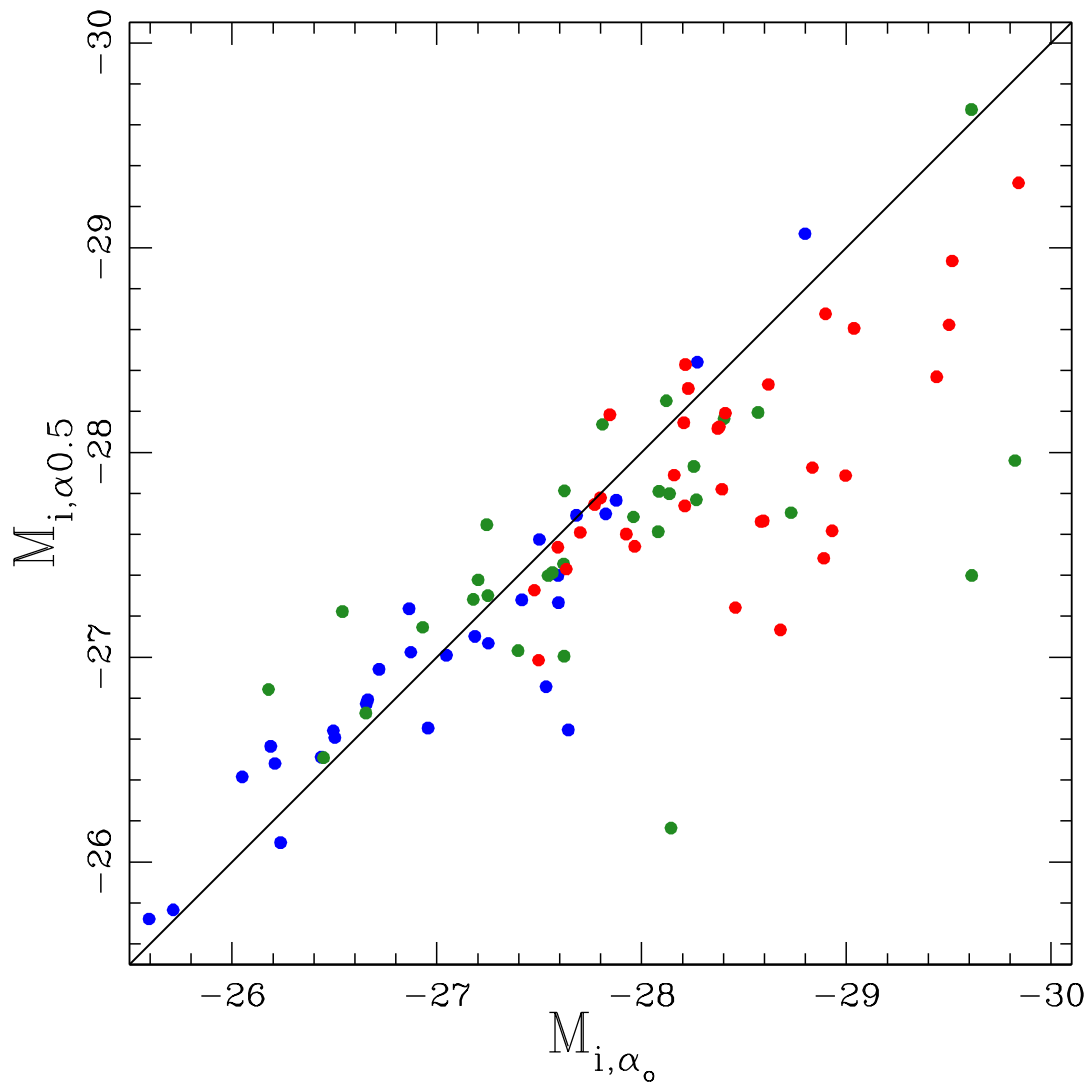


Figure 2.6: **Comparison i -band Magnitude Calculations** — the x-axis is represents M_{i, α_o} , the magnitude calculated using α_o and the y-axis is $M_{i, \alpha 0.5}$, the magnitude calculated using the traditional value $\alpha = -0.5$; blue points are quasars in the $z \sim 1.88$ bin, green are $z \sim 2.80$, and red are $z \sim 4.07$; solid black line represents the $M_{i, \alpha_o} = M_{i, \alpha 0.5}$ line.

(Hogg, 1999). We assume $H_0 = 70\text{km/s/Mpc}$, $\Omega_M = 0.3$, and $\Omega_\Lambda = 0.7$. For the full $K(z)$ expression we follow the methods of Richards et al. (2006) who computed M_i for quasars in the SDSS DR3 quasar catalog to construct a quasar luminosity function. They added a term to $K(z)$ to correct for quasar emission lines by using a composite spectrum that was convolved from the spectra of 16,713 SDSS quasars. Richards et al. (2006) correct back to redshift $z = 2$, the peak of quasar number density. They assume a spectral index of $\alpha = -0.5$ which we substitute in our calculation for α_o from the co-epochal SED. The i -band luminosities are listed in Table 2.1 as M_{i,α_o} and are compared to $M_{i,\alpha 0.5}$, Richards et al. (2006) method with $\alpha = -0.5$. Figure 2.6 is a visual comparison of the two. The M_{i,α_o} -luminosities lay systematically below the $M_{i,\alpha_o} - M_{i,\alpha 0.5}$ line particularly for the quasars in the highest redshift bin. This suggests that luminosities reported using $\alpha = -0.5$ could, in general, be overestimations.

2.6 Conclusion

We measured the optical-UV spectral index for 96 high-redshift quasars. The spectral index was calculated by fitting SED constructed from the co-epochal measurements in *griz* and JHK bands. We found the average spectral index in our sample to be $\langle \alpha_o \rangle = -0.67$, significantly different from the standard $\alpha = -0.5$. We also find evidence that α_o is redshift dependent. When we compared M_i calculated from K-correction with $\alpha = -0.5$ and α_o , we found that using $\alpha = -0.5$ overestimated M_i especially at redshift $z \sim 4$. These results suggest that using the composite SED for K-correction could impact the quasar luminosity functions particularly at higher redshift.

Table 2.1: Quasar SED Measurements

SDSS Identification	z	α_o	$Err(\alpha_o)$	$M_{i,\alpha 0.5}$	M_i, α_o
J073147.76+371707.4	1.8607	-0.434	0.025	-26.512	-26.436
J074136.49+385847.5	1.8656	-0.625	0.025	-26.095	-26.237
J235108.82+153739.2	1.8694	-0.175	0.018	-27.237	-26.865
J005933.30+144731.6	1.8713	-0.409	0.028	-26.607	-26.502
J220430.23+004201.1	1.8721	-0.389	0.041	-25.722	-25.595
J005320.83+152724.2	1.8722	-0.373	0.05	-26.641	-26.495
J012537.60+152831.7	1.8727	-0.661	0.018	-27.068	-27.252
J073844.52+313928.4	1.8738	-1.37	0.023	-26.645	-27.642
J074225.35+325233.5	1.8744	-0.764	0.022	-26.654	-26.957
J074804.66+374046.4	1.8752	-0.667	0.017	-27.4	-27.592
J004023.76+140807.3	1.8753	-0.264	0.008	-29.068	-28.798
J012840.52+134756.3	1.8753	-0.532	0.016	-27.01	-27.047
J014240.88+143840.0	1.8761	-0.181	0.031	-26.416	-26.05
J074122.09+242449.9	1.8763	-0.454	0.03	-25.766	-25.713
J034027.31+003441.5	1.8764	-0.353	0.01	-28.441	-28.272
J075044.67+394258.0	1.8764	-1.67	0.033	-25.439	-26.781
J232634.65+153325.4	1.8771	-0.785	0.018	-27.267	-27.594
J222824.14+131431.4	1.8773	-0.435	0.014	-27.575	-27.501
J010648.03+004627.6	1.8774	-0.573	0.023	-27.102	-27.186
J011721.27+151542.9	1.879	-0.618	0.018	-27.28	-27.415
J225253.03+142313.7	1.8794	-0.172	0.026	-26.565	-26.189
J031544.54+004220.8	1.8796	-0.305	0.021	-26.941	-26.718
J001142.79+152216.3	1.8846	-1.09	0.02	-26.856	-27.534
J222645.57+004519.9	1.8848	-0.368	0.022	-27.025	-26.873
J010028.36+133259.2	1.8853	-0.387	0.022	-26.793	-26.663
J085853.42+063909.5	1.8854	-0.596	0.013	-27.766	-27.876
J011731.27+135238.8	1.8868	-0.609	0.014	-27.7	-27.825
J223003.78+125012.4	1.8878	-0.265	0.03	-26.481	-26.21
J015856.27+130702.6	1.8885	-0.398	0.022	-26.773	-26.656
J074337.86+385212.0	1.89	-1.39	0.031	-25.367	-26.393
J080106.51+415753.4	1.89	-0.49	0.014	-27.693	-27.682
J225635.84+143243.5	2.6323	-2.08	0.027	-27.399	-29.612
J074437.52+205900.1	2.6786	-0.366	0.031	-27.813	-27.623
J221003.55+120547.6	2.6993	-0.376	0.042	-27.378	-27.202
J073424.40+363244.0	2.7032	-0.038	0.109	-25.853	-25.195
J003742.04+154938.2	2.7069	-0.019	0.038	-27.223	-26.539
J015936.60+131133.8	2.7075	-1.89	0.044	-26.166	-28.144
J003815.92+140304.6	2.7165	-0.603	0.045	-27.398	-27.544
J074150.73+394920.6	2.7306	-0.449	0.07	-26.727	-26.654
J074628.66+344248.4	2.7414	-0.35	0.034	-27.146	-26.931
J073936.25+280754.7	2.743	-1.8	0.019	-27.96	-29.823
J013729.94+002243.1	2.7444	-0.725	0.021	-27.932	-28.255

Continuation of Table 2.1

SDSS Identification	z	α_o	$Err(\alpha_o)$	$M_{i,\alpha 0.5}$	M_i, α_o
J073535.44+374450.4	2.7506	-0.76	0.019	-28.195	-28.569
J012606.60+142825.9	2.7747	-0.457	0.068	-26.509	-26.447
J234315.88+004659.5	2.7799	-0.927	0.032	-27.005	-27.622
J021720.47+005935.8	2.7878	-0.428	0.051	-27.282	-27.178
J075849.47+305452.9	2.7957	-0.041	0.034	-26.843	-26.178
J075626.19+282055.3	2.8231	-0.822	0.021	-27.613	-28.081
J025516.88+011134.3	2.8391	-0.603	0.029	-27.413	-27.564
J075901.28+284703.4	2.8491	-1.2	0.02	-27.706	-28.73
J001502.26+001212.4	2.8498	-0.841	0.034	-27.769	-28.268
J074520.21+415725.4	2.855	-0.611	0.027	-27.456	-27.619
J001025.90+005447.6	2.8573	-0.73	0.022	-27.799	-28.136
J223144.19+142107.2	2.8581	-0.225	0.041	-27.647	-27.244
J003939.96+152720.3	2.8599	-0.465	0.034	-27.301	-27.249
J073934.66+231450.6	2.8696	-0.748	0.037	-27.032	-27.397
J012156.03+144823.9	2.8703	-0.457	0.015	-29.674	-29.611
J081339.42+251004.7	2.8953	-0.278	0.023	-28.137	-27.809
J234352.62+141014.6	2.896	-0.661	0.021	-28.165	-28.403
J234352.62+141014.6	2.896	-0.661	0.021	-28.252	-28.121
J031609.83+004043.1	2.897	-0.411	0.029	-27.685	-27.96
J220116.75+125636.4	2.9213	-0.685	0.045	-27.81	-28.085
J081844.34+355243.9	3.9341	-0.83	0.053	-27.82	-28.392
J001820.71+141851.5	3.9361	-0.376	0.04	-28.429	-28.214
J034946.61-065730.3	3.9457	-1.39	0.044	-27.134	-28.678
J001747.92+141015.7	3.955	-1.03	0.042	-27.662	-28.583
J034402.85-065300.6	3.9567	-0.665	0.055	-28.332	-28.619
J075313.81+330327.6	3.9623	-0.512	0.05	-27.778	-27.799
J222824.19+134154.9	3.9883	-0.655	0.056	-27.889	-28.159
J025518.57+004847.4	3.9887	-0.747	0.046	-28.606	-29.037
J024457.18-010809.9	3.9959	-0.833	0.043	-28.935	-29.517
J074640.16+344624.8	4.0101	-0.624	0.044	-28.192	-28.409
J073146.99+364346.4	4.0181	-0.646	0.066	-28.117	-28.372
J075412.18+253229.7	4.0282	-0.585	0.076	-27.327	-27.476
J075347.41+281805.1	4.0309	-0.645	0.042	-28.125	-28.379
J031213.98-062658.8	4.0313	-0.452	0.047	-28.312	-28.228
J232112.40+143312.0	4.045	-0.791	0.086	-26.986	-27.497
J024447.79-081606.0	4.0678	-0.798	0.024	-29.316	-29.841
J034109.35-064805.1	4.0696	-0.615	0.077	-27.43	-27.632
J003749.19+155208.3	4.0729	-0.741	0.073	-27.541	-27.966
J224630.86+131706.6	4.0885	-0.514	0.06	-27.746	-27.771
J012019.99+000735.6	4.102	-0.683	0.099	-27.601	-27.925
J221320.00+134832.5	4.1267	-0.309	0.05	-28.184	-27.845
J224721.05-091548.6	4.1303	-1.24	0.048	-27.617	-28.93

Continuation of Table 2.1

SDSS Identification	z	α_o	$Err(\alpha_o)$	$M_{i,\alpha 0.5}$	M_i, α_o
J234025.97+135009.1	4.1379	-0.53	0.053	-27.537	-27.591
J025204.28+003137.0	4.149	-1.01	0.045	-27.926	-28.834
J230314.37+134808.8	4.1501	-0.551	0.086	-27.609	-27.7
J222254.82+130444.3	4.1567	-0.534	0.048	-28.145	-28.206
J015704.09+122858.2	4.1612	-1.29	0.062	-27.483	-28.89
J075103.96+424211.6	4.1627	-0.624	0.034	-28.677	-28.898
J015032.87+143425.6	4.1786	-1.02	0.049	-27.666	-28.594
J030025.23+003224.2	4.1817	-0.764	0.07	-27.739	-28.211
J005922.65+000301.4	4.1836	-1.1	0.034	-28.369	-29.441
J234750.30+134102.6	4.1881	-1.12	0.047	-27.887	-28.996
J015339.61-001104.9	4.1936	-0.991	0.036	-28.623	-29.501
J075204.16+252200.7	4.194	-1.18	0.059	-27.242	-28.458

Bibliography

- Abazajian, K. N., Adelman-McCarthy, J. K., Agueros, M. A., et al. 2009, *ApJS*, 182, 543
- Bertin, E., & Arnouts, S. 1996, *A&AS*, 117, 393
- Elvis, M., Wilkes, B. J., McDowell, J. C., et al. 1994, *ApJS*, 95, 1
- Hogg, D. W. 1999, *ArXiv Astrophysics e-prints*, astro-ph/9905116
- Kennefick, J., & Bursick, S. 2008, *AJ*, 136, 1799
- Oke, J. B. 1974, *ApJS*, 27, 21
- Richards, G. T., Strauss, M. A., Fan, X., et al. 2006, *AJ*, 131, 2766
- Schlegel, D. J., Finkbeiner, D. P., & Davis, M. 1998, *ApJ*, 500, 525
- Schneider, D. P., Hall, P. B., Richards, G. T., et al. 2005, *AJ*, 130, 367
- Shang, Z., Brotherton, M. S., Wills, B. J., et al. 2011, *ApJS*, 196, 2
- Skrutskie, M. F., Cutri, R. M., Stiening, R., et al. 2006, *AJ*, 131, 1163

Chapter 3

The Co-Evolution of Galaxy Disks and Type 1 AGN

3.1 Abstract

A relationship between the mass of supermassive black holes, M_{BH} , at the center of galaxies and the pitch angle, ϕ , a measure of tightness of spiral arms, was recently reported by Berrier et al. (2013) for late type galaxies. The relationship, established for a local sample, shows that spiral galaxies with tighter pitch angles host higher mass black holes. In this work, we explore the M_{BH} - ϕ relation for a sample of 50 low to moderate redshift ($0.04 < z < 1.4$) spiral galaxies that host Type 1 Active Galactic Nuclei, AGN. These objects were selected from the SDSS quasar catalog and various studies involving HST imaging. Broad $H\beta$, $H\alpha$, and $MgII$ and narrow $[OIII]\lambda 5007$ emission lines were used with established mass scaling relations to estimate black-hole mass. Pitch angles were measured using a 2DFFT technique (Davis et al., 2012). We find that the M_{BH} - ϕ relation for the higher redshift AGN sample differs from that of the local sample and discuss the possibility of AGN feedback by looking at a proposed Fundamental Plane for late-type galaxies — a correlation between bulge mass, disk mass, and spiral-arm pitch angle (Davis et al., 2015).

3.2 Introduction

Since the discovery that supermassive black holes reside at the center of galaxies, there have been several correlations found between black hole mass (M_{BH}) and galaxy properties suggesting that the black hole and the galaxy evolve together. The correlations also provide a way of estimating M_{BH} in larger samples of galaxies. Some examples are M_{BH}

correlations to stellar velocity dispersion, σ_* , (e.g. Ferrarese & Merritt, 2000; Gebhardt et al., 2000; Gültekin et al., 2009; Woo et al., 2010), bulge luminosity (e.g. Kormendy & Richstone, 1995; McLure & Dunlop, 2001; Wandel, 2002; Bentz et al., 2009), and bulge mass, M_{bulge} , (e.g. Magorrian et al., 1998; Häring & Rix, 2004), all of which are related to early-type galaxies (ellipticals) or the classical bulge of some late-type (disk) galaxies — see Kormendy & Ho (2013) and references therein. However, there was a recent correlation specific to spiral galaxies discovered between M_{BH} and pitch angle, ϕ , a measure of the tightness of the spiral arms (Berrier et al., 2013). This study shows that higher mass black holes are found in galaxies with more tightly wound spiral arms. The correlation between M_{BH} and pitch angle is not surprising considering we have long known, through the Hubble tuning fork classification, that galaxies with tighter spiral arms are found in galaxies with more massive bulges (also see Dong & De Robertis 2006 for a recent example which looked at M_{BH} with a sample of AGN in spiral galaxies).

This M_{BH} - ϕ relation can be physically explained using the density wave theory of spiral structure; e.g. Lin & Shu (1966), Shu (2016) and references therein; and is, in fact, a well-established explanation for the spiral structure of the rings of Saturn (Shu, 1984). The density wave theory is analogous to waves on a string where the wave pattern (pitch angle in the case of Saturn’s rings or galaxy spiral arms) is determined by tension in the string (a restoring force or gravity from a central mass) and the density of the string itself (density of the disk). The density waves (or regions of higher density) move through the disk, compressing material and sparking star formation which gives rise to the familiar spiral structure in disk galaxies. The idea is developed further in Davis et al. (2015) where they present a possible fundamental plane for disk galaxies with pitch angle proportional to the

density of gas in the disk and inversely proportional to the bulge mass. Credence is also given to the density wave theory in a recent letter where Pour-Imani et al. (2016) confirm one of the predictions of the theory — specifically the way in which the pitch angle will vary in a given galaxy at different wavelengths due to star formation happening in the density wave and the stars moving out of it as they age.

All of the above mentioned correlations between galaxy properties and M_{BH} , including the $M_{BH}-\phi$ relation, were established using local galaxies where M_{BH} was calculated using direct measures of the gravitational effect from the black hole. Thus a logical question to ask is, do these correlations hold for previous periods in the Universe? Some studies have found no evolution in $M_{BH}-\sigma_*$ (e.g. out to $z \sim 3$ in Shields et al. 2003 and the simulations in Robertson et al. 2006). While others find that $M_{BH}-\sigma_*$ may depend on redshift (Treu et al., 2004; Canalizo et al., 2012). It is unclear what relationship between M_{BH} and ϕ we should expect particularly if, as some have argued, spiral structure arose at $z \lesssim 2$ (Elmegreen & Elmegreen, 2014). There are a few examples of spiral structure seen out to $z \sim 2$ (see Shields et al., 2017) but it is unclear if spirals from this far in the past arise from internal secular processes or from interactions with other galaxies or some other process. Studies like ours can lead to a physical understanding of galaxy formation and evolution.

In this paper we explore the $M_{BH}-\phi$ relation further by looking at a sample of spiral galaxies that host Type 1 Active Galactic Nuclei (AGN). There is evidence that AGN and host galaxies interact (Fabian, 2012) and this feedback was one of the first proposed mechanisms invoked to explain the tight correlation between M_{BH} and bulge properties (e.g. Silk & Rees, 1998; King, 2003). Our study is an opportunity to investigate that interaction in spiral galaxies. We use single-epoch spectra to measure the gas dynamics

around the black hole in order to estimate black hole mass for AGN. Because this method can be applied to distant galaxies we are able to extend our redshift range past the limits of the previous studies of the $M_{BH}-\phi$ relation. We also use our higher redshift sample to place the AGN into the fundamental plane for disk galaxies as a possible way to explore AGN-feedback in spiral galaxies. In §3.3 we describe the sample selection as well as imaging and spectroscopic data. Section 3.4 describes data reduction and the methods for estimating M_{BH} and measuring pitch angle. We present the $M_{BH}-\phi$ relation for spiral-AGN as well as discussion of the fundamental plane in §3.5.

3.3 Sample

AGN are detected at great distances and optical spectra of the broad-line region (BLR) of Type 1 AGN are used to estimate black-hole mass (e.g. Greene & Ho, 2005a; Vestergaard & Peterson, 2006). Therefore, in order to explore the $M_{BH}-\phi$ relation beyond the local epoch, we identified spiral galaxies that host Type 1 AGN. Our sample of 50 galaxies is divided into two main subsamples: the Sloan Digital Sky Survey (SDSS) sample and the *Hubble Space Telescope* (*HST*) sample. The SDSS sample with ground-based imaging goes out to a redshift of $z \simeq 0.3$ while the *HST* sample allowed us to extend our redshift range out to $z \simeq 1.4$. The complete redshift distribution is shown in Figure 3.1.

The SDSS sample consists of objects chosen from the quasar catalogs of the SDSS-I/II (Abazajian et al., 2009) and SDSS-III (Alam et al., 2015) projects. The SDSS-I/II quasar catalog contains 105,783 objects and SDSS-III has 297,301 with some overlap. We searched the catalogs for objects at redshift less than 0.7 since we have found that spiral structure is difficult to measure beyond that for the SDSS subsample. SDSS classifies each object as

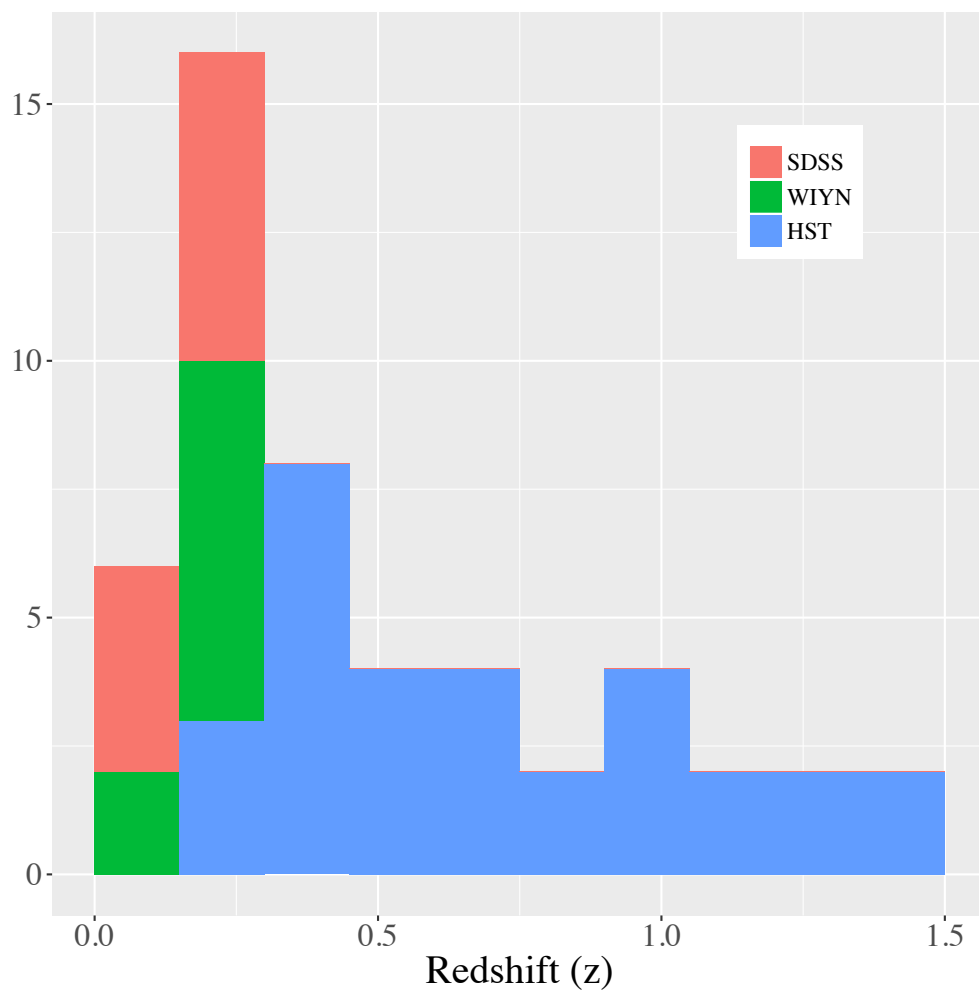


Figure 3.1: **Redshift distribution** — SDSS-selected sample with imaging and spectra from SDSS in salmon; SDSS-selected sample with imaging from WIYN and spectra from SDSS in green; *HST* sample in blue.

“extended” or “point-like”; we filtered out “point-like” objects since we are interested in identifying host spiral galaxies. Eliminating duplicates between the two catalogs, we found 4,034 galaxies from SDSS-I/II and 1,020 from SDSS-III which had extended morphology host galaxies and were within our redshift cut-off. We visually examined cut-out images of each object to identify spiral structure using SDSS’s Image Lists¹ tool which combines i , r and g images to display $R-G-B$ color cut-outs. We found 65 spiral galaxies in the quasar catalogs. We eliminated galaxies with a pixel radius of less than 20 in order to ensure a robust pitch angle measurement (see Davis et al., 2012) and found 10 galaxies with SDSS imaging meeting all our criteria. We were awarded 3 nights in 2013B on the WIYN 3.5-meter telescope and, using the partial One Degree Imager (pODI), we observed a subset of the 65 spiral galaxies found in the SDSS quasar catalogs. We chose 22 galaxies that either needed better resolution for reliable pitch angle measurement or galaxies that we suspected as spiral from the SDSS cutouts. Of the 22 galaxies we imaged at WIYN, four were identified as spirals and five were a significant enough improvement in resolution for measurement. Thus the final SDSS sample consists of 19 galaxies selected from the SDSS quasar catalogs — 10 with SDSS imaging and 9 with WIYN imaging.

The use of *HST* higher resolution, space-based imaging allowed us to greatly extend the redshift range of our sample. The *HST* sample was selected from various sources (see Table 3.2) by searching the literature for spiral galaxies that host Type 1 AGN. Type 1 AGN are classified by the broadness of emission lines in their spectra so we can be sure that if we search for Type 1 objects, there will be spectra available with which to measure M_{BH} . Three objects were chosen from the GOODS fields by first searching for spiral galaxies

¹<http://www.sdss.org/dr13/imaging/jpg-images-on-skyserver/>

using *HST* imaging (Hughes, 2015). We found 144 possible spirals in GOODS-N and 125 in GOODS-S. A single galaxy in GOODS-N and two from GOODS-S were identified in the literature as hosting Type 1 AGN. Additionally, 19 objects were selected from the Galaxy Zoo: Hubble (GZH) project (Willett et al., 2017). We found 3,558 galaxies that were classified as spiral in GZH and 19 of those were identified in the literature as Type 1 AGN. The final addition to the *HST* sample was from Jones (2015) who found nine objects from the X-ray selected AGN in Lusso et al. (2010). 361 of the 545 AGN in Lusso et al. (2010) are classified as Type 1 AGN and we found 18 of those to exhibit spiral structure. Of those 18, one was excluded from the sample because it is an obvious merger system (the arms are possibly tidal tails and not spiral arms), four more were excluded due to un-measurable images (galaxy image with a pixel radius less than 20) or spectra (absorption or noise in the emission line of interest), and finally four others are already included in the GZH group. The final *HST* sample consists of 31 objects.

3.4 Methods

3.4.1 Mass Estimates

All spectra are absolute flux calibrated according to references listed in Table 3.2 with the exception of data from the Team Keck Redshift Survey (TKRS) and phase two of Deep Extragalactic Evolutionary Probe (DEEP2). The TKRS and DEEP2 spectra were calibrated using broad-band magnitudes: starting with the observed, flat-fielded, and sky-subtracted spectrum we matched the region of the spectrum that contains the emission line of interest to a corresponding magnitude in order to find the normalization. Flux

calibrated spectra were corrected for Galactic extinction using reddening estimates from Schlafly & Finkbeiner (2011) and assuming extinction-to-reddening ratio $R_V = 3.1$. For each spectrum, we fit the continuum emission assuming $f_\lambda \propto \lambda^{-\alpha}$ and then fit and subtracted FeII templates (Véron-Cetty et al., 2004; Tsuzuki et al., 2006) near the emission lines.

To estimate M_{BH} , we found the width and luminosity above the continuum of broad emission lines — $H\beta$ (Vestergaard & Peterson, 2006, eqn. 6), $H\alpha$ (Greene & Ho, 2005b, eqn. 6), and $MgII\lambda 2800$ (McLure & Jarvis, 2002, eqn. 7). The choice of line depends on the redshift of the galaxy and thus the emitted lines available in the observed optical spectra (see Table 3.2). The techniques for fitting emission lines follow those of Shen et al. (2011) and are briefly described here. Assuming gravitationally bound, virialized gas in the BLR the black hole mass is estimated with

$$M_{BH} = \frac{v^2 R_{BLR}}{G} \quad (3.1)$$

where v is the orbital velocity of the gas and R_{BLR} is the radius of the BLR. The width (FWHM) is a measure of the velocity of the gas in the BLR and thus the gravitational force from the black hole. Reverberation mapping techniques give us a correlation between luminosity of the BLR and the size of the region. For the broad $H\beta$, we deblended narrow $[OIII]\lambda\lambda 5007, 4959$ from $H\beta$. $H\beta$ was fit with one narrow component and up to three broad components. There are three objects where noise in the spectrum or absorption of $H\beta$ prevented accurate measurement. For those objects we used the width of the $[OIII]\lambda 5007$ line as a proxy for σ_* in the M - σ_* relation (Salviander & Shields, 2013). We fit two Gaussians for each $[OIII]$ narrow line (core component and blue wing; Wang & Lu, 2001)

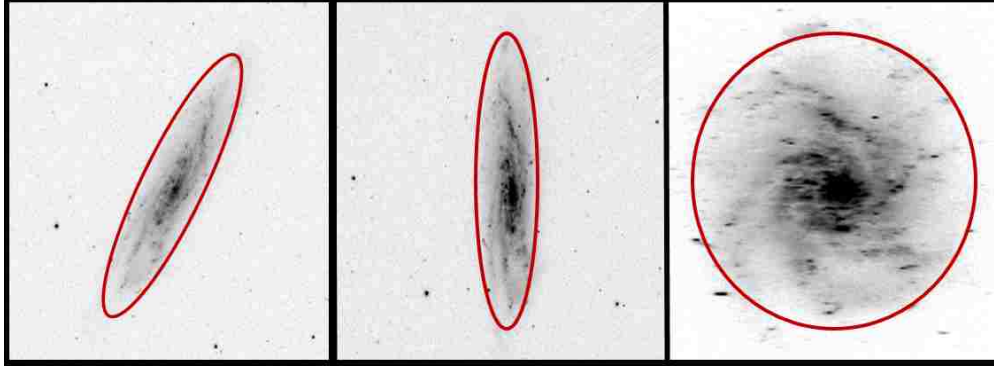


Figure 3.2: B-band image of NGC1337; left: observed image, center: semimajor axis aligned with the y-axis, right: deprojected image; ellipse and circle overlays are a visual aid only; i.e. not fit to galaxy

requiring that the wavelength ratio stay fixed - $5009\text{\AA} / 4959\text{\AA}$, flux ratios

$flux_{5007}/flux_{4959} = 3$ (Dimitrijević et al., 2007) and that the FWHM is the same for both lines. The $H\alpha$ lines were deblended from the $[\text{NII}]\lambda\lambda 6550, 6585$. We fit one Gaussian to each narrow line again requiring that the FWHM was equal. And two to four Gaussians were fit to the $H\alpha$ line (a narrow component and up to three broad). The MgII lines were fit with up to three broad components and the luminosity at 3000\AA was taken from the continuum fit.

3.4.2 Pitch-Angle Measurements

Images for the SDSS sample are from the SDSS catalog and WIYN observations. Objects in the SDSS catalog were imaged with a 2.5-meter telescope and the SDSS camera (0.396 arcsec/pixel) in *ugriz* filter bands. We stacked images from the *gr&i* bands for each object in order to improve the S/N for the pitch angle measurement. The WIYN objects were imaged on the WIYN 3.5-meter ODI (0.11 arcsec/pixel) through *r&i* filter bands for 360s (120s x 3) in each band. Data reduction, i.e. flat-fielding and sky subtraction, for the 120s

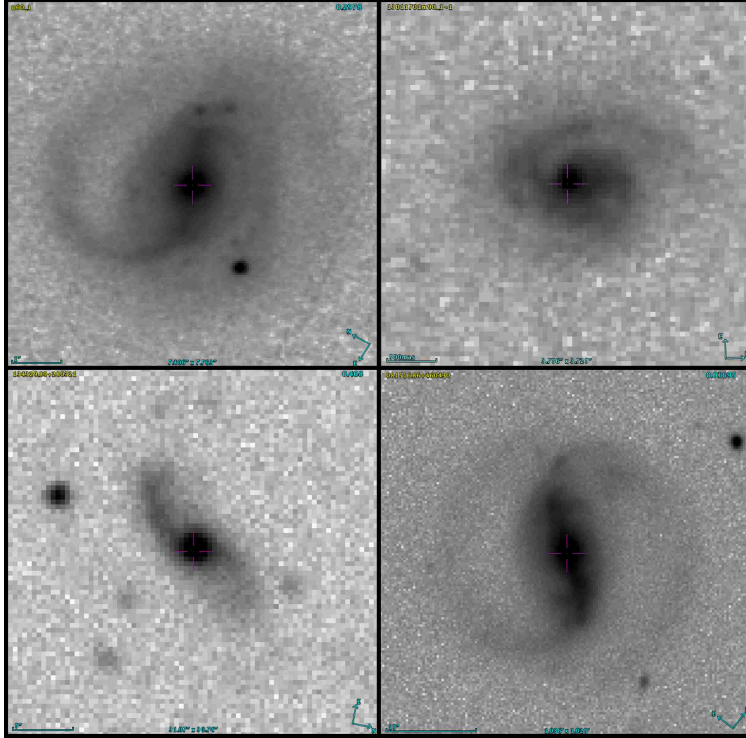


Figure 3.3: Examples of galaxies from this sample that show the difficulty of deprojection; note the prominence of the spiral arms and lack (above the sky) of light from the disk in all the images; objects clockwise from upper left: *HST* 14, *HST* 5, SDSS 7, and SDSS 3. See Table 3.3 for images of each galaxy in the sample

exposures was performed by the team at the ODI Pipeline, Portal, and Archive². The three exposures for each object were stacked using SWarp (Bertin et al., 2002) and finally *r&i* band images were stacked to improve the S/N. Images for the *HST* sample were downloaded from the MAST Portal³ and information about the instrument and filter used to take individual images can be found in Table 3.2.

We use the same technique developed by Davis et al. (2012) for measuring pitch angle (described here briefly; please see Davis et al. (2012) for full details). Galaxy arms can be modeled as logarithmic spirals — in polar coordinates, $r = r_0 e^{\theta \tan(\phi)}$. The pitch angle of the spiral, ϕ , is the angle between a line tangent to the spiral and the radial line at any

²<https://portal.odi.iu.edu>

³<https://mast.stsci.edu>

point on the spiral. Thus pitch angle can vary from 0° (a perfect circle) to 90° (a ray). We use a two-dimensional fast-Fourier transform, 2DFFT, algorithm to decompose spiral arms into a superposition of logarithmic spirals of different pitch angles and number of arms. The fit with the strongest signal (amplitude) indicates the most likely pitch angle. The measurement involves first deprojecting the galaxy to face-on. Davis et al. (2012) used the IRAF⁴ task, `Ellipse`, to fit an ellipse to the disk of a galaxy and stretch the semi-minor axis to equal the length of the semi-major axis, Figure 3.2. This assumes the elliptical shape is from the inclination of the viewing angle. The deprojected image is then fed into the 2DFFT software to detect and measure the symmetric, logarithmic components of the spiral arms.

This method has been sufficient for the high resolution images of local galaxies in previous studies but not for the higher redshift objects in this sample. We found that the low S/N of the images results in the spiral arms — the brightest part of the disk — being the only components significantly above the sky background. The result is that the `Ellipse` task will only fit the spiral arms. See Figure 3.3 for some examples, specifically the image in the lower left panel of SDSS 3 — one of the highest redshift objects in the sample that is imaged with the SDSS telescope. For this object the correct deprojection is not obvious — the image could be of either a highly inclined galaxy or a galaxy with loosely wound spiral arms. Therefore we used the 2DFFT algorithm to find the correct deprojection under the assumption that the correct deprojection will result in the most logarithmic spirals (also see Barberà et al. 2004 and Considerere & Athanassoula 1988). We assumed 36 different

⁴Image Reduction and Analysis Facility, is software written and supported by the National Optical Astronomy Observatories (NOAO) in Tucson, Arizona. NOAO is operated by the Association of Universities for Research in Astronomy (AURA), Inc. under cooperative agreement with the National Science Foundation.

deprojection configurations for each object: six position angles between 0° and 180° to align the semi-major axis of the inclined galaxy with the vertical axis of the image and, for each position angle, we chose six inclination angles – 10° , 20° , 30° , 40° , 50° , and 60° – which determines how much the image is stretched along the horizontal axis. We ran each “deprojected” image plus the unaltered image through 2DFFT. Since the correct deprojection will result in logarithmic spiral arms, we then choose the most stable measurement from the 2DFFT output (here, most stable refers to a deprojection that results in the largest region, within the radius of the galaxy, with a constant ϕ measurement). Please see Table 3.3 for cut-outs of the observed image and the deprojected image for each galaxy.

3.5 Results

Black hole mass, M_{BH} , and pitch angle, ϕ , measurements are listed in Table 3.2. The reported error in ϕ was calculated using the method of Davis et al. (2012) such that there are three sources of error that are accounted for: (1) standard deviation of ϕ over the stable region mentioned in the last section, (2) the fraction of the galaxy radius that is considered the stable region, and (3) an error accounting for the lower resolution of the 2D FFT code when measuring galaxies with fewer arms. The mass estimate error is propagated from the error in fits to the continuum and emission lines of the spectra. Mass, $\mathcal{M}_{BH} \equiv \log(M_{BH}/M_\odot)$ is plotted as a function of the absolute value of the pitch angle in degrees in Figure 3.4. In order to characterize any trend in the data we performed a linear, least-squares fit (solid line in Figure 3.4) using Deming regression. The fit line expresses

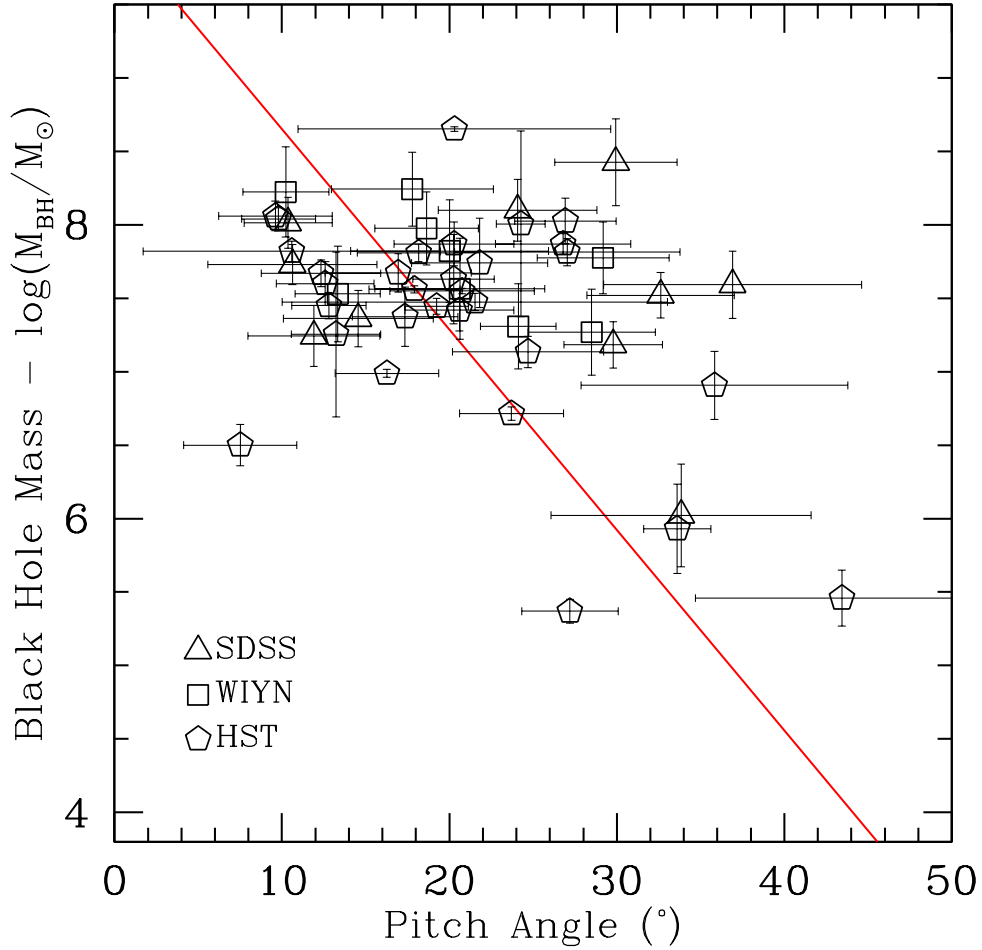


Figure 3.4: $M_{BH}-\phi$ — Mass as a function of pitch angle for all spiral, Type 1 AGN: triangles are from the SDSS-selected sample with imaging and spectra taken from SDSS, squares are from the SDSS-selected sample with imaging from WIYN and spectra from SDSS, circles are from the Hubble sample with imaging from HST and spectra from various sources (see Table 3.2) for details about sources); the solid line is a linear least-squares fit to the entire spiral-AGN sample.

the $M_{BH}-\phi$ relation as

$$\mathcal{M}_{BH} = (10.12 \pm 0.91) - (0.14 \pm 0.048)\phi \quad (3.2)$$

We then took our sample of 50 spiral-AGN galaxies sorted them by redshift (z) and divided the sample into three bins — 17 galaxies in the lowest z -bin $0.04 < z < 0.23$, 17 in the middle bin $0.23 < z < 0.56$, and 16 in the highest z -bin $0.56 < z < 1.5$. We performed a weighted least-squares fit (Deming regression) in $M_{BH}-\phi$ for each bin in order to explore evolution in redshift — Figure 3.5.

3.5.1 The $M_{BH}-\phi$ Relation

The $M_{BH}-\phi$ relation was established by Berrier et al. (2013) using a sample of 34 local galaxies with mass measurements taken from stellar and gas dynamics, masers, and reverberation mapping — hereafter referred to as the local sample. The local sample showed that galaxies with smaller pitch angles (tighter arms) correlate with higher mass black holes. Figure 3.6 compares mass as a function of pitch angle for our Type 1 AGN sample along with the local sample. The black circles represent objects in this study, the purple squares are from the local sample, the solid line is the fit to the Type 1 spiral AGN (the same as in Figure 3.4) and the dashed line is the fit to the local sample. The relationship between black-hole mass and pitch angle from the sample here — Type 1 AGN in spiral galaxies at moderate redshifts — shows the same trend as the local sample, namely higher mass black holes correlate with tighter pitch angles. However, when the AGN sample is compared to the local sample we see a significant change in the slope of the linear fit and with more scatter.

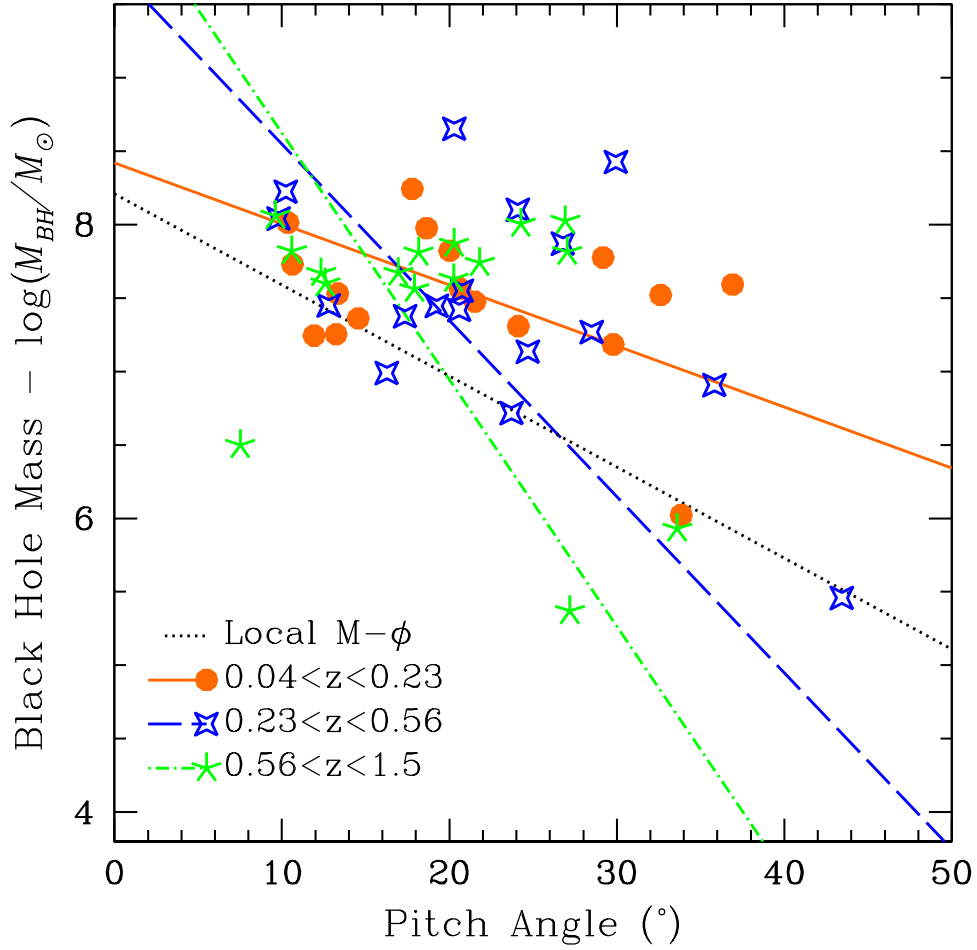


Figure 3.5: $M_{BH}-\phi$ **z-bins** — mass as a function of pitch angle divided into three equal sized redshift bins; objects in each bin were fit to a weighted least squares fit.

Table 3.1: Fits to local and redshift-binned $M-\phi$

z-range	$\log(M_{BH}/M_{\odot}) = (A) - (B)\phi$	
	A (y-inter)	B (slope)
$z < 0.04$	8.21 ± 0.16	0.062 ± 0.009
$0.04 < z < 0.23$	8.90 ± 3.09	0.06 ± 0.13
$0.23 < z < 0.56$	9.75 ± 1.45	0.12 ± 0.07
$0.56 < z < 1.5$	10.3 ± 4.90	0.17 ± 0.29

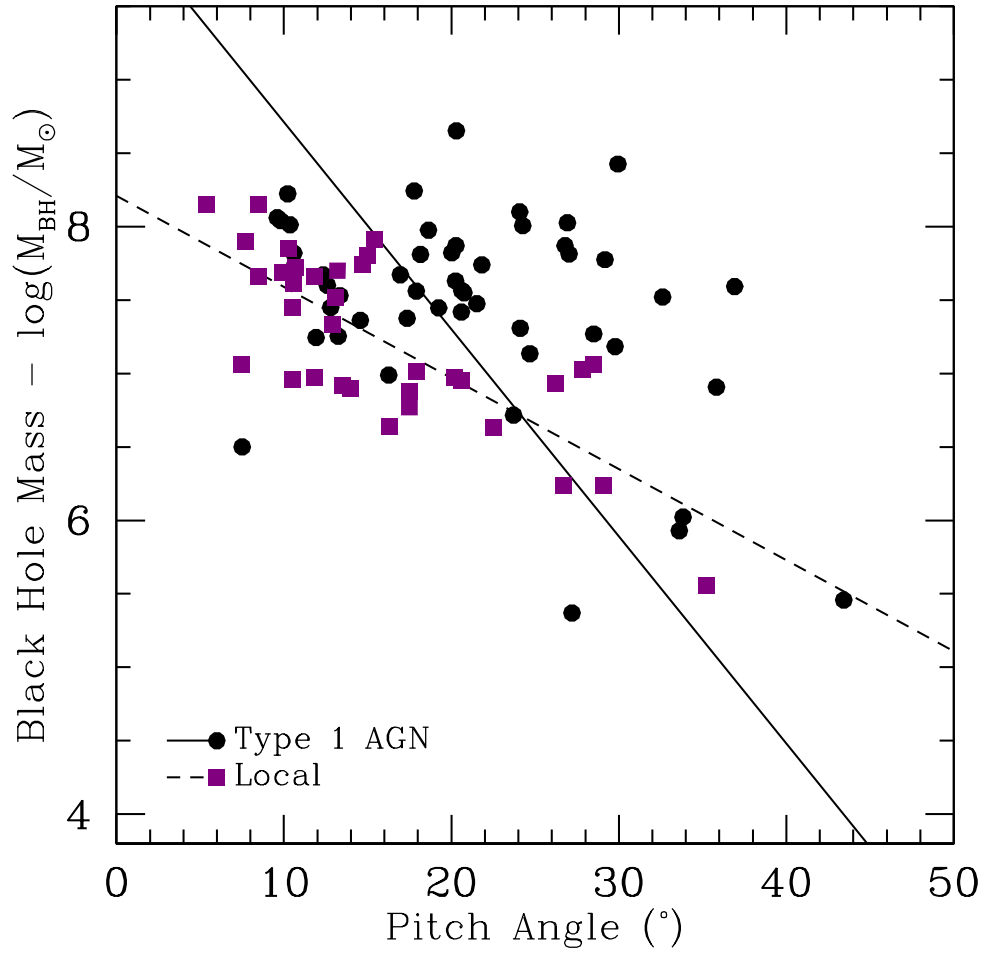


Figure 3.6: $M_{\text{BH}}-\phi$ Local and AGN samples — Comparison of mass as a function of pitch angle for the two samples — black circles represent the Type 1 AGN and the purple squares represent the local sample (Berrier et al., 2013).

The sample presented here is different in two notable ways from the local sample — all galaxies contain AGN and they sample a higher redshift range. To explore the difference in redshift of our sample, we divided it into three equally sized redshift bins. Table 3.1 shows the results of the least-squares fit to each bin compared to the M - ϕ relation from the local sample (Berrier et al., 2013). We see that the slope of the M - ϕ relation increases as z increases (see Figure 3.5). There is large scatter in each of the fits due to the fundamental nature of this study; i.e. higher redshift galaxies will have lower quality images because of resolution and fewer actual pixels to measure ϕ . Because of the difficulty of measuring ϕ (discussed in §3.4) many of our measurements have large error bars – the error calculation produces large error bars if there is a large scatter or if there is a small stable region but does not directly account for lower image quality. Nevertheless the change in the M - ϕ relation could point to several questions: Is there a physical cause behind the correlation between redshift and M - ϕ ? Are we seeing evidence that spiral galaxies were structurally different in past epochs? Is it possible that because we are looking at a sample consisting solely of AGN we are seeing an indication of AGN affecting the structure of galaxies at such large scales?

3.5.2 The Fundamental Plane of Disk Galaxies

It could be that the evolution in redshift of M - ϕ is the result of the density of gas in the disks of galaxies to changing over time as stars form. Consider that M_{BH} - ϕ is a projection in two dimensions of the fundamental plane of spiral structure in disk galaxies. The fundamental plane can be explained, physically, as evidence of density-wave theory or a standing-wave picture of spiral structure (Davis et al., 2015). One can think of the

correlation between pitch angle, density of neutral atomic hydrogen in the disk, and the central bulge mass of the galaxy as an analogy to waves on a string where the density of the string (disk density for a galaxy) and the tension or restoring force (mass in the central region) determine the properties of the wave (pitch angle). The correlation between pitch angle (ϕ), maximum neutral atomic hydrogen gas mass surface density in the disk (Σ_{HI}^{max}), and the stellar galactic bulge mass of the galaxy (M_{bulge}), is quantified as (Davis et al., 2015, eqn. 4)

$$\Sigma_{HI}/M_{\odot}pc^{-2} = 5.70 \tan |\phi| - 0.677 \log(M_{bulge}/M_{\odot}) + 9.29 \quad (3.3)$$

We used the redshift-binned M_{BH} - ϕ fits (Figure 3.4) to place our data in the proposed fundamental plane of late-type galaxies by projecting $M_{BH}(\phi)$ into $\Sigma_{HI}(M_{bulge})$. In order to get Equation 3.5.2 in terms of a single parameter, bulge mass, we first took the M - ϕ relation from each z-bin and solved for pitch angle — the linear fit gives a function of $M_{BH}(\phi)$ which we transformed to $\phi(M_{BH})$, then converted black hole mass (M_{BH}) to bulge mass (M_{bulge}) using Kormendy & Ho (2013, Equation 10), and finally substituted these values for ϕ and M_{bulge} into Equation 3.5.2. The result is three “slices” of the fundamental plane plotted in Figure 3.7. For comparison we show individual objects in the same plot — these values were calculated by converting M_{BH} to M_{bulge} and using ϕ with equation 3.5.2 to find the neutral atomic hydrogen disk density. We see that higher neutral atomic hydrogen disk density correlates to lower bulge mass and that the correlation is steeper at lower redshift.

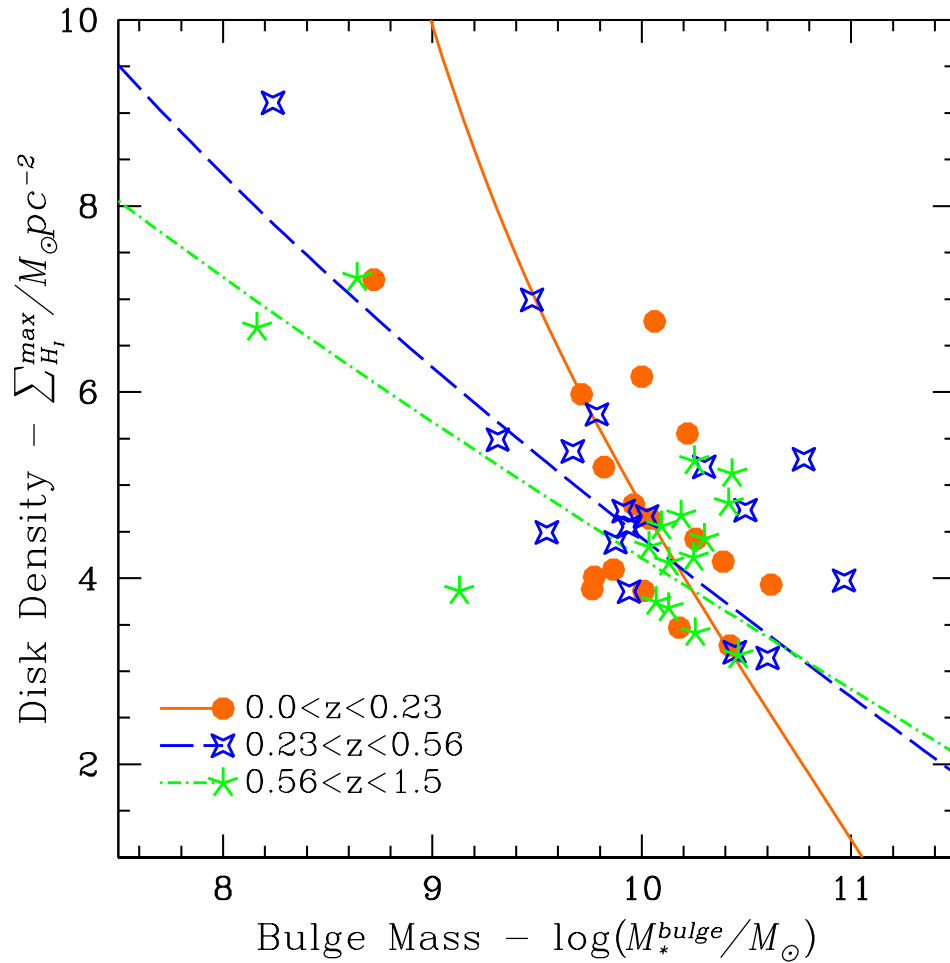


Figure 3.7: $\Sigma_{H_I}(M_{bulge})$ — density of neutral hydrogen in the disk as a function of bulge mass for each redshift bin; solid lines were calculated by converting M_{BH} to M_{bulge} , using the $M_{BH}-\phi$ fits from Figure 3.4 to get pitch angle as a function of M_{bulge} , and using the fundamental plane (Davis, et al. 2015) to find disk density.

3.6 Discussion

The results presented here lead to many questions about galaxy evolution and the interaction between AGN and host galaxy. Is this picture indicating that the distribution of gas was more homogeneous between bulge and disk in past epochs? Does material/gas tend to flow toward the central region? Does it get dissipated from the disk by some other mechanism? Do AGN play a role? However before we can hope to answer these questions we must be able to understand our sample of galaxies in relation to the larger sample of spiral galaxies. Our data set is particularly challenging since we are pushing the limits of current instruments for imaging and thus are biased toward the brightest galaxies at the higher redshift end. But as redshift increases, the limitations are not only defined by instrumentation but also the size or radius of the disk, the brightness of the arms, and the inclination angle.

3.6.1 What are we seeing?

Our sample was not chosen to be representative of spiral galaxies at higher redshifts but rather an attempt to build a sample of galaxies with available M_{BH} estimates (independent of ϕ) at redshifts beyond the local samples already studied. We do see evidence that the pitch angle measurements in this study are drawn from the same distribution as local galaxies even though our sample differs in redshift and physical characteristics (all of our galaxies contain Type 1 AGN). The distribution of measured pitch angles is shown in Figure 3.8 - a binned histogram along with the empirical density function (dashed, red line), an effectively binless histogram calculated using a kernel density estimator (KDE).

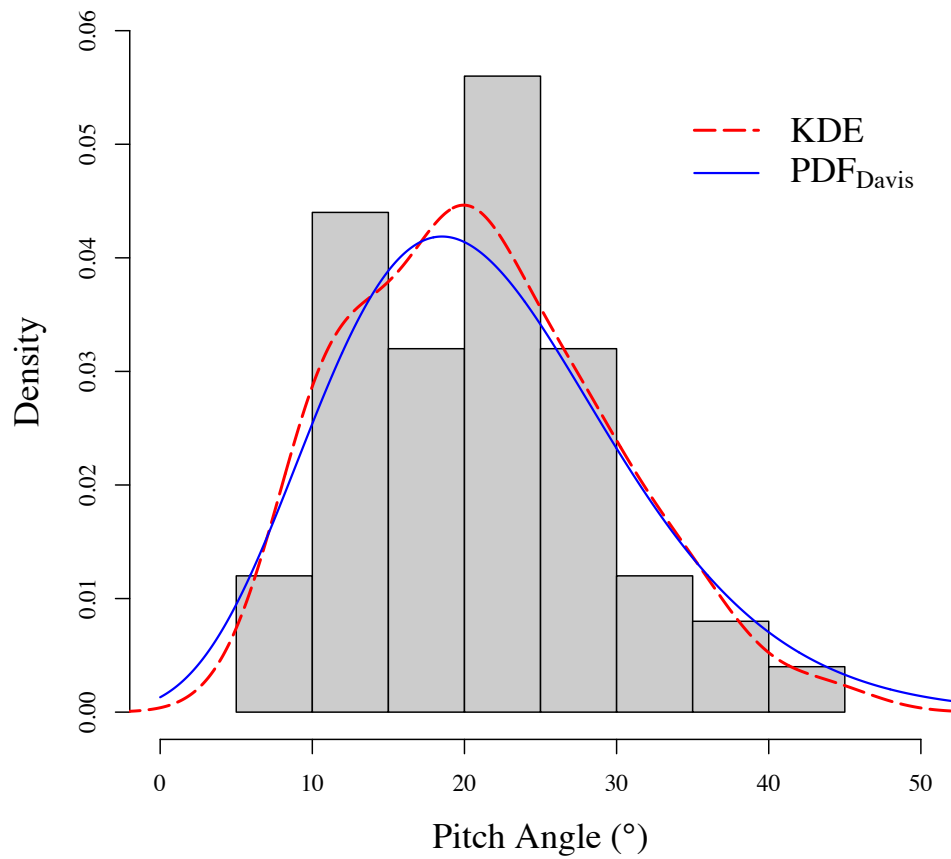


Figure 3.8: **Pitch angle distribution** — binned histogram of pitch angle measurements for the type I AGN sample: grey; the empirical density function for the Type 1 AGN sample: dashed, red line; for comparison, the probability density function (PDF) for a complete, local sample (Davis et al., 2014): solid, blue line.

We compare the Type 1 AGN sample to the work of Davis et al. (2014) who measured pitch angles for a complete, volume-limited sample of spiral galaxies in the southern hemisphere based on the Carnegie-Irvine Galaxy Survey. The density function of pitch angles for the Type 1 AGN sample is consistent with the probability density function (PDF) for this local, complete sample shown as a blue, solid line in Figure 3.8 (for details on the calculation of the PDF see Davis et al. 2014). Further, the parameters for the two samples are similar - the mean and standard deviation for the Type 1 AGN sample are $\mu = 21.01^\circ$ and $\sigma = 8.26^\circ$ compared to $\mu = 21.42^\circ$ and $\sigma = 8.22^\circ$ for the local, complete sample. We can be confident that we are at least sampling a similar pitch angle distribution as a complete sample.

However we still need to understand our sample more precisely to know what galaxies we are missing. Besides the obvious desire for a larger data set, one step toward answering this question and a way that this work can be supplemented is by studying the selection bias of high redshift spiral galaxies using, for example, simulations and/or artificially redshifted galaxies. We have taken a first step in this direction by simulating spiral galaxies with parameters of pixel radius, arm-interarm contrast, and inclination angle informed by images of galaxies in this sample. First we created face-on galaxies using GALFIT, then rotated and stretched the images to simulate the inclination angle, and finally added Poisson noise. The pitch angles of the simulated galaxies were then measured using the technique described in §3.4.2. We created four galaxies and varied the pitch angle, inclination angle, and noise level. Figure 3.9 shows each galaxy simulation. The galaxy labeled A was generated with a pitch angle $\phi_{gen} = 12.5^\circ$ and we measured the pitch angle as $\phi_{meas} = 13.719 \pm 3.43^\circ$. For galaxy B, $\phi_{gen} = 25.2^\circ$ and $\phi_{meas} = 23.425 \pm 3.35^\circ$; galaxy

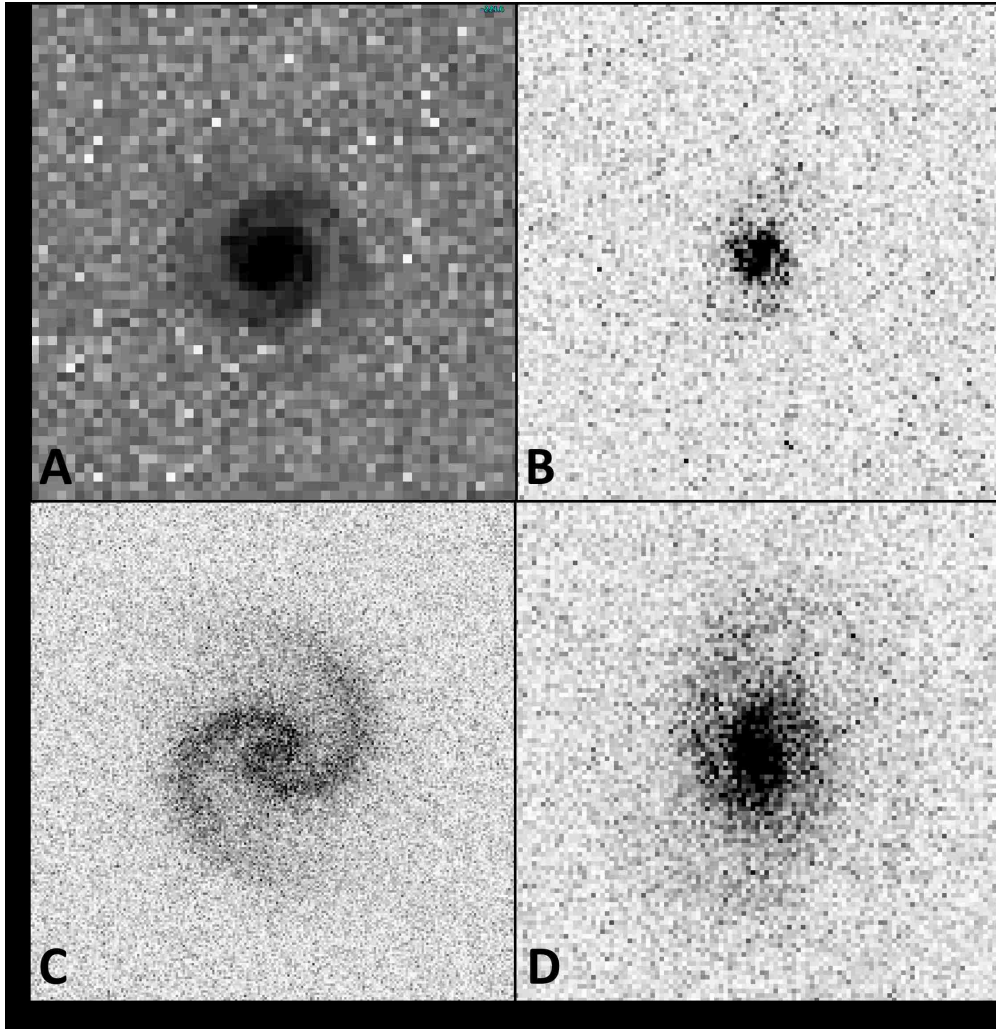


Figure 3.9: **Simulated Galaxies** — galaxies created using GALFIT which were rotated and stretched and had Poisson noise added to simulate real galaxy properties.

C, $\phi_{gen} = 23.4^\circ$ and $\phi_{meas} = 23.842 \pm 1.86^\circ$; and galaxy D, $\phi_{gen} = 18.5^\circ$ and $\phi_{meas} = 21.299 \pm 1.87^\circ$. The measurement errors are calculated using the techniques in §3.5.1 and it is worth noting that the errors found here are significantly smaller than those found for the real galaxies for which the average measurement error is 4.25° . So we were able to recover the pitch angle, ϕ_{meas} of the simulations to within less than 3° of the input pitch angle, ϕ_{gen} . To understand and quantify our selection effects, a much more extensive study is forthcoming.

3.6.2 Implications

The strong correlations between M_{BH} and properties of host galaxies implies that black holes and galaxies influence each other or at least evolve together. Silk & Rees (1998) proposed that AGN feedback could be regulating the AGN as well as the host galaxy. The idea is that AGN are accreting material from the host galaxy onto the black hole until some critical mass when radiative output and winds from AGN are expelled out of the bulge to heat the gas in the disk. Not only would this suppress star formation but would also change the density in disks of galaxies. A hotter disk would have a lower density. This is reflected in the trend in Figure 3.7 which suggests lower-density disks are correlated with higher bulge mass.

Additionally, Elmegreen & Elmegreen (2014) present evidence that the onset of spiral structure happened around $1.4 \lesssim z \lesssim 1.8$. At these redshifts clumpy disks, dominated by turbulent gas, give way to disks dominated by rotation and eventually spiral arms. So galaxy disks start out as hot (less dense) then, as time passes, settle (shrink in volume) to become more dense. Figure 3.7 is pointing to this trend as well – in the lowest redshift bin

there are more galaxies with higher disk density. The disk density is higher for the lowest redshift bin following the trend suggested by Elmegreen & Elmegreen (2014) of hot, clumpy disks at higher redshifts settling into disks more conducive to star formation at lower redshifts.

3.7 Conclusion

We measured the pitch angle for a sample of 50 spiral galaxies that host Type 1 AGN and used established methods for estimating M_{BH} of supermassive black holes with the spectra of Type 1 AGN. This sample allowed us to explore the $M_{BH}-\phi$ relation out to a redshift of $z \simeq 1.4$. We found that

1. The $M_{BH}-\phi$ relation for the higher redshift, Type 1 AGN sample:

$$\mathcal{M}_{BH} = (10.12 \pm 0.91) - (0.14 \pm 0.048)\phi$$

differs from that of the local sample (Berrier et al., 2013).

2. When we bin by redshift, we find some indication that the slope of the $M_{BH}-\phi$ relation depends on redshift.

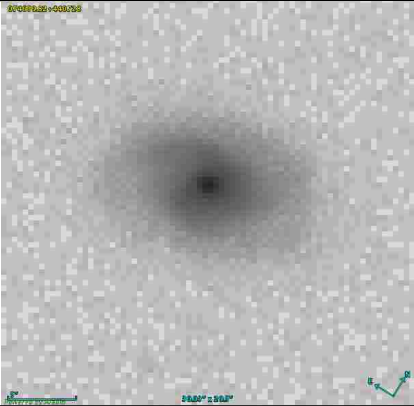
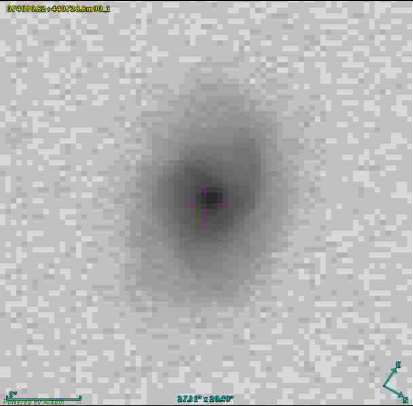
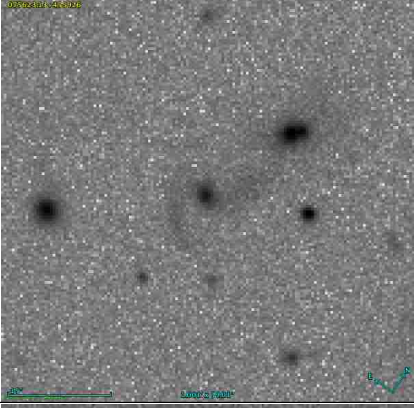
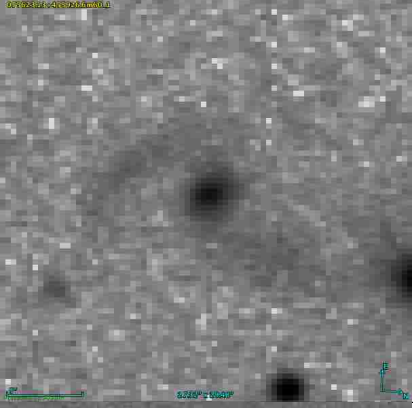
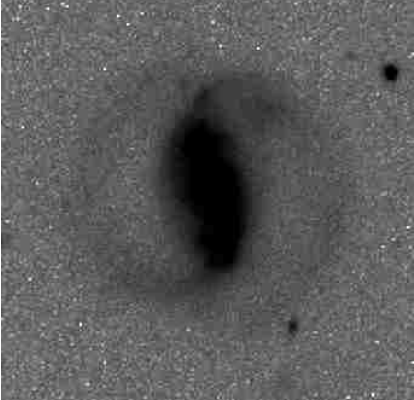

Assuming that spiral galaxies form by way of density waves and considering the fundamental plane of spiral structure in disk galaxies, the evolution in the $M_{BH}-\phi$ relation could have implications for galaxy evolution and AGN feedback mechanisms. Detailed studies of selection effects of high redshift spiral galaxies and AGN in spiral galaxies are necessary to draw conclusions concerning our results.

Table 3.2: Type 1 AGN in Spiral Galaxies – Object Information and Measurements

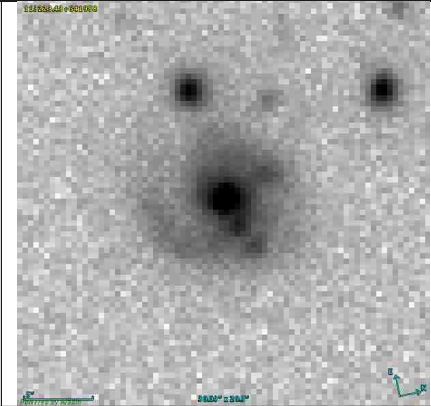
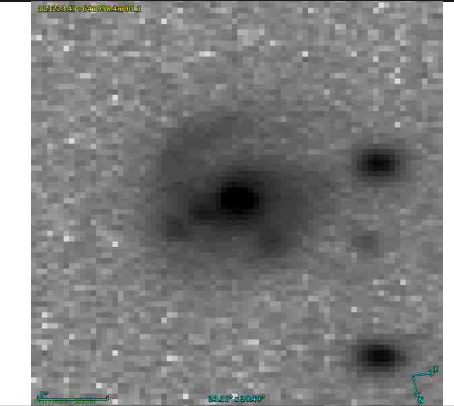
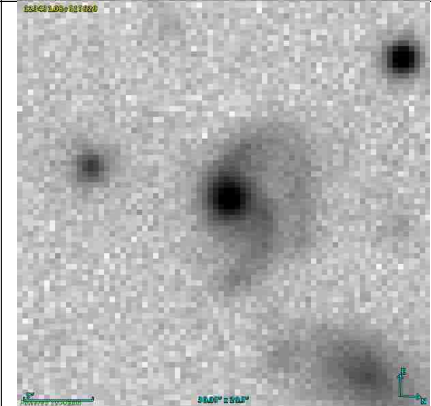
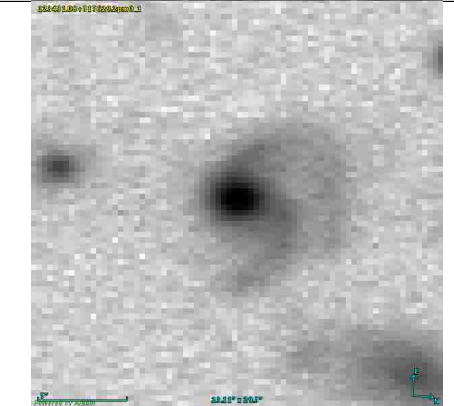
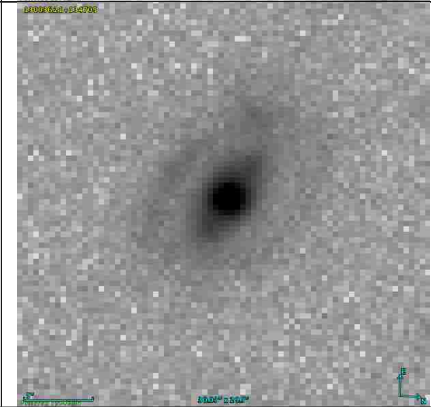
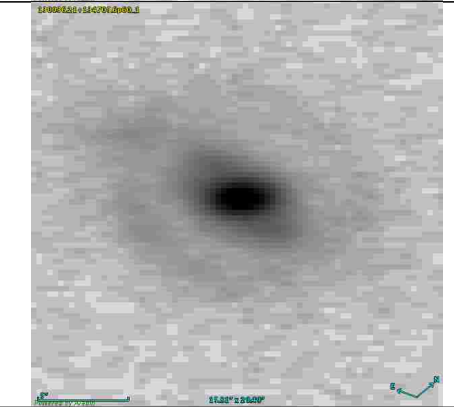
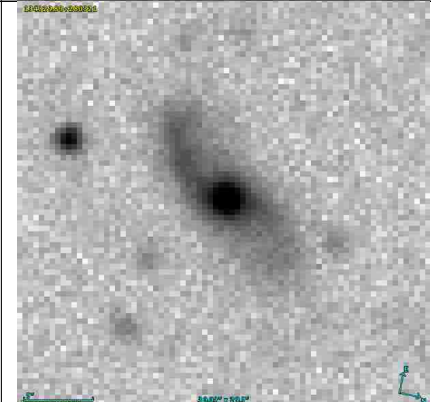
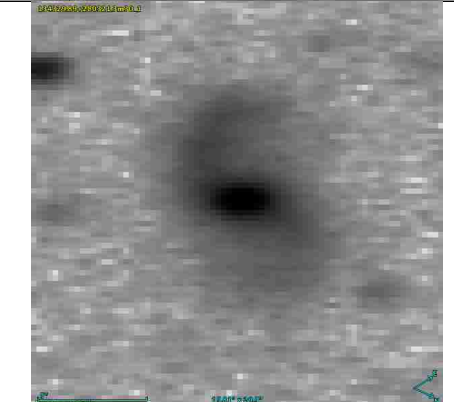
ID (1)	RA (2)	Dec (3)	z (4)	Type (5)	Spec (6)	Filter (7)	M_{BH} (8)	err M_{BH} (9)	ϕ (10)	err ϕ (11)
SDSS1	116.74925	44.12467	0.0759	1	1	gri	6.022	0.350	33.842	7.764
SDSS2	119.09638	45.99072	0.2093	1	1	gri	7.520	0.155	32.613	4.406
SDSS3	123.82025	46.07522	0.0410	1	1	gri	7.730	0.136	10.629	5.048
SDSS4	173.09763	64.33289	0.2098	2	2	gri	7.244	0.208	11.913	3.930
SDSS5	188.62950	51.94144	0.2959	2	2	gri	8.426	0.296	29.944	3.653
SDSS6	195.15088	13.78489	0.1423	2	2	gri	7.362	0.192	19.464	8.155
SDSS7	205.87454	28.05592	0.2276	2	2	gri	7.592	0.229	36.913	7.692
SDSS8	208.63454	54.47514	0.1103	1	1	gri	7.184	0.158	29.781	2.935
SDSS9	208.69937	42.11150	0.2319	2	2	gri	8.100	0.211	24.078	4.740
SDSS10	211.26100	47.12986	0.1522	2	2	gri	8.013	0.173	10.366	2.629
WIYN1	29.95896	0.39469	0.1627	2	2	ri	7.822	0.350	20.018	5.912
WIYN2	121.50000	26.10069	0.1360	2	2	ri	8.243	0.251	17.784	4.836
WIYN3	127.86496	5.82350	0.2287	2	2	ri	7.309	0.289	24.113	2.249
WIYN4	137.99796	59.50247	0.2289	2	2	ri	7.530	0.325	13.338	2.540
WIYN5	139.24600	16.23878	0.2984	2	2	ri	8.224	0.307	10.234	2.567
WIYN6	141.99196	22.00219	0.1573	2	2	ri	7.775	0.245	29.177	3.938
WIYN7	144.56200	2.00647	0.1741	2	2	ri	7.976	0.250	18.639	3.087
WIYN8	146.88800	10.08578	0.1392	2	2	ri	7.565	0.343	20.629	5.070
WIYN9	357.12796	13.81119	0.2512	2	2	ri	7.269	0.293	28.498	3.794
HST1	53.22038	-27.85553	1.2270	3	4	F606W	7.740	0.304	21.810	4.059
HST2	53.11038	-27.67656	1.0310	3	4	F606W	5.930	0.304	33.609	2.008
HST3	188.97133	62.17708	1.3710	5	6	F850LP	7.630	0.304	20.249	2.422
HST4	215.32605	53.09682	0.4354	5	7	F814W	5.458	0.190	43.439	8.739
HST5	214.81979	52.84555	0.7403	5	7	F814W	5.370	0.081	27.199	2.875
HST6	150.19474	2.06790	0.5524	8	9	F814W	7.135	0.106	24.691	4.514
HST7	149.79300	2.12561	0.3529	1	1	F814W	7.549	0.017	20.759	4.305
HST8	150.57638	2.18136	0.5545	10	9	F814W	8.652	0.016	20.300	9.331
HST9	149.78190	2.13907	0.3542	1	1	F814W	6.907	0.231	35.832	7.957
HST10	150.12369	2.35825	0.7277	11	11	F814W	7.672	0.131	16.948	4.369
HST11	149.86801	2.35185	0.3459	1	1	F814W	6.716	0.046	23.711	3.109
HST12	149.66183	2.39688	0.3552	1	9	F814W	7.375	0.203	17.356	3.163
HST13	150.68316	2.57462	0.3757	10	11	F814W	8.040	0.077	9.800	2.202
HST14	150.64524	2.71475	0.1962	10	2	F814W	7.255	0.561	13.236	2.662
HST15	150.65795	2.78355	0.2123	1	1	F814W	7.475	0.059	21.520	11.499
HST16	150.55485	2.64099	1.1442	10	11	F814W	8.025	0.155	26.929	3.038
HST17	189.46972	62.27459	0.3057	1	1	F814W	7.418	0.140	20.598	3.254
HST18	189.07750	62.18763	1.0200	12	6	F814W	8.007	0.633	24.262	1.450
HST19	189.26135	62.26220	0.5120	8	6	F814W	7.446	0.054	19.241	1.888
HST20	189.05014	62.19422	0.2760	13	1	F814W	6.989	0.026	16.267	3.086
HST21	53.33785	-27.65329	1.2350	14	14	F606W	7.561	0.024	17.910	2.715
HST22	53.24608	-27.72766	0.7330	14	4	F814W	7.814	0.093	27.036	6.729
HST23	149.58279	2.48431	0.3450	15	2	F814W	7.870	0.070	26.790	4.030
HST24	150.32717	1.92856	0.5290	15	1	F814W	7.450	0.090	12.800	2.220
HST25	150.13913	1.87697	0.8320	15	16	F814W	7.870	0.150	20.280	3.580
HST26	150.49758	2.65989	0.8510	15	16	F814W	7.600	0.150	12.590	2.920
HST27	149.62167	2.26186	0.9460	15	16	F814W	7.670	0.090	12.340	3.560
HST28	150.31788	2.60208	0.9590	15	16	F814W	7.810	0.060	18.160	3.650
HST29	150.53633	2.27289	1.0870	15	11	F814W	8.060	0.100	9.610	3.390
HST30	150.00442	2.23714	1.4070	15	10	F814W	7.820	0.070	10.590	8.870
HST31	150.12375	2.35831	0.7280	15	11	F814W	6.500	0.140	7.510	3.390

Columns: (1) object identifier, (2) Right Ascension, (3) Declination, (4) redshift, (5) reference for classification as a Type 1 AGN, (6) reference for spectrum source, (7) filter of image used for pitch angle measurement, (8) $\log(M_{BH}/M_{\odot})$, (9) error in $\log(M_{BH}/M_{\odot})$ estimate (10) pitch angle, (11) error in pitch angle measurement; **References:** 1. Alam et al. 2015 2. Abazajian et al. 2009 3. Hasan 2007 4. Szokoly et al. 2004 5. specExam 6. Wirth et al. 2004 7. Matthews et al. 2013 8. Lin et al. 2012 9. Trump et al. 2007 10. Trump et al. 2009 11. Lilly et al. 2007 12. Hornschemeier et al. 2001 13. Trouille et al. 2008 14. Silverman et al. 2010 15. Lusso et al. 2010 16. Prescott et al. 2006

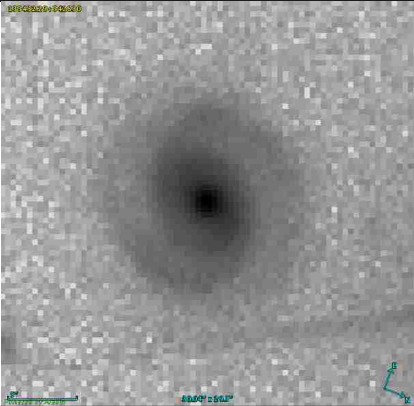
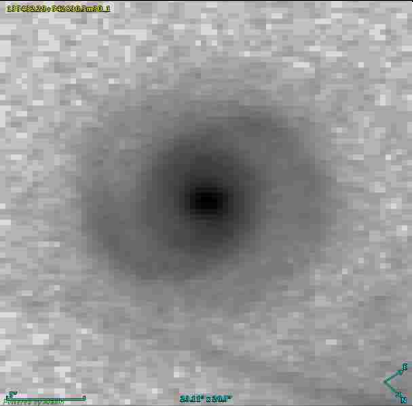
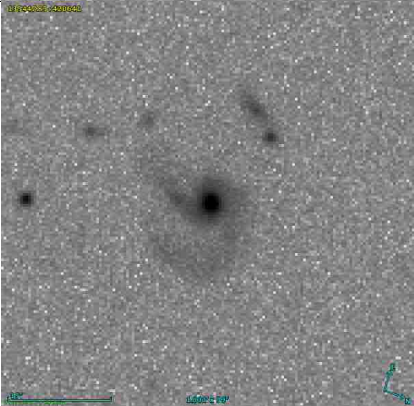
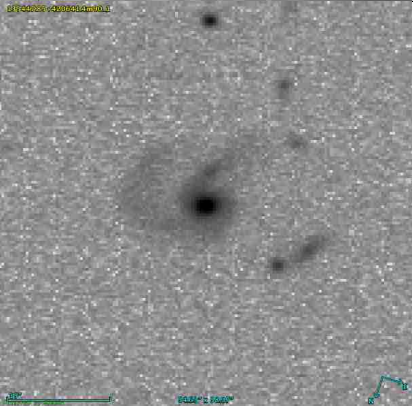
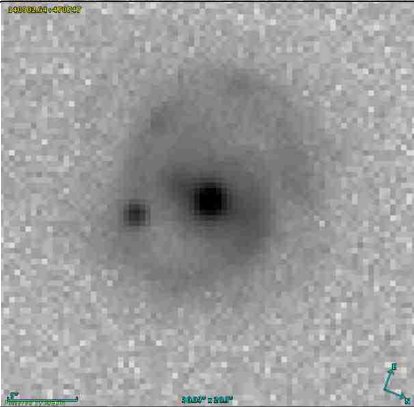

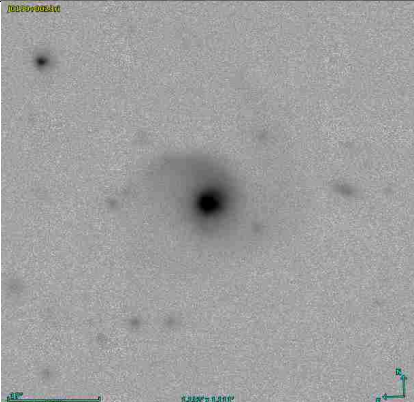
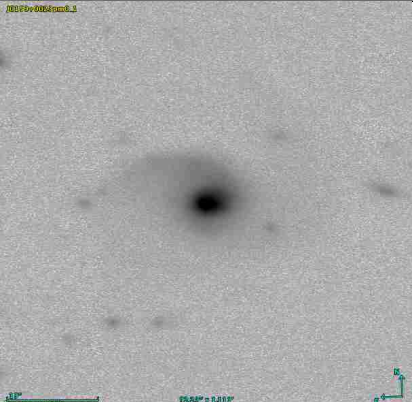
Table 3.3: Galaxy Images

ID	redshift	observed	deprojected
SDSS1	0.0759		
SDSS2	0.2093		
SDSS3	0.041		

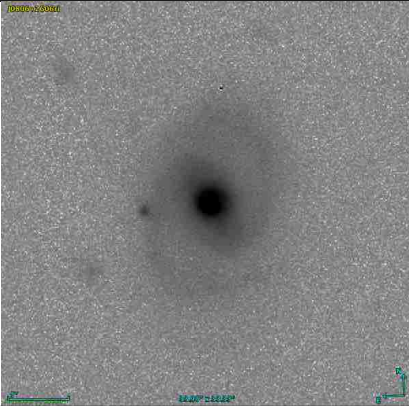
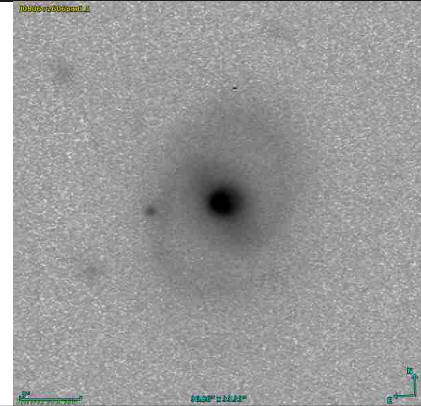
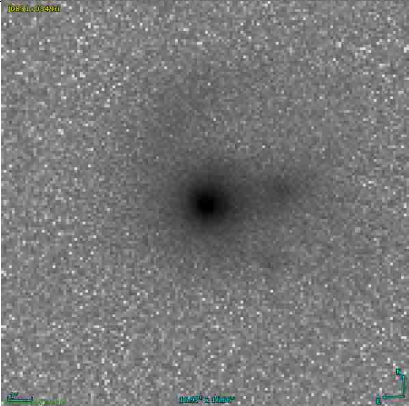
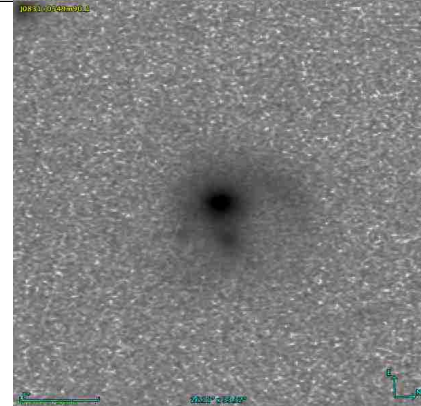
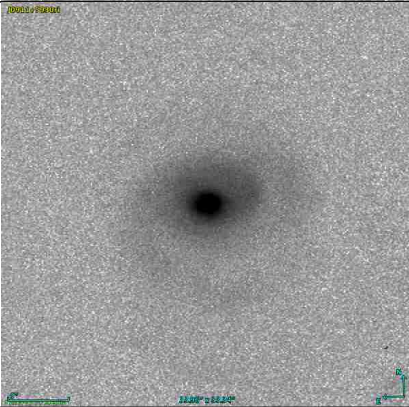
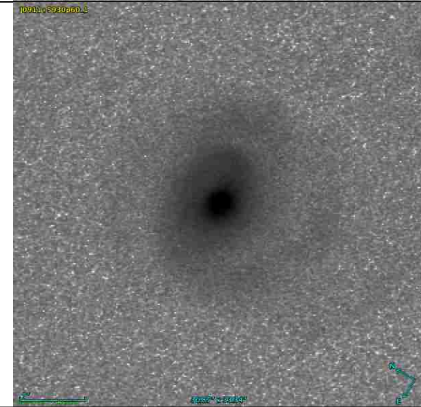
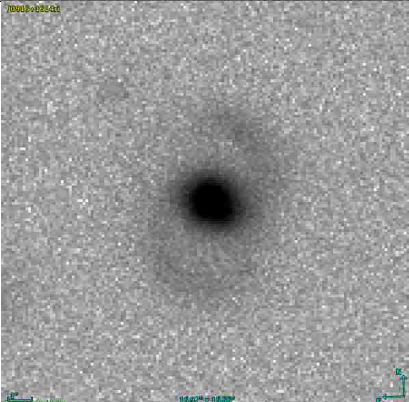
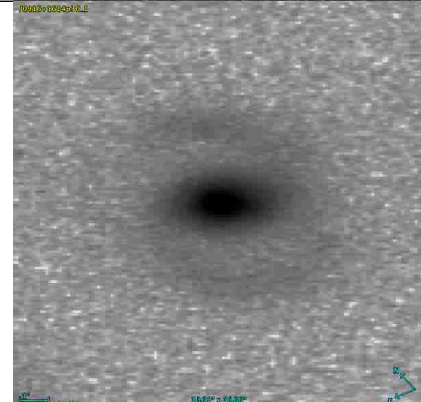
Continuation of Table 3.3

ID	redshift	observed	deprojected
SDSS4	0.2098		
SDSS5	0.2959		
SDSS6	0.1423		
SDSS7	0.2276		

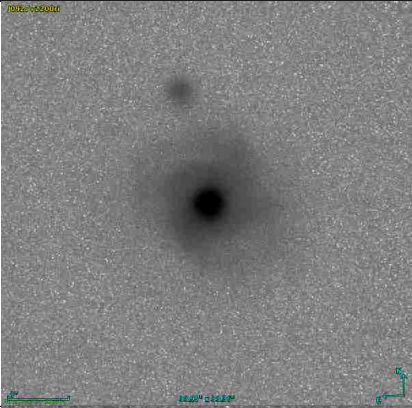
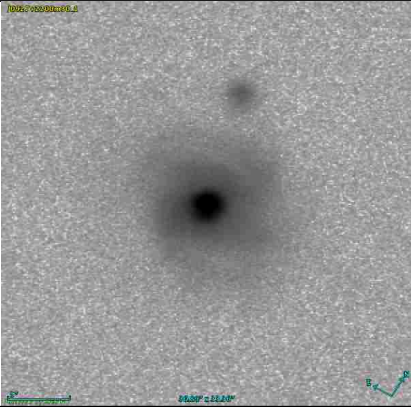
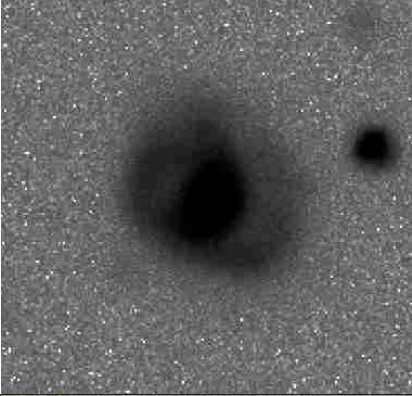
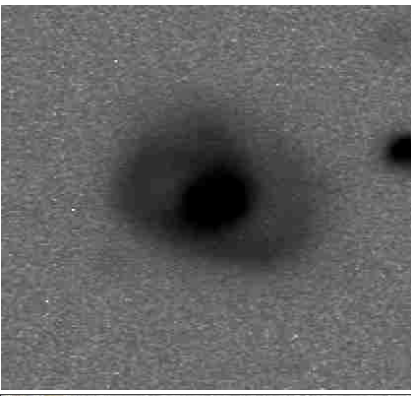
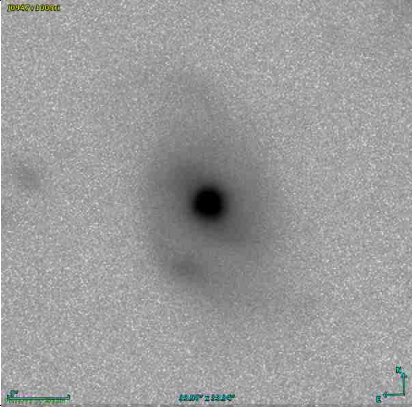
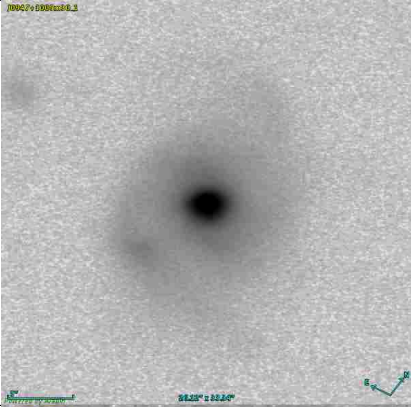
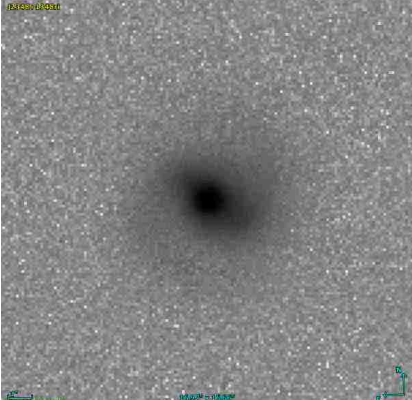
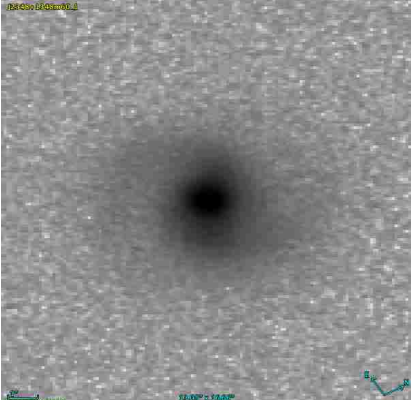
Continuation of Table 3.3

ID	redshift	observed	deprojected
SDSS8	0.1103		
SDSS9	0.2319		
SDSS10	0.1522		
WIYN1	0.1627		

Continuation of Table 3.3

ID	redshift	observed	deprojected
WIYN2	0.136		
WIYN3	0.2287		
WIYN4	0.2289		
WIYN5	0.2984		

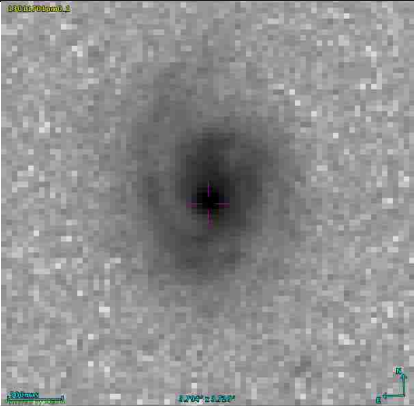
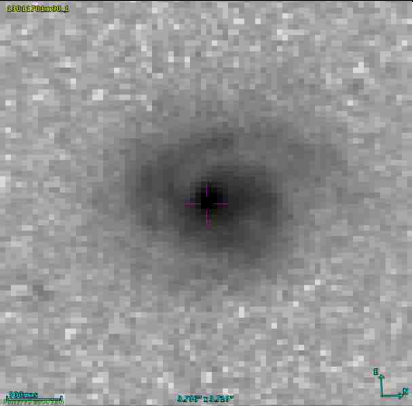
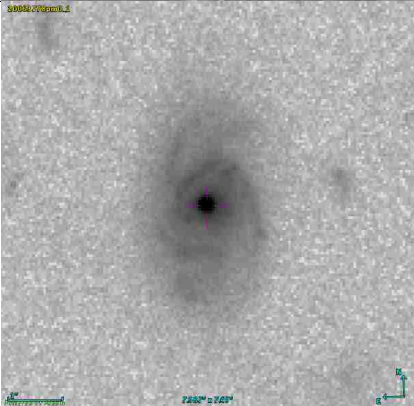
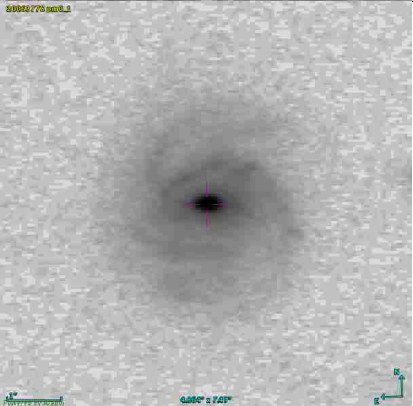
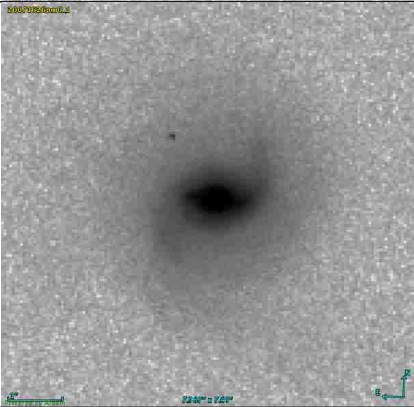
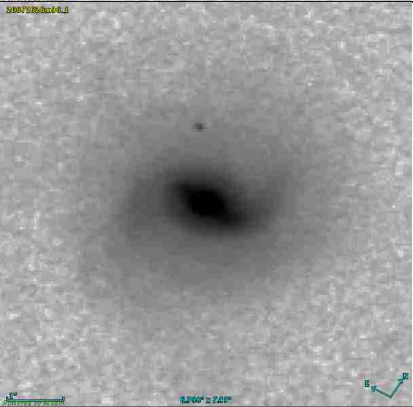
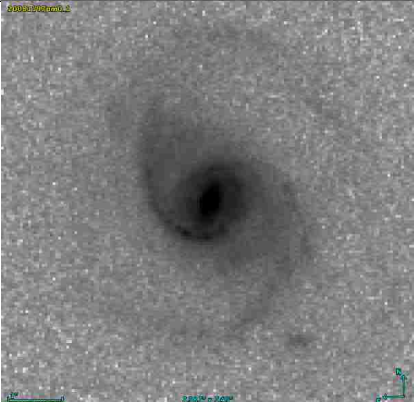
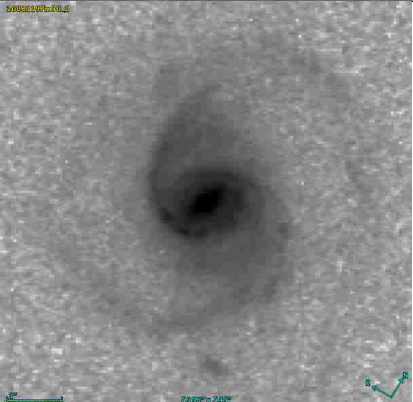
Continuation of Table 3.3

ID	redshift	observed	deprojected
WIYN6	0.1573		
WIYN7	0.1741		
WIYN8	0.1392		
WIYN9	0.2512		

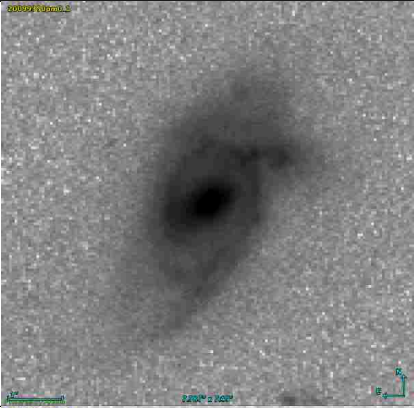
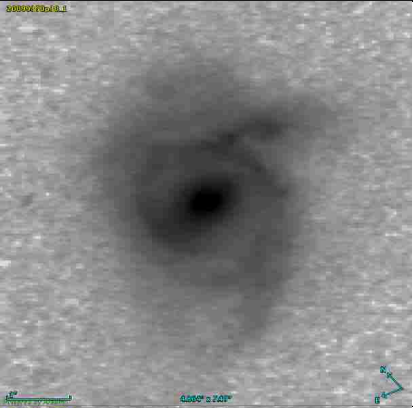
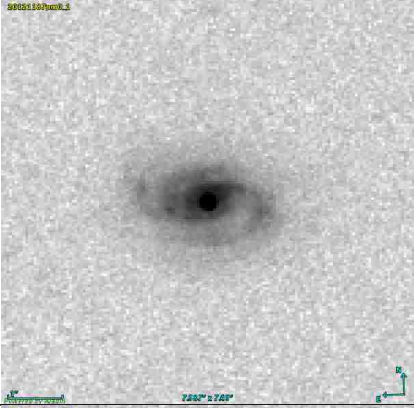
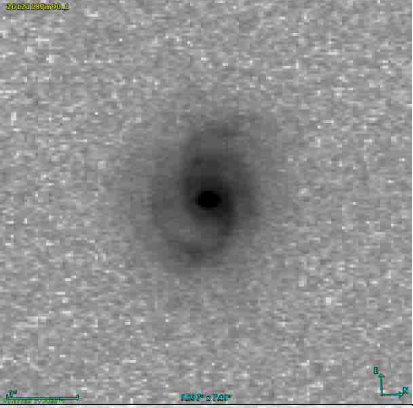
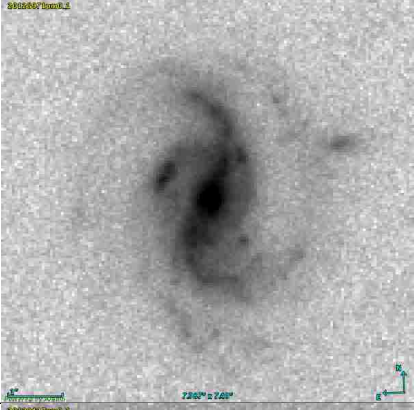
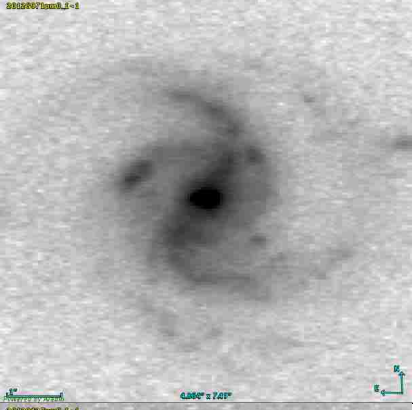
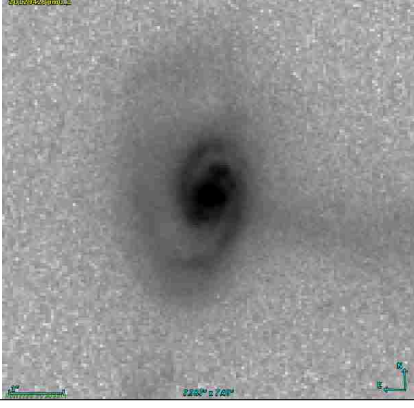
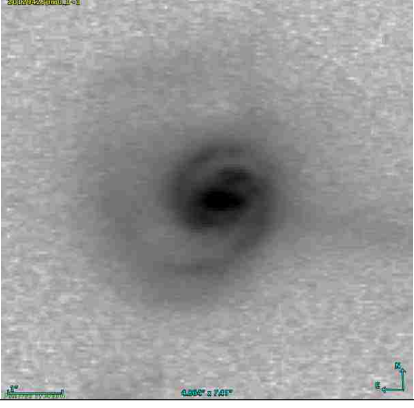
Continuation of Table 3.3

ID	redshift	observed	deprojected
HST1	1.227		
HST2	1.031		
HST3	1.371		
HST4	0.4354		

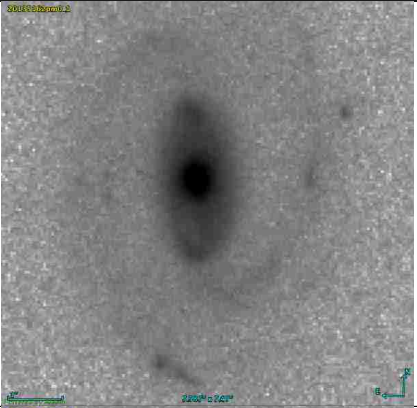
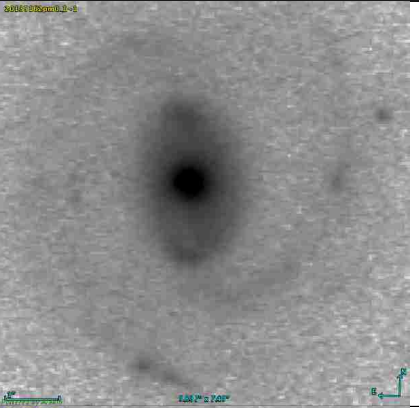
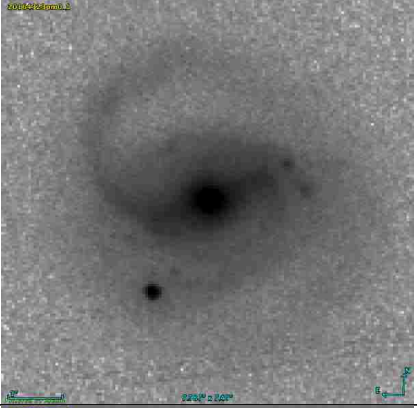
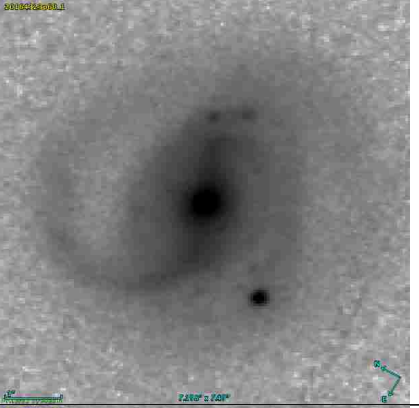
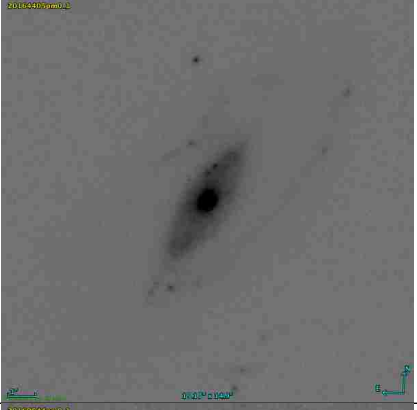
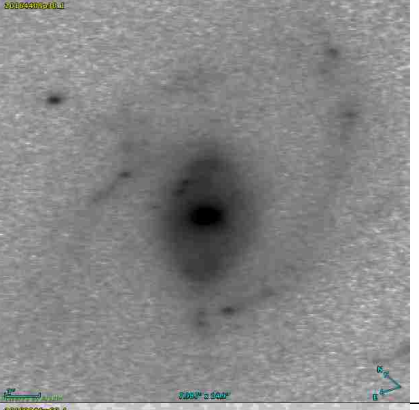


Continuation of Table 3.3

ID	redshift	observed	deprojected
HST5	0.7403		
HST6	0.5524		
HST7	0.3529		
HST8	0.5545		

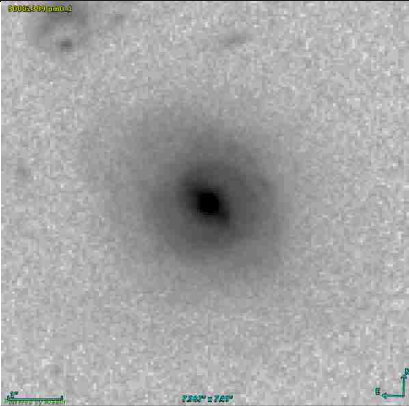
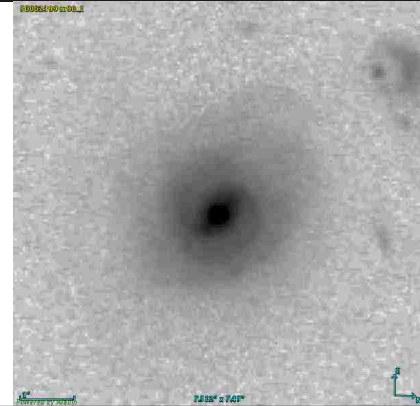
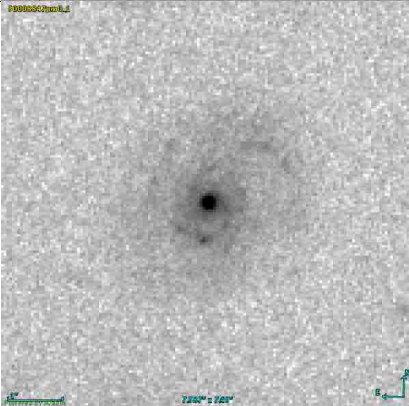
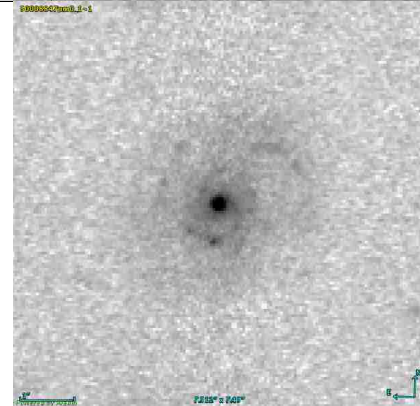
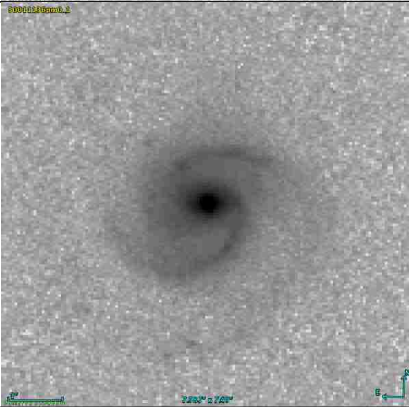
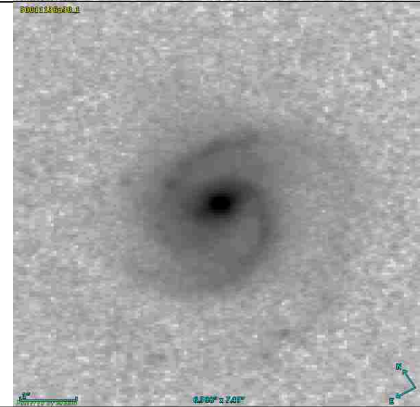
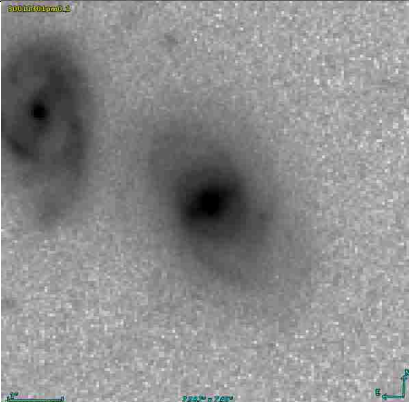
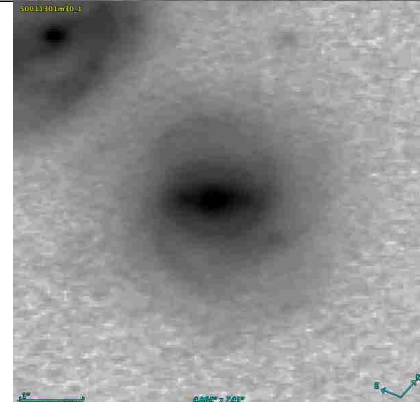
Continuation of Table 3.3

ID	redshift	observed	deprojected
HST9	0.3542		
HST10	0.7277		
HST11	0.3459		
HST12	0.3552		

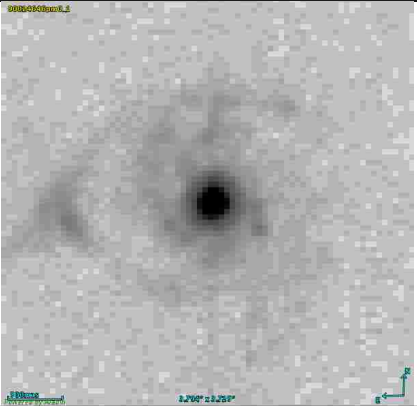
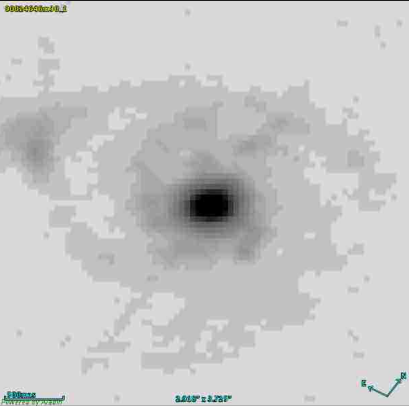
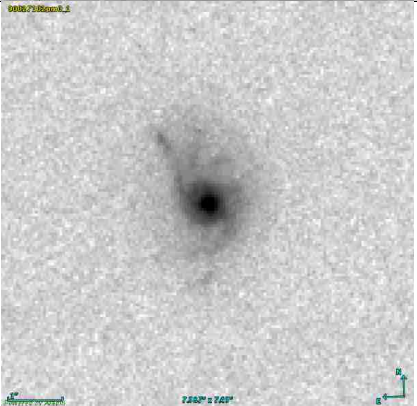
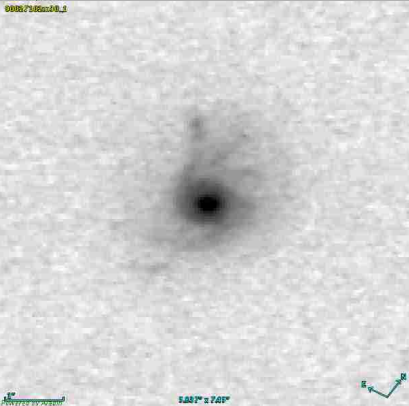
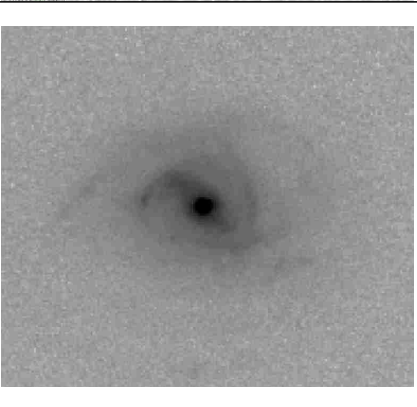
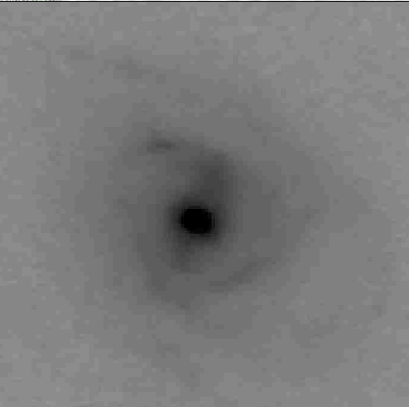
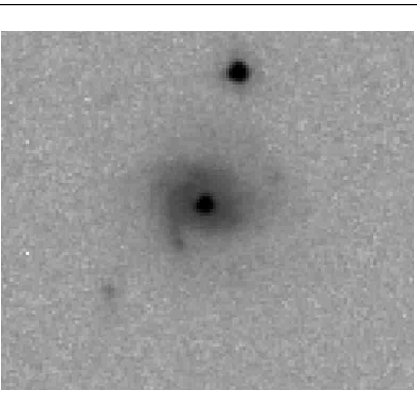
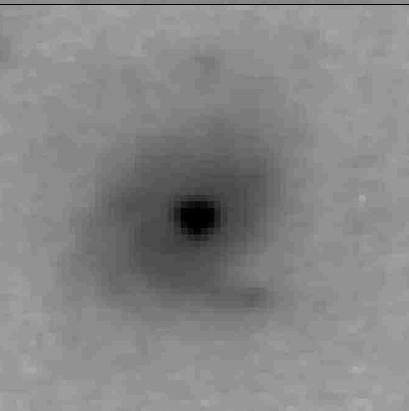
Continuation of Table 3.3

ID	redshift	observed	deprojected
HST13	0.3757		
HST14	0.1962		
HST15	0.2123		
HST16	1.1442		

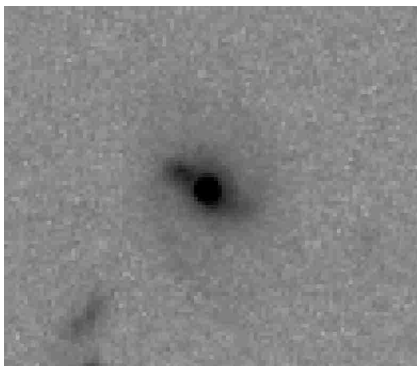

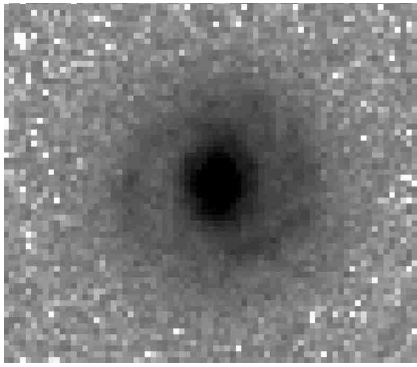
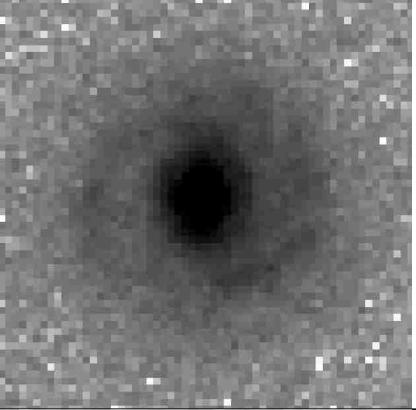
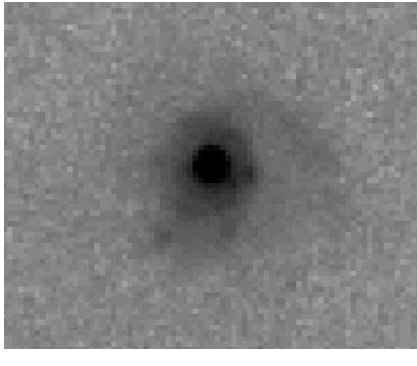
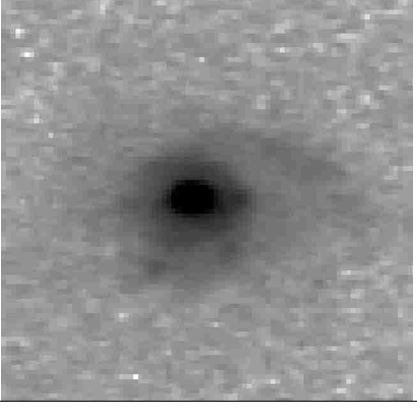
Continuation of Table 3.3

ID	redshift	observed	deprojected
HST17	0.3057		
HST18	1.02		
HST19	0.512		
HST20	0.276		

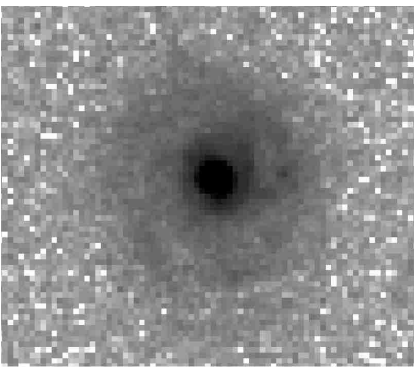
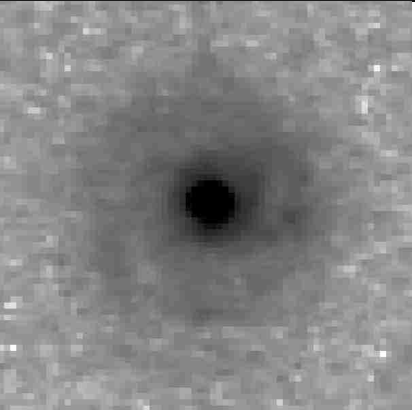

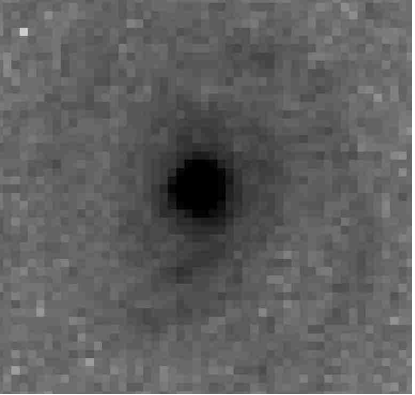
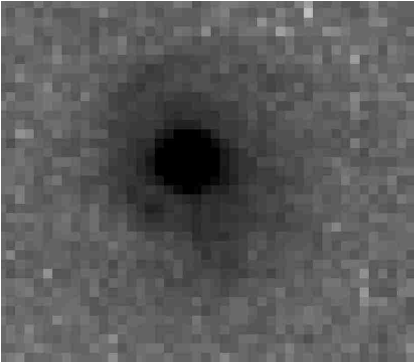
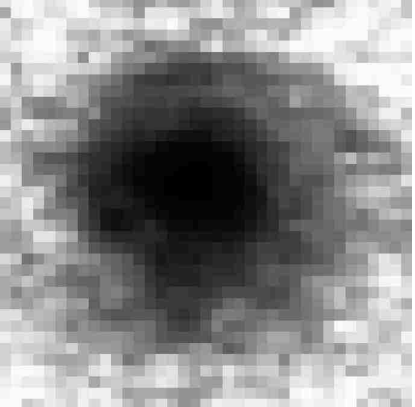
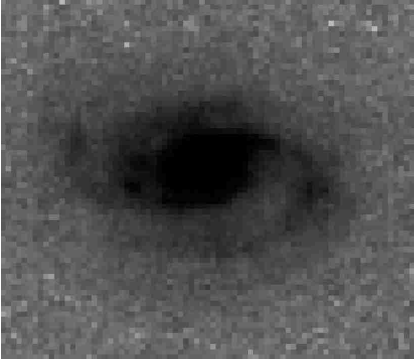
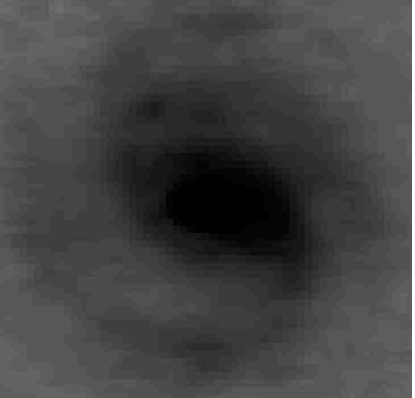
Continuation of Table 3.3

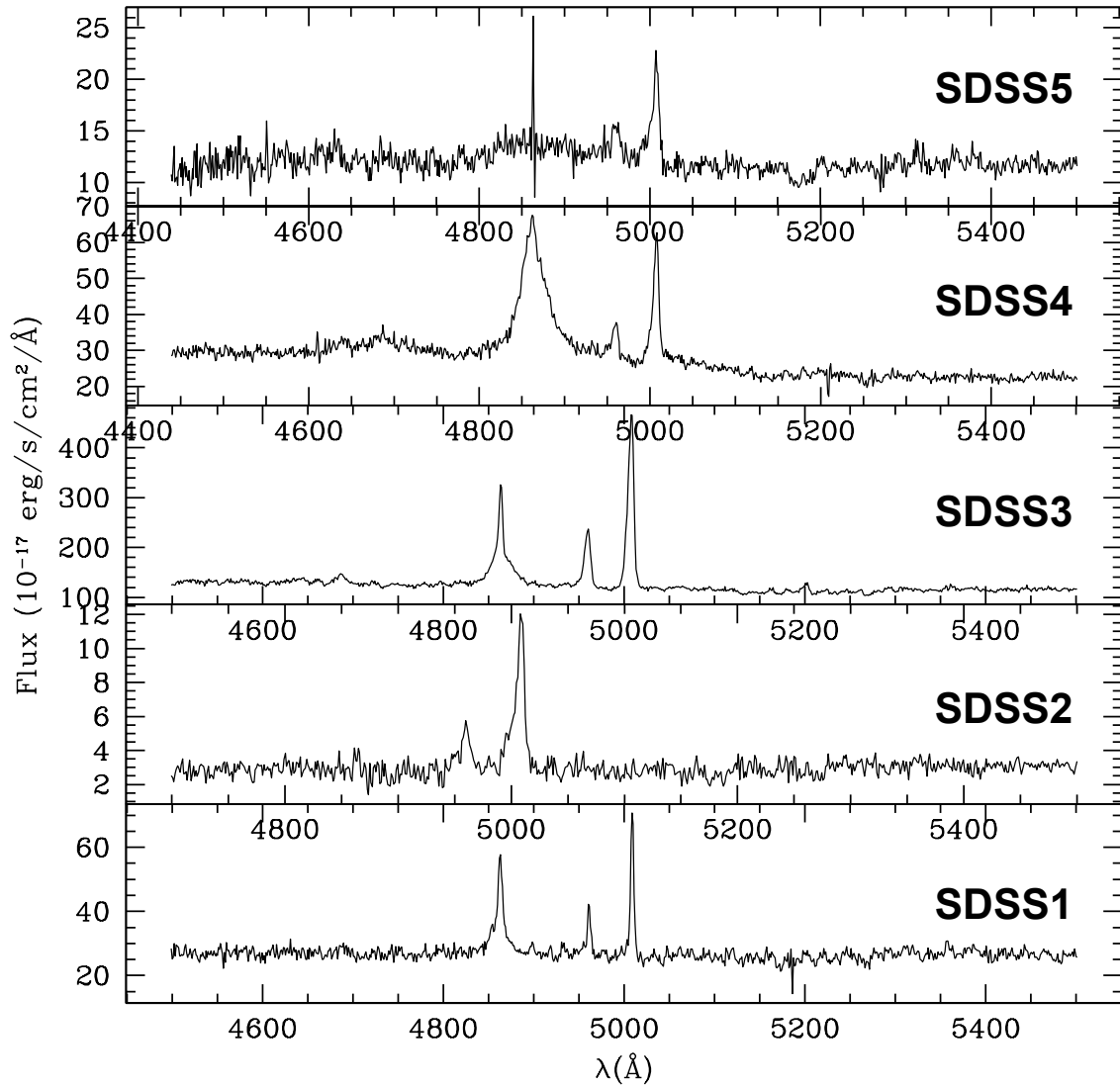
ID	redshift	observed	deprojected
HST21	1.235		
HST22	0.733		
HST23	0.345		
HST24	0.529		

Continuation of Table 3.3

ID	redshift	observed	deprojected
HST25	0.832		
HST26	0.851		
HST27	0.946		

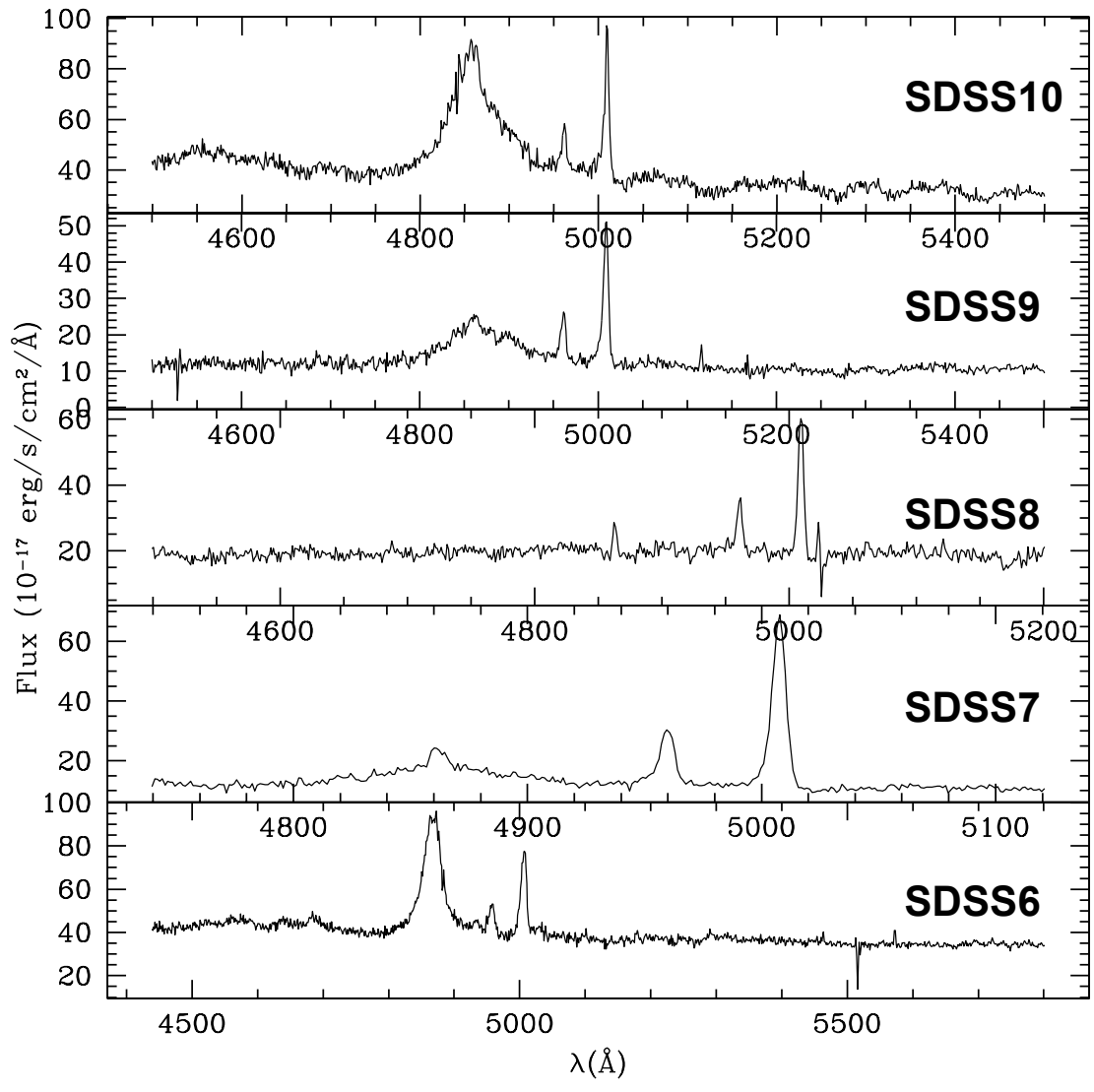
Continuation of Table 3.3

ID	redshift	observed	deprojected
HST28	0.959		
HST29	1.087		
HST30	1.407		
HST31	0.728		



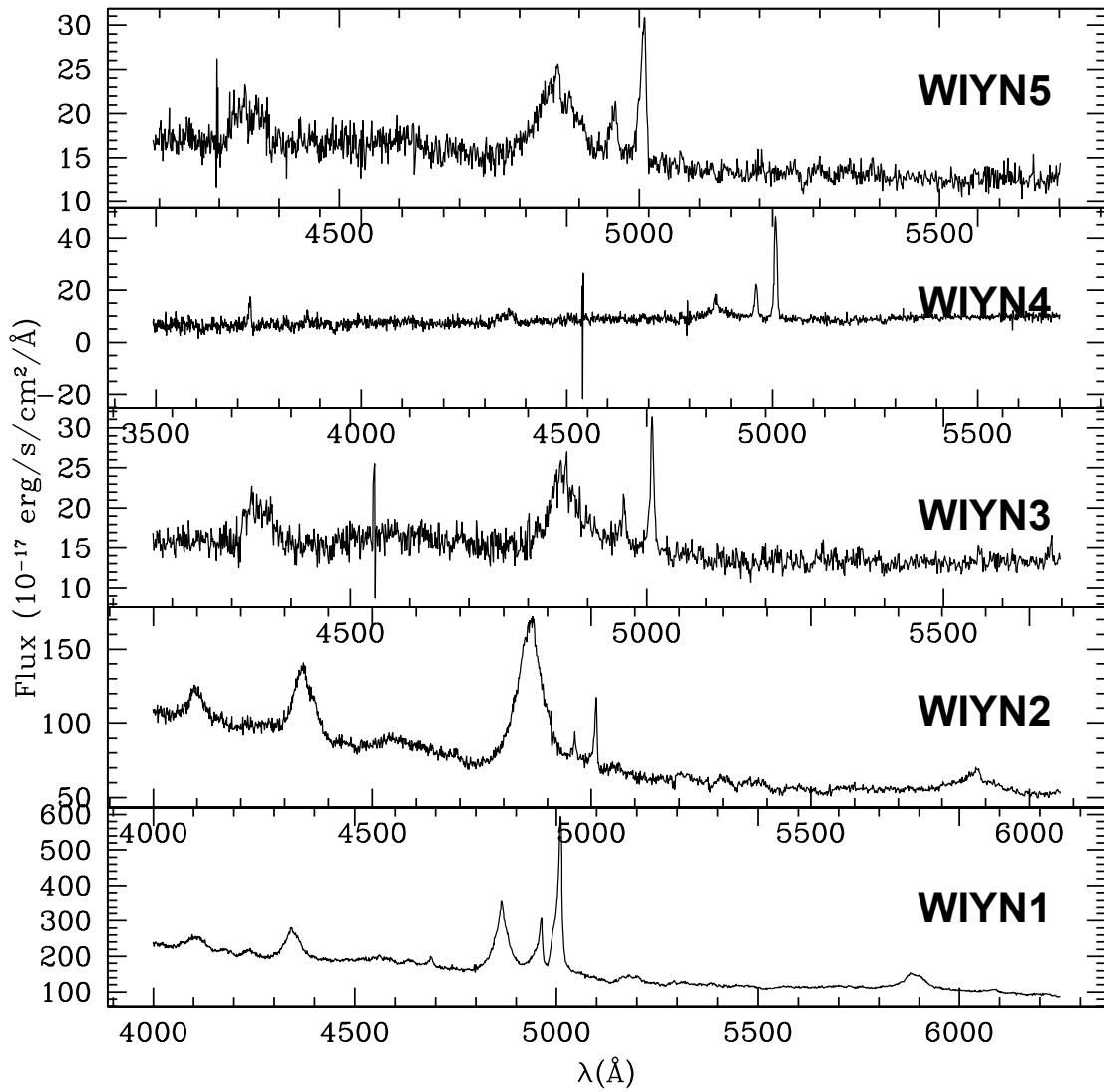
(a)

Figure 3.10: Type 1 AGN spectra



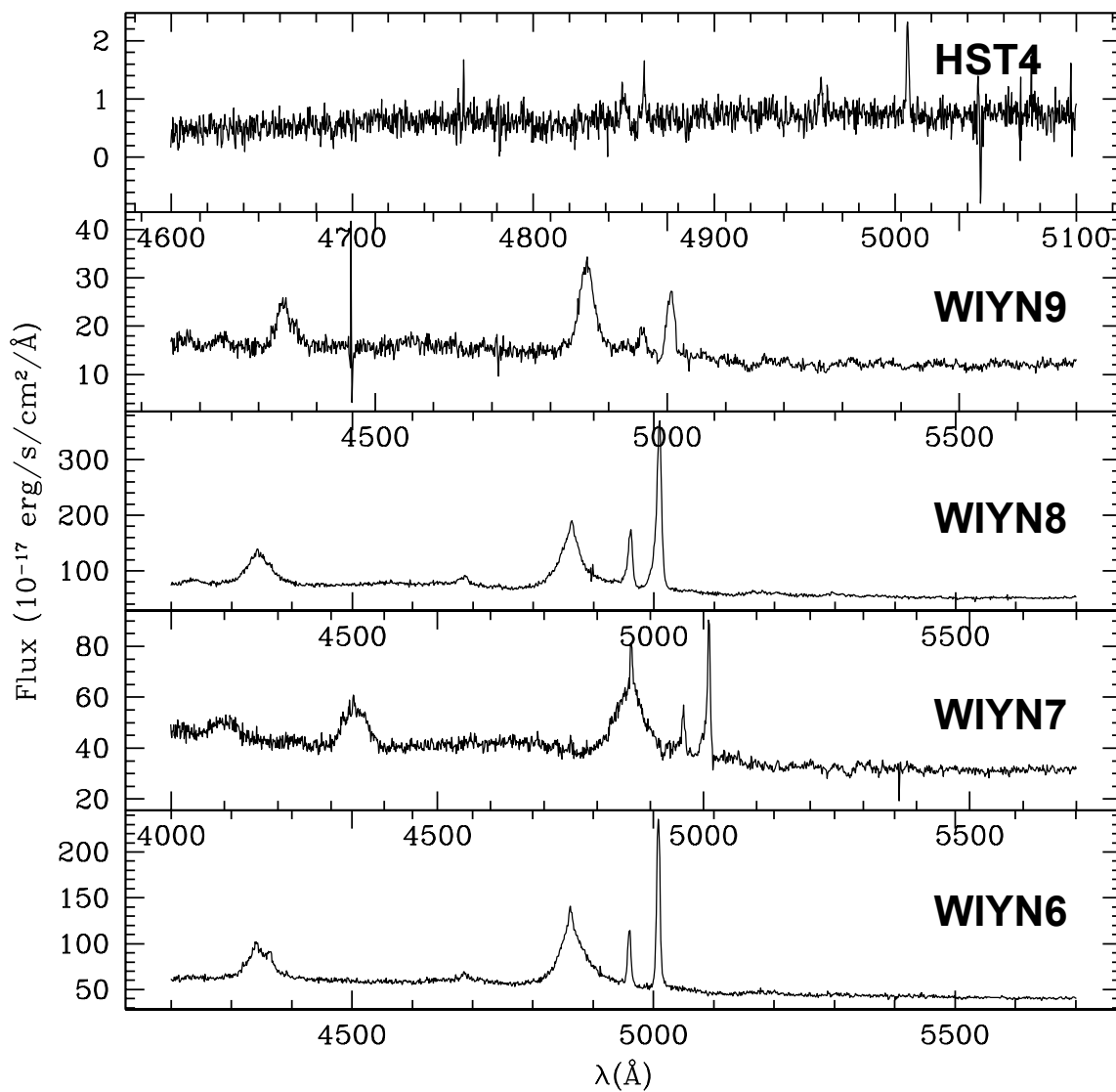
(b)

Figure 3.10: Type 1 AGN spectra (continued)



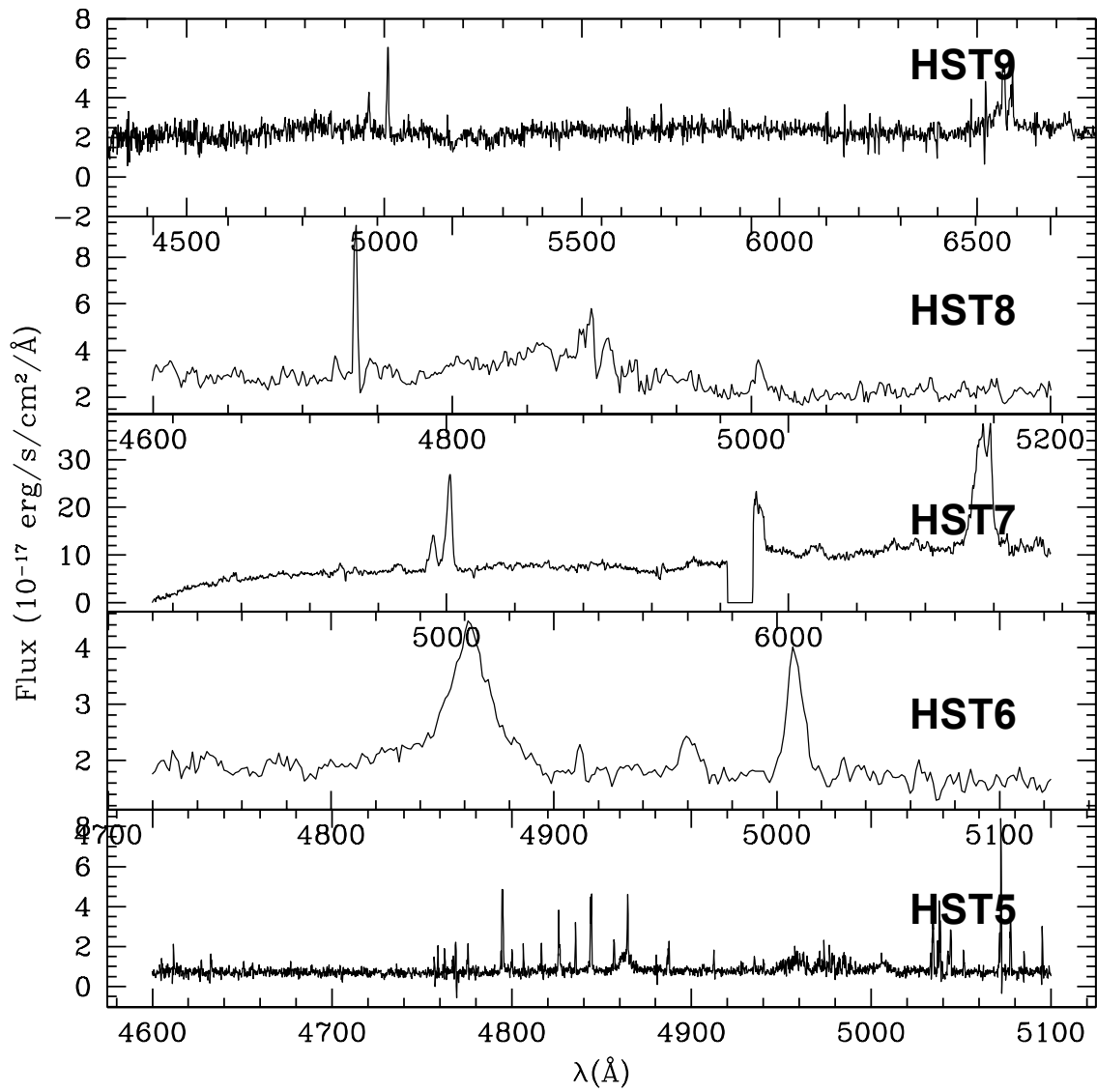
(c)

Figure 3.10: Type 1 AGN spectra (continued)



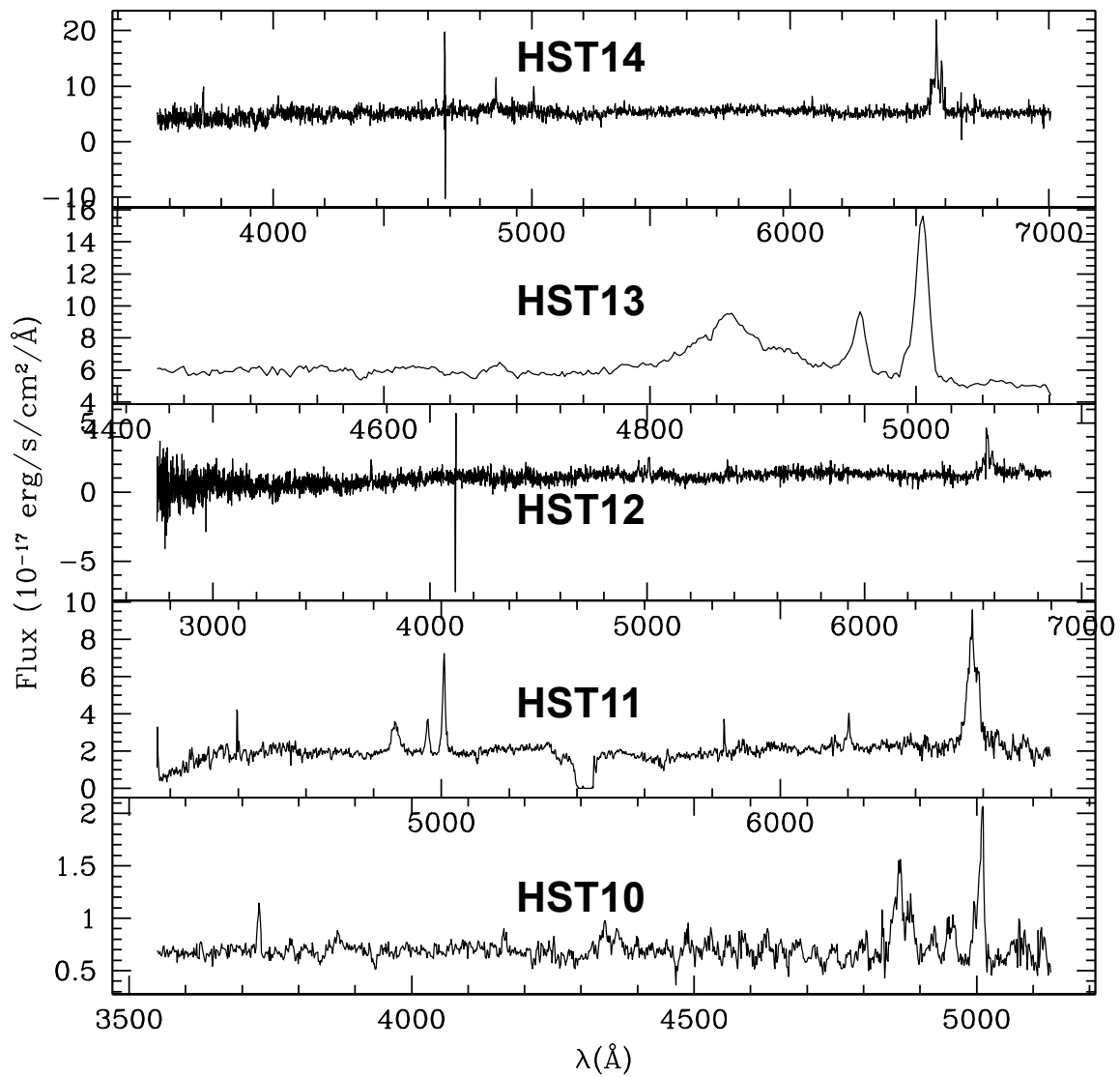
(d)

Figure 3.10: Type 1 AGN spectra (continued)



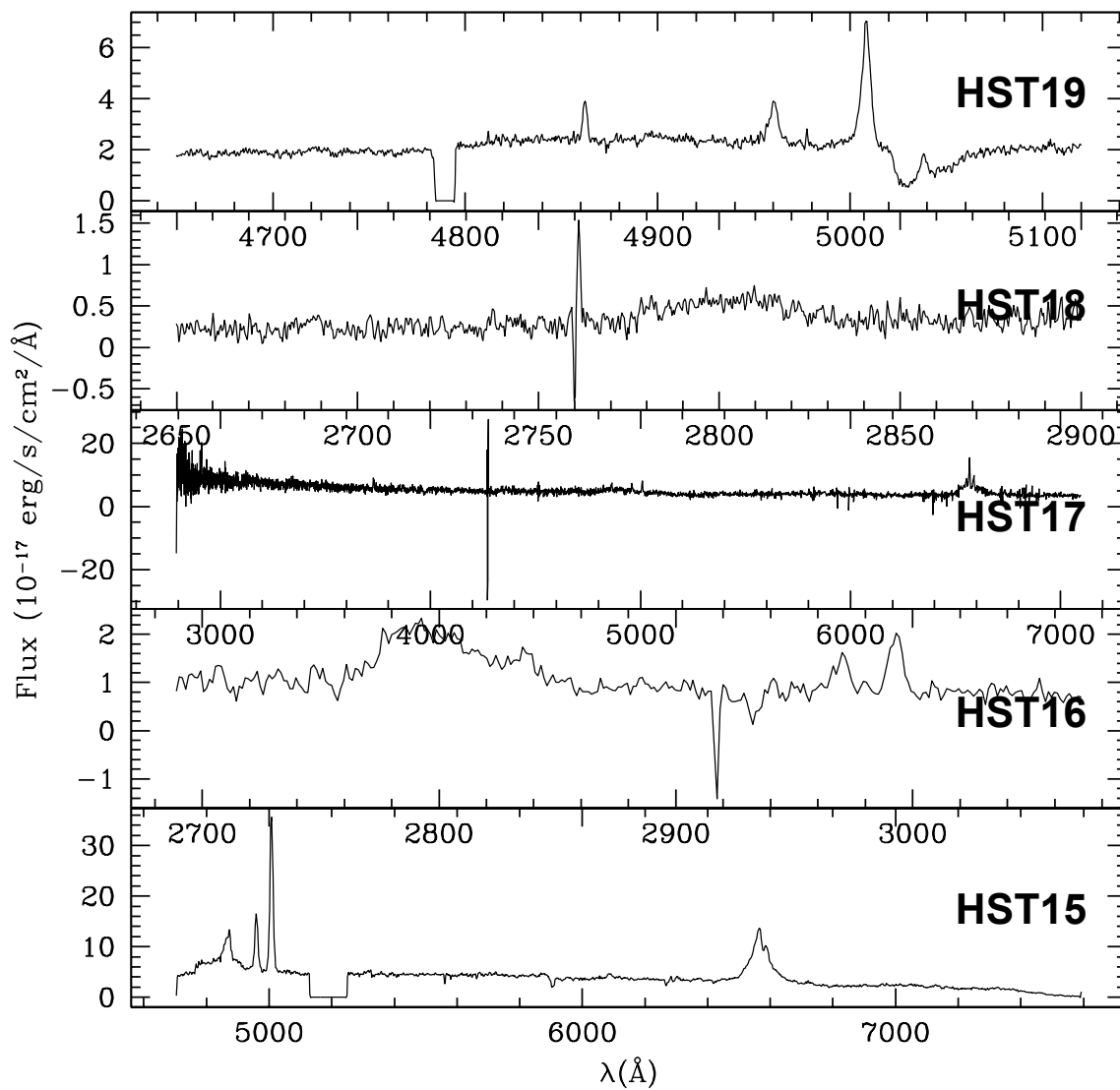
(e)

Figure 3.10: Type 1 AGN spectra (continued)



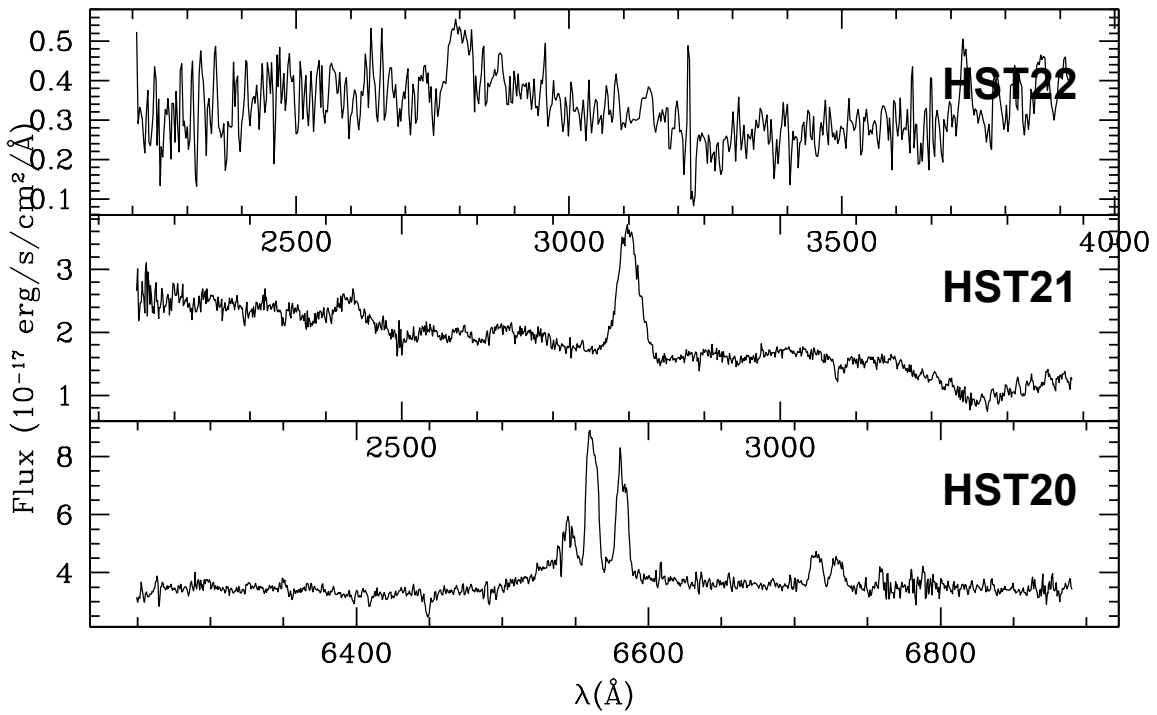
(f)

Figure 3.10: Type 1 AGN spectra (continued)



(g)

Figure 3.10: Type 1 AGN spectra (continued)



(h)

Figure 3.10: Type 1 AGN spectra (continued)

Bibliography

- Abazajian, K. N., Adelman-McCarthy, J. K., Agueros, M. A., et al. 2009, *ApJS*, 182, 543
- Alam, S., Albareti, F. D., Prieto, C. A., et al. 2015, *ApJS*, 219, 27
- Barberà, C., Athanassoula, E., & García-Gómez, C. 2004, *A&A*, 415, 849
- Bentz, M. C., Peterson, B. M., Pogge, R. W., & Vestergaard, M. 2009, *ApJL*, 694, L166
- Berrier, J. C., Davis, B. L., Kenefick, D., et al. 2013, *ApJ*, 769, 17
- Bertin, E., Mellier, Y., Radovich, M., et al. 2002, in *Astronomical Society of the Pacific Conference Series*, Vol. 281, *Astronomical Data Analysis Software and Systems XI*, ed. D. A. Bohlender, D. Durand, & T. H. Handley, 228
- Canalizo, G., Wold, M., Hiner, K. D., et al. 2012, *ApJ*, 760, 38
- Considerere, S., & Athanassoula, E. 1988, *A&AS*, 76, 365
- Davis, B. L., Berrier, J. C., Shields, D. W., et al. 2012, *ApJS*, 199, 20
- Davis, B. L., Berrier, J. C., Johns, L., et al. 2014, *ApJ*, 789, 16
- Davis, B. L., Kenefick, D., Kenefick, J., et al. 2015, *ApJL*, 802, 5
- Dimitrijević, M. S., Popović, L. Č., Kovačević, J., Dačić, M., & Ilić, D. 2007, *MNRAS*, 374, 1181
- Dong, X. Y., & De Robertis, M. M. 2006, *AJ*, 131, 1236
- Elmegreen, D. M., & Elmegreen, B. G. 2014, *ApJ*, 781, 11
- Fabian, A. C. 2012, *ARA&A*, 50, 455
- Ferrarese, L., & Merritt, D. 2000, *ApJ*, 539, L9
- Gebhardt, K., Bender, R., Bower, G., et al. 2000, *ApJL*, 539, L13
- Greene, J. E., & Ho, L. C. 2005a, *ApJ*, 627, 721
- . 2005b, *ApJ*, 630, 122
- Gültekin, K., Richstone, D. O., Gebhardt, K., et al. 2009, *ApJ*, 698, 198
- Häring, N., & Rix, H.-W. 2004, *ApJL*, 604, L89
- Hasan, P. 2007, *Ap&SS*, 312, 63

Hornschemeier, A. E., Brandt, W. N., Garmire, G. P., et al. 2001, *ApJ*, 554, 742

Hughes, J. 2015, Thesis, University of Arkansas.
<http://scholarworks.uark.edu/etd/1400/>

Jones, L. H. 2015, Undergraduate honors thesis, University of Arkansas.
<http://scholarworks.uark.edu/physuht/5/>

King, A. 2003, *ApJL*, 596, L27

Kormendy, J., & Ho, L. C. 2013, *ARA&A*, 51, 511

Kormendy, J., & Richstone, D. 1995, *ARA&A*, 33, 581

Lilly, S. J., Le Fèvre, O., Renzini, A., et al. 2007, *ApJS*, 172, 70

Lin, C. C., & Shu, F. H. 1966, *PNAS*, 55, 229

Lin, D., Webb, N. A., & Barret, D. 2012, *ApJ*, 756, 27

Lusso, E., Comastri, A., Vignali, C., et al. 2010, *A&A*, 512, A34

Magorrian, J., Tremaine, S., Richstone, D., et al. 1998, *AJ*, 115, 2285

Matthews, D. J., Newman, J. A., Coil, A. L., Cooper, M. C., & Gwyn, S. D. J. 2013, *ApJS*, 204, 21

McLure, R. J., & Dunlop, J. S. 2001, *MNRAS*, 327, 199

McLure, R. J., & Jarvis, M. J. 2002, *MNRAS*, 337, 109

Pour-Imani, H., Kenefick, D., Kenefick, J., et al. 2016, *ApJL*, 827, L2

Prescott, M. K. M., Impey, C. D., Cool, R. J., & Scoville, N. Z. 2006, *ApJ*, 644, 100

Robertson, B., Hernquist, L., Cox, T. J., et al. 2006, *ApJ*, 641, 90

Salviander, S., & Shields, G. A. 2013, *ApJ*, 764, 7

Schlaflly, E. F., & Finkbeiner, D. P. 2011, *ApJ*, 737, 13

Shen, Y., Richards, G. T., Strauss, M. A., et al. 2011, *ApJS*, 194, 45

Shields, D. W., Schilling, A. B., Kenefick, D., & Kenefick, J. 2017, submitted to *ApJ*

Shields, G. A., Gebhardt, K., Salviander, S., et al. 2003, *ApJ*, 583, 124

Shu, F. H. 1984, in *IAU Colloq. 75: Planetary Rings*, ed. R. Greenberg & A. Brahic,

- Shu, F. H. 2016, *ARA&A*, 54, 667
- Silk, J., & Rees, M. J. 1998, *A&A*, 331, L1
- Silverman, J. D., Mainieri, V., Salvato, M., et al. 2010, *ApJS*, 191, 124
- Szokoly, G. P., Bergeron, J., Hasinger, G., et al. 2004, *ApJS*, 155, 271
- Treu, T., Malkan, M. A., & Blandford, R. D. 2004, *ApJL*, 615, L97
- Trouille, L., Barger, A. J., Cowie, L. L., Yang, Y., & Mushotzky, R. F. 2008, *ApJS*, 179, 1
- Trump, J. R., Impey, C. D., McCarthy, P. J., et al. 2007, *ApJS*, 172, 383
- Trump, J. R., Impey, C. D., Elvis, M., et al. 2009, *ApJ*, 696, 1195
- Tsuzuki, Y., Kawara, K., Yoshii, Y., et al. 2006, *ApJ*, 650, 57
- Véron-Cetty, M. P., Joly, M., & Véron, P. 2004, *A&A*, 417, 515
- Vestergaard, M., & Peterson, B. M. 2006, *ApJ*, 641, 689
- Wandel, A. 2002, *ApJ*, 565, 762
- Wang, T., & Lu, Y. 2001, *A&A*, 377, 52
- Willett, K. W., Galloway, M. A., Bamford, S. P., et al. 2017, *MNRAS*, 464, 4176
- Wirth, G. D., Willmer, C. N. A., Amico, P., et al. 2004, *AJ*, 127, 3121
- Woo, J.-H., Treu, T., Barth, A. J., et al. 2010, *ApJ*, 716, 269

Chapter 4

Conclusion

In this dissertation, I examined the optical-UV energy emitted from active galactic nuclei (AGN) using photometric data to construct spectral energy distributions (SEDs). Emission in the optical-UV is most likely a combination of thermal and synchrotron energy from the accretion disk and has been observed to follow a power-law $f_\nu \propto \nu^\alpha$. Due to the challenges of studying objects at a large range of redshifts, the spectral index, α , has traditionally been approximated from composite spectral energy distributions. In Chapter 2, I present the optical-UV spectral index measurements, α_o , of 96 high redshift AGN. We found α_o to vary greatly between objects and on average α_o does not agree with the $\alpha = -0.5$ assumption. Our measurements also suggest evolution of α_o with redshift – the SED is steeper at higher redshifts on average. Misunderstanding of the SED or misuse of an average spectral index impacts how accurately we are able to measure the luminosity of individual objects. We calculated absolute i -band magnitude, M_i , using the previously assumed $\alpha = -0.5$ and compared it to M_i calculated from α_o . We found that the assumption of $\alpha = -0.5$ gave systematically brighter luminosities. This difference is especially stark for the $\langle z \rangle = 4.07$ AGN. With the release of several all-sky-survey data sets, it is possible to use the techniques described in Chapter 2 to measure α_o for more AGN. The corrected α_o for individual objects would help to further studies of absolute magnitude, bolometric luminosity, as well as quasar luminosity functions.

The amount of energy emitted by AGN suggests that there could be interaction with host galaxies. In fact AGN-feedback, the exchange of material and energy between AGN

and galaxies, has been studied through the co-evolution of black holes and larger galaxy properties. These studies focus mainly on elliptical galaxies. However Berrier et al. (2013) presented the $M_{BH}-\phi$ relation for spiral galaxies. In Chapter 3 we found a sample of spiral galaxies that host Type 1 AGN in order to measure M_{BH} beyond the local epoch.

Emission lines in the optical-UV spectra of Type 1 AGN are the result of reprocessed energy from the accretion disk that ionizes gas orbiting the black hole. We used the width and luminosity of the emission lines to measure black hole mass and we measured pitch angle of the spiral arms using a 2DFFT algorithm. We showed that the $M_{BH}-\phi$ relation is not stable at higher redshifts — the slope of the $M_{BH}-\phi$ relation steepens as redshift increases. The $M_{BH}-\phi$ relation is a two-dimensional projection of the fundamental plane relation between bulge mass, pitch angle, and the density of neutral hydrogen in the disk. This fundamental plane relation was used to transform the $M_{BH}-\phi$ relation into a function of disk density vs. bulge mass for our sample. We find more high-density disks in local epochs. We expect disks to be less dense in the past especially at $z \sim 1.5 - 1.9$ where spiral arms are beginning to form. Spiral arm formation happens as ‘puffy’ disks settle into a smaller volume until density waves are able to dominate. AGN also contribute to the lowering of disk density - AGN winds heat disks and in some cases can expel gas out of the disks of galaxies. The peak in AGN activity was at $z \sim 2.0 - 3.0$ so we expect that disk density, on average, will increase at lower redshifts.

In the future we will extend the study of disk density in spiral galaxies by taking advantage of data from a new SDSS project, Mapping Nearby Galaxies at APO (MaNGA, Bundy et al., 2015). In Chapter 3, evidence for the fundamental plane of disk galaxies was presented from Davis et al. (2015). The measurements in Davis et al. (2015) were taken

from the Disk Mass Survey (Martinsson et al., 2013) who used integral field spectroscopy to measure stellar velocity dispersions and gas velocities – proxies for bulge mass and disk density. MaNGA will take integral field spectroscopy across the disks of spiral galaxies out to redshifts $z \sim 0.03$.

Bibliography

Berrier, J. C., Davis, B. L., Kennefick, D., et al. 2013, *ApJ*, 769, 17

Bundy, K., Bershady, M. A., Law, D. R., et al. 2015, *ApJ*, 798, 7

Davis, B. L., Kennefick, D., Kennefick, J., et al. 2015, *ApJL*, 802, 5

Martinsson, T. P. K., Verheijen, M. A. W., Westfall, K. B., et al. 2013, *A&A*, 557, A130

Appendix A

Image Processing

In this section I describe the steps used to process images in order to find infrared J, H, and K apparent magnitudes of the quasars in Chapter 2. Images were taken at Kitt Peak National Observatory using the 2.1 meter telescope with the Simultaneous Quad Infrared Imaging Device (SQIID) during 2005 November 4–10. The quasars in this study were observed using a dithering program (see Figure A.5) where each object was imaged for 120 seconds in each of 5 offset positions.

A.1 Image Reduction

Image reduction accounts for noise from two main sources: the detector itself and the background or sky. The process can be understood from the simple equation:

$$\text{reduced image} = \frac{\text{raw image} - (\text{sky \& dark frames})}{\text{flat frame}}$$

All raw images were reduced by subtracting off noise from the detector (dark frame) and noise from the sky (sky frame), then normalizing the image (with flat frame) to take into account the pixel to pixel variation of the detector. These steps were carried out using the IRAF `upsqiid`¹ package. Examples and descriptions of each of these frames are shown below.

SQIID dark frames are stable over a night but are time dependent. Each night dark exposures were taken for each JHK filter at the same exposure time as object images. Dark frames were created with `usqdark` – Figure A.1.

¹<https://www.noao.edu/kpno/sqiid/upsqiidpkg.html>

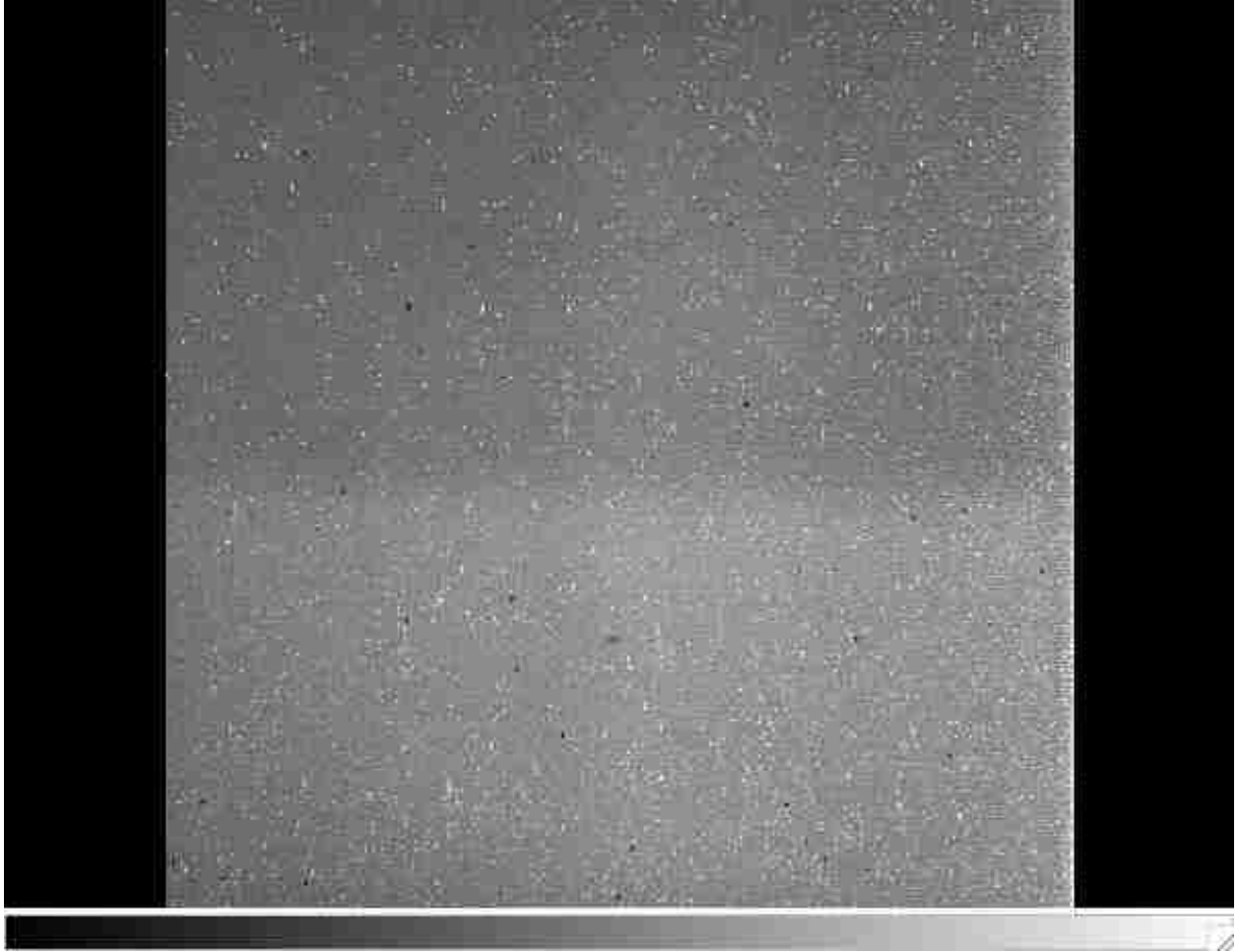


Figure A.1: **Dark Frames** — Turning on the detectors but not exposing them to light produces dark frames. Dark frames reveal the noise of the individual pixels.

The sky background in the infrared is very sensitive to temperature, humidity, moonlight, and light reflected off of clouds. Sky exposures are not stable over a night. We found the median pixel values from six image frames taken closest in time to the frame being processed in order to create sky frames with `movproc` – Figure A.2. The dithering pattern allowed for the averaging out of any objects in the frames.

The flat field or pixel-to-pixel sensitivity is stable over a night for SQUID. We used object frames taken throughout the night and found the median pixel value to create flat frames using `usqflat` – Figure A.3. A dithering program was used for imaging – five

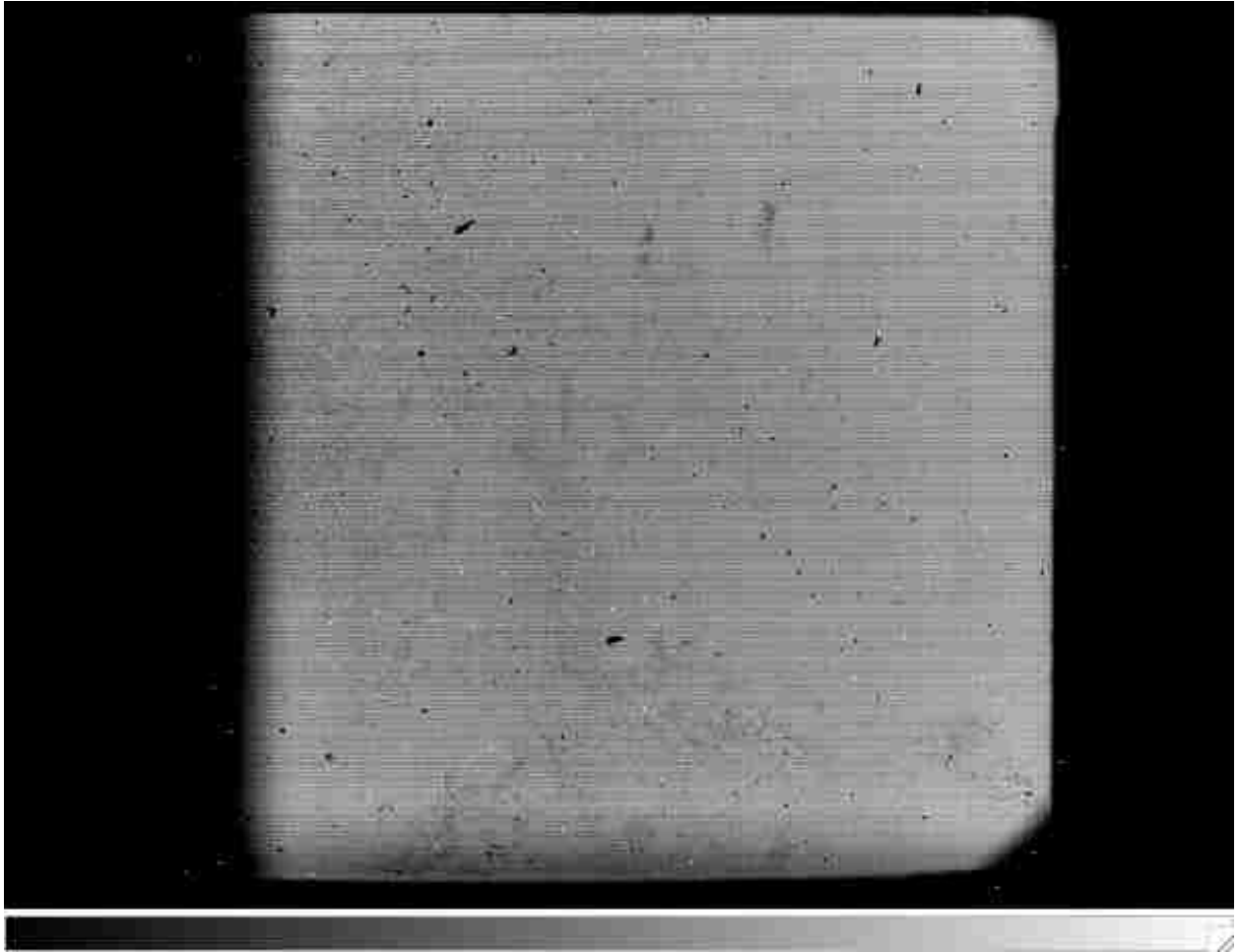


Figure A.2: **Sky Frames** — Sky frames, ideally, should be images taken of the sky with no objects (such as stars) present in the field. In this case we averaged several frames that had objects in them to use as sky frames so long as the objects present were offset enough between frames to not survive in the averaging.

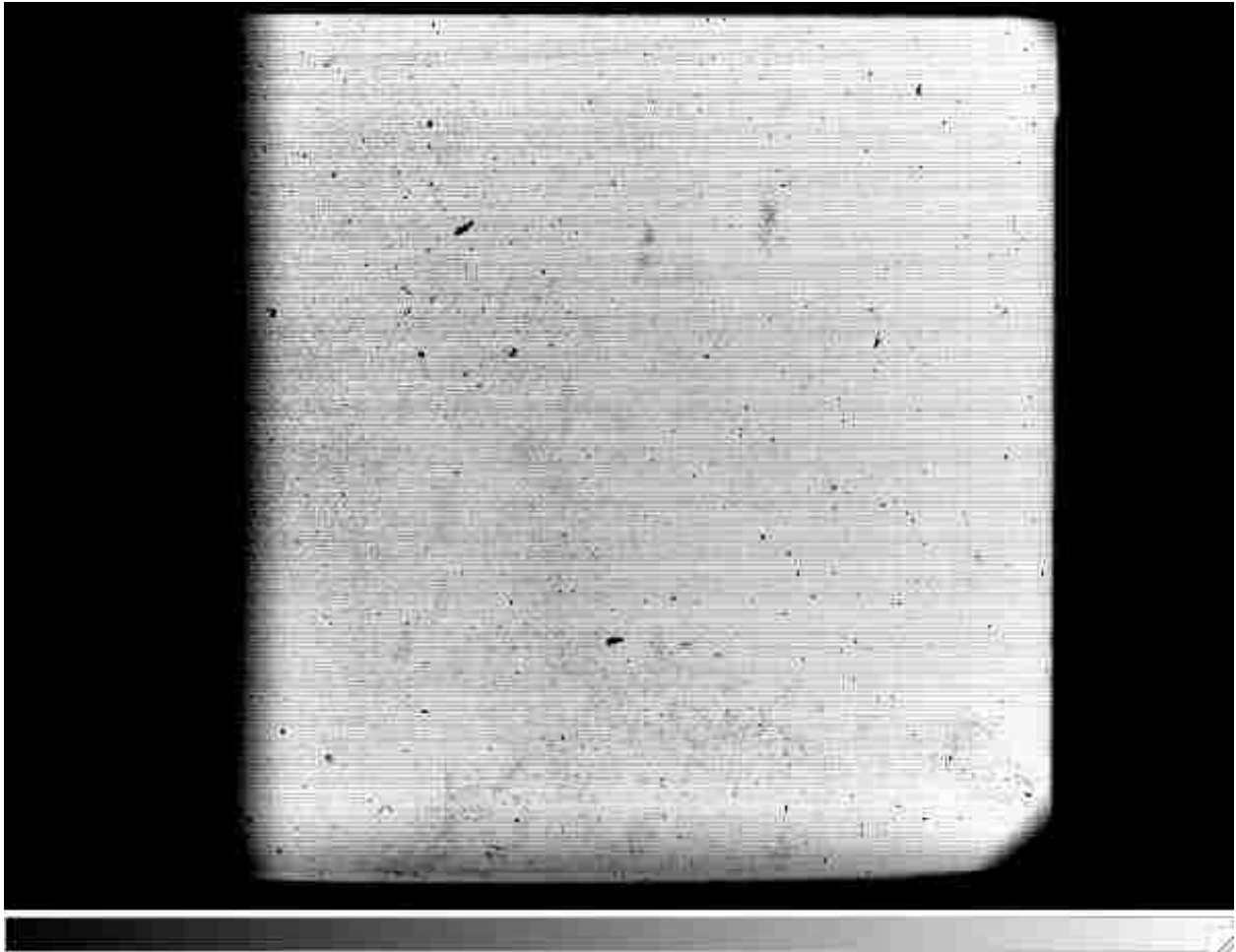


Figure A.3: **Flat Frames** — Flat frames, again ideally, are obtained by exposing the detector to a source of light with uniform, known energy. Flat frames reveal the gain ratio of photons hitting the detector to the number actually recorded for each pixel. As with the sky frames, we used object frames to make the flats by dividing each pixel in a frame by the median pixel value for that frame. (An actual flat frame is the average of many flats.)

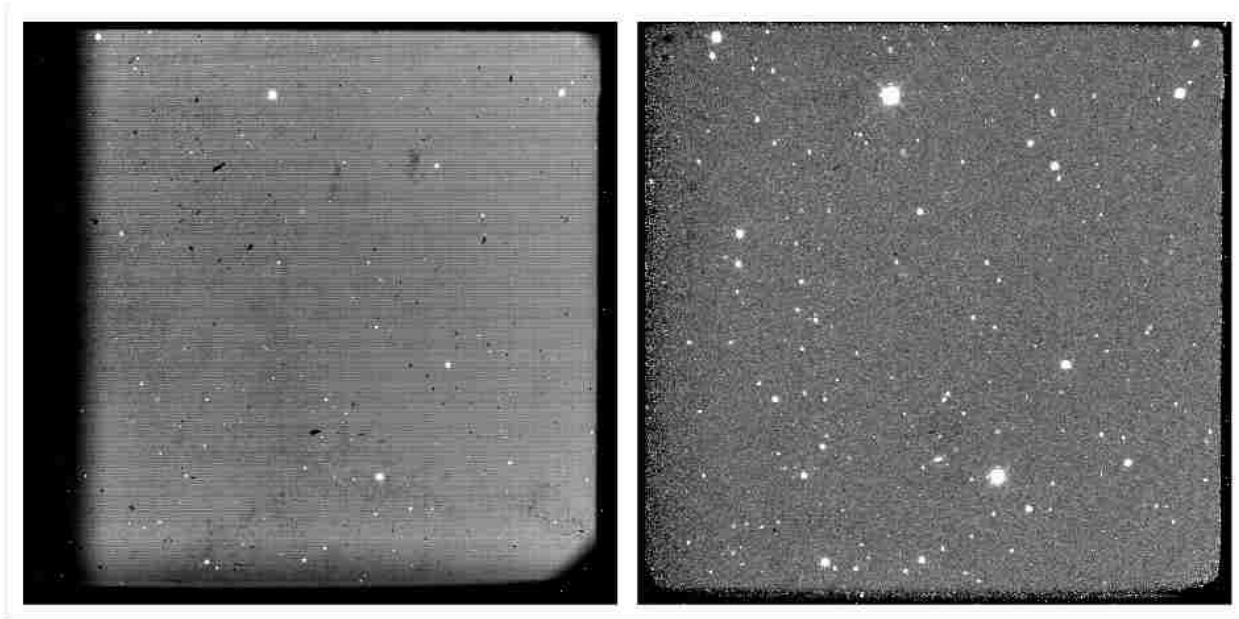


Figure A.4: **Image Reduction** — example of a raw frame (left) and the same frame after image reduction (right).

separate, spatially offset exposures were taken for each quasar in each JHK filter – in order to boost signal and decrease noise. Thus 15 raw exposures for each of the 96 quasars (a total of 1,440) were processed using the techniques described above. Figure A.4 shows an example of a single frame before and after the image reduction process. Finally, the dithered frames were combined by first identifying three to five point sources common in each of the five exposures and registering them with `xyget`. The five exposures were combined using the registered point sources with `nircombine` to get an average value for each pixel. See Figure A.5 for an example.

A.2 Astrometry

In order to find the plate solution for each of the 96 reduced and combined images, I used the software package `WCSTools` (Mink, 1999). The task `imwcs` reads right ascension and

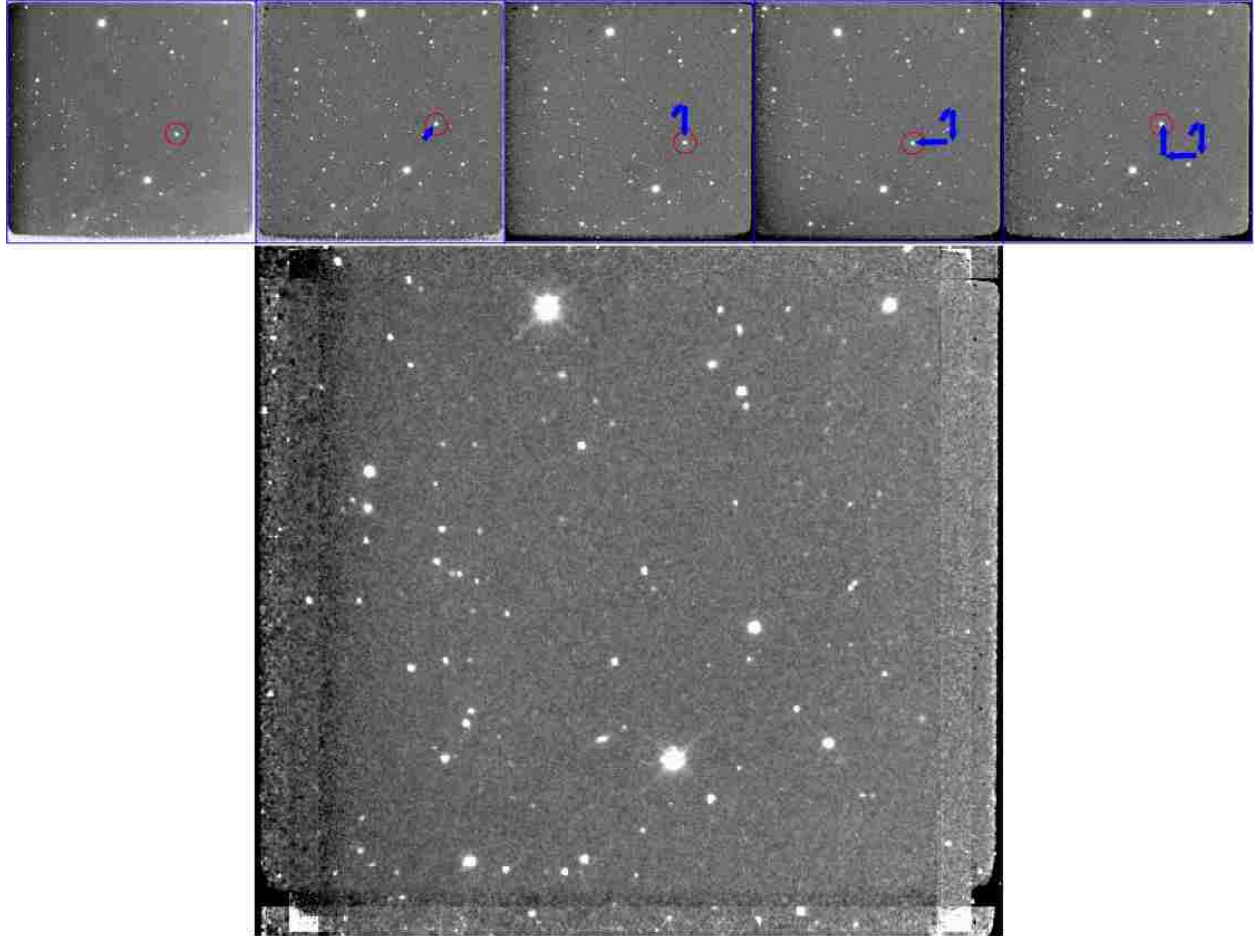


Figure A.5: **Combination of Dithered frames**

declination keywords in a FITS image file as a starting point then matches point sources in the image to a catalog of objects with known coordinates. The following command

```
$ imwcs -wc tmc -p 0.68 {image}.fits
```

matches point sources in `{image}.fits` to objects in the 2MASS Point Source Catalog (`-c tmc`). The `-p` command sets the plate scale, appropriate for the KPNO 2.1 meter telescope plus the SQUID detector, at 0.68 arcseconds per pixel. And the command `-w` writes the relationship between image pixel to sky coordinates in the header of a new image.

A.3 Photometry

This section details the technical steps used to perform photometry on each of the images as outlined in Section 2.3.2. First I used the IRAF task `imexamine` to find the seeing in each image. This is done using the interactive display for `imexamine` — locate point sources and type `a` while the cursor is over an object to see a measure of the width (FWHM) of the point-spread function. I used the radial plot by typing `r`, and surface plot (`s`) to ensure that each measurement was from an object that is a point source and not saturated. I took the average FWHM from ~ 10 point sources spread across an image and used this to find seeing for that image, $\text{seeing} = 2 \times \text{FWHM}$.

SExtractor software was used to find the aperture magnitude for all objects in each image (see the manual² for full details). The input file for SExtractor requires the user to define the gain of the detector, the plate scale, and seeing for each image. I chose an aperture size of twice seeing. Using the catalog files output by SExtractor, I chose point sources — sources that were classified by SExtractor as < 0.85 on the star-galaxy scale

²<http://www.astromatic.net/software/sextractor>

(0=galaxy 1=star). I matched point sources in my images to those with calibrated magnitudes in the 2MASS catalog using the sky coordinates. From this matched catalog, I eliminated the quasar if it happened to have a measurement in 2MASS since quasars are known to vary in brightness. I also eliminated any object that was fainter than the quasar, objects that were extended, saturated, close to the edge of the image, or close to another object. Once these cuts were made, I calculated the difference or offset between the 2MASS magnitude and the magnitude measured in my image for each object. I calculated an average offset and standard deviation, σ . Any object with an offset $> 2\sigma$ was eliminated from the catalog. This final cut left each image with 10–20 calibration stars in the frame with the quasar. The average offset was calculated again and applied to the quasar's instrument magnitude in order to get a calibrated apparent magnitude. The error in apparent magnitude was calculated by adding in quadrature the measurement error from SExtractor for the quasar and each of the calibration stars.

Bibliography

Mink, D. J. 1999, in *Astronomical Society of the Pacific Conference Series*, Vol. 172, *Astronomical Data Analysis Software and Systems VIII*, ed. D. M. Mehringer, R. L. Plante, & D. A. Roberts, 498. <http://tdc-www.harvard.edu/software/wcstools/>

Appendix B

Type 1 AGN Spectra

AGN are classified as Type 1 if the broad line region is observed in optical spectra in the form of Doppler broadened emission lines. Because the emission lines are broadened due to orbital motion of gas clouds around the central black hole, the spectra of Type 1 AGN are commonly used to estimate the mass of the black hole. In this Appendix, I describe the steps used in Chapter 3 to process spectra and measure quantities needed for the black-hole mass estimate.

B.1 Flux Calibration

Several of the spectra discussed in Chapter 3 were only relative flux calibrated; i.e. instrument and sky noise were accounted for but the scale of the flux is unknown. I used broad-band magnitudes to calibrate these spectra. The calibration coefficient, x , is defined as

$$f_{\lambda,c} = x f_{\lambda,o}$$

where $f_{\lambda,c}$ is the calibrated flux at each wavelength and $f_{\lambda,o}$ is the relative flux of the un-calibrated spectrum at each wavelength. We find x starting with the definition of apparent magnitude:

$$x = \frac{f_c}{f_o} = 10^{(m_o - m_c)/2.5}$$

Where m_c is the calibrated apparent magnitude of the AGN in some waveband, a quantity that is easily found in the literature. The λ subscript is dropped because we are now

referring to a specific waveband. We can define the quantity m_o as

$$m_o - m_s = -2.5 \log(f_o/f_s)$$

where the s -index refers to a standard star for which an apparent magnitude measurement in the same band as the AGN and an absolute flux calibrated spectrum are available. Then the final form for x is

$$x = \frac{f_s}{f_o} 10^{(m_s - m_o)/2.5}$$

f_o and f_s are found by “observing” the flux calibrated standard star spectrum and AGN relative flux calibrated spectrum through a pseudo system — instrument plus filter — and integrating each spectrum over the waveband of interest.

$$f_s = \int_{\lambda_1}^{\lambda_2} f_{\lambda,s} d\lambda$$

and

$$f_o = \int_{\lambda_1}^{\lambda_2} f_{\lambda,o} d\lambda$$

In practice, the calibration coefficient is found using IRAF and all steps are applied to observed frame spectra since the apparent magnitude is defined as the observed brightness in a given band. I looked up apparent magnitudes for each AGN such that the waveband was close to the emission line to be used for mass estimation. A standard star was chosen if, in the literature, there was an apparent magnitude measurement in the same band and an absolute calibrated spectrum that includes the same band. The pseudo system mentioned above consists of a waveband filter curve and a spectrograph throughput curve.

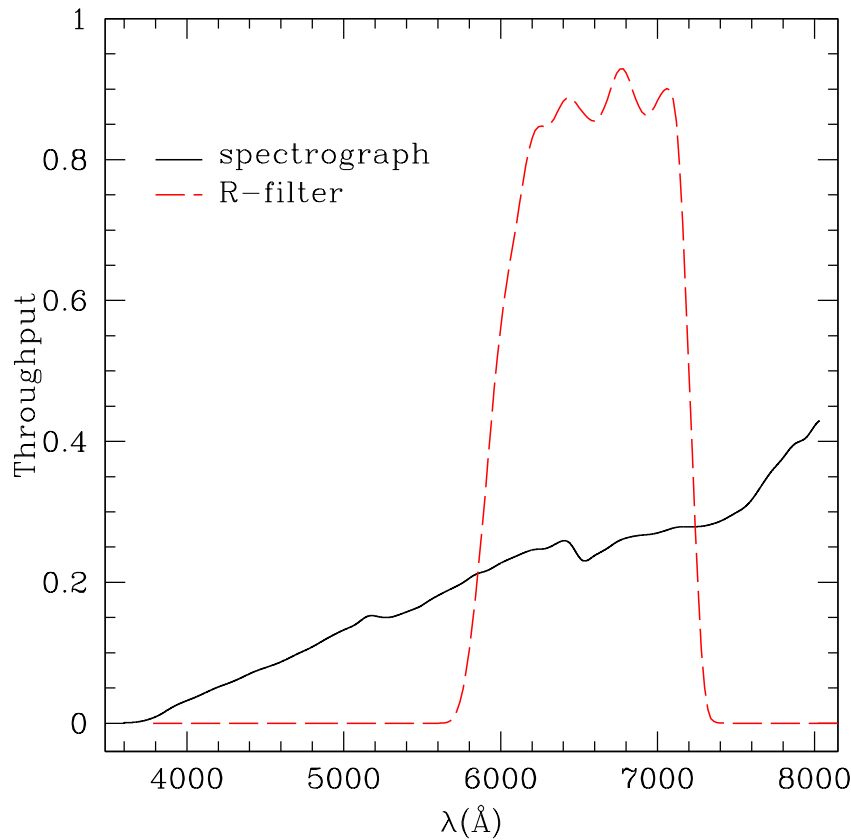


Figure B.1: **Pseudo System for Flux Calibration** — black, solid line: throughput curve for the DEIMOS (Faber et al., 2003) spectrograph (<https://www2.keck.hawaii.edu>); red, dashed line: *R*-filter response curve from Canada-France-Hawaii Telescope CFH12k’s filter (<http://www.cfht.hawaii.edu>).

Both curves are in the form of the fraction of light detected per unit wavelength – see

Figure B.1 for an example. In IRAF, open the `noao.onedspec` and `tables.ttools`

packages. Create the pseudo-system using the `sarith` task

```
> sarith {filter}.fits * {transmission}.fits {pseudo}.fits
```

Send the AGN and standard star through the pseudo-system

```
> sarith {AGNspec}.fits * {pseuso}.fits {AGNout}.fits
```

```
> sarith {STARspec}.fits * {pseuso}.fits {STARout}.fits
```

convert the output spectra to `tab` files; e.g.


```
> wspectext {AGNout}.fits {AGNout}.txt
```

```
> tcreate {AGNout}.tab columns.cd {AGNout}.txt
```

The `columns.cd` file is a list of columns, in this example `lambda` and `flux`. Integrate across the spectrum to find f_o and f_s

```
> tintegrate {AGNout}.tab flux lambda
```

will give f_o . Integrate over the `{STARout}.tab` spectrum to find f_s . These are all the parameters needed (f_s , f_o , m_s , and m_c) to calculate the calibration coefficient, x . Once x is found, the absolute flux calibrated spectrum, $f_{\lambda,c}$ or `{AGNcalib}.fits`, is produced using

```
> sarith {AGNspec}.fits * x {AGNcalib}.fits
```

B.2 Measurements

Equations 1.2, 1.3, and 1.4 show that black hole mass, $\mathcal{M} \equiv \log(M_{BH}/M_\odot)$, depends on the measurement of the width (FWHM) and luminosity of the emission line for H β and H α . Or, for MgII, \mathcal{M} depends on the width of the emission line and luminosity of the continuum at 3000Å. Section 3.4 describes the general strategy for finding these quantities as well as references with more detail. In this section, I will outline the steps to carry out the measurements in IRAF.

Prior to measuring FWHM and luminosity, I followed the techniques of Barrows (2013, sec. 5.3.3.1) to fit and subtract off broad Fe II emission lines for each spectrum. The Fe II fit also gives an initial estimate of the spectral index, α , for the continuum fit, $f \propto \lambda^{-\alpha}$. Initial estimates for emission line fits are found using the `splot` task in the `noao.onedspec` IRAF package. Once in the display terminal for `splot`, the emission line(s) of interest are fit using the `k` command for a single Gaussian or `d` to deblend several Gaussians

simultaneously. The `deblend` command is particularly useful for the $H\beta$ -[O III] and the $H\alpha$ -[N II] line groups. `splot` outputs wavelength of the peak, total flux under the line, and the FWHM of the Gaussian that is fit to the emission line — all the parameters needed to define the Gaussian. These values are used as initial parameters in the input file for a more rigorous fit task, `specfit` from the `stsdas.contrib.sffitpkg` package. Below is an example of a typical `specfit` input file that was used when fitting the $H\beta$ line. In this case, the spectrum is fit with seven components: the continuum represented as a power law, a broad $H\beta$ component, narrow $H\beta$, and the core component and blue wing for each of the [O III] lines. The power law component has two parameters: flux at 1000Å and the spectral index. The Gaussian components each have four parameters: total flux under the line, central wavelength, FWHM, and skewness. Each parameter is described in a separate line in the input file and each parameter has the following associated parameters: initial guess, lower limit, upper limit, step size, tolerance, and the fix/free parameter (see the `specfit` help page for full details).

```
begin    in_hbeta
task     specfit
components      7
                powerlaw
                gaussian
                gaussian
                gaussian
                gaussian
                gaussian
                gaussian

powerlaw1      2
0.6 0. 1000. .1 0.001 0
0.0 -10. 10. 0.01 0.001 0

#Hb (4862) -----
# broad
```

```

gaussian2          4
25. 10. 400. 0.1 0.001 0
4866. 4830. 4860. 0.1 0.001 0
2000. 400. 8000. .5 0.001 0
1. 1. 1. 0.1 0.001 -1
# narrow
gaussian3          4
5. 1. 1000. 0.1 0.001 0
4863. 4858. 4868. 0.1 0.001 0
400. 10. 3000. .1 0.001 0
1. 1. 1. 0.1 0.001 -1

#OIII 5007 -----
#blue wing
gaussian4          4
12. 1. 1000. 0.1 0.001 0
5002. 4997. 5006. 0.1 0.001 0
1000. 10. 1500 0.5 0.001 0
1. 1. 1. 0.1 0.001 -1
#core
gaussian5          4
8. 1. 1000. 0.1 0.001 0
5010. 5006. 5012. 0.1 0.001 0
376. 10. 1500. 0.1 0.001 0
1. 1. 1. 0.1 0.001 -1

#OIII 4959 -----
#blue wing
gaussian6          4
4. 1. 1000. 0.33333 0.001 4
4955. 4951. 4956. 0.9904267 0.001 4
783. 10. 1000. 1.0 0.001 4
1. 1. 1. 0.1 0.001 -1
#core
gaussian7          4
5. 1. 1000. 0.33333 0.001 5
4960. 4955. 4962. 0.9904267 0.001 5
420. 10. 1500. 1.0 0.001 5
1. 1. 1. 0.1 0.001 -1

```

I assumed skewness = 1 (symmetric) for all Gaussian fits and instead addressed asymmetries in the emission lines by fitting multiple Gaussians. Note that FWHM is reported in units of Å in `splot` but `specfit` requires units of km/s. To convert FWHM to a velocity, use the definition of a Doppler redshift

$$z = \frac{\Delta\lambda}{\lambda_o} = \frac{\text{FWHM}}{\lambda_o}$$

where $\Delta\lambda$ is the amount the wavelength of light is shifted from the theoretical value and λ_o is the central wavelength (theoretical value) of the emission line. For non-relativistic speeds $z = v/c$ where c is the speed of light. Then the width in km/s is

$$v = c \frac{\text{FWHM}}{\lambda_o}$$

I used the interactive mode in `specfit` in order to visually confirm the best fit. See Figure B.2 for an example of a spectrum and the fit found from `specfit`.

The output of `specfit` includes the best fit to each of the parameter components as well as standard deviation error for each. If a single broad Gaussian is fit to the emission line, the FWHM of that fit may be directly input in the mass calculation. However for multiple broad components of a single emission line, the FWHM is found by adding in quadrature the FWHM of each broad component. For \mathcal{M} calculated with H β and H α , the luminosity of the broad emission line is needed. Total flux of the broadened line, F , and the luminosity distance, D_L , are used to calculate luminosity.

$$L = (4\pi D_L^2)F \tag{B.1}$$

Luminosity distance is defined by redshift and cosmological parameters that describe the

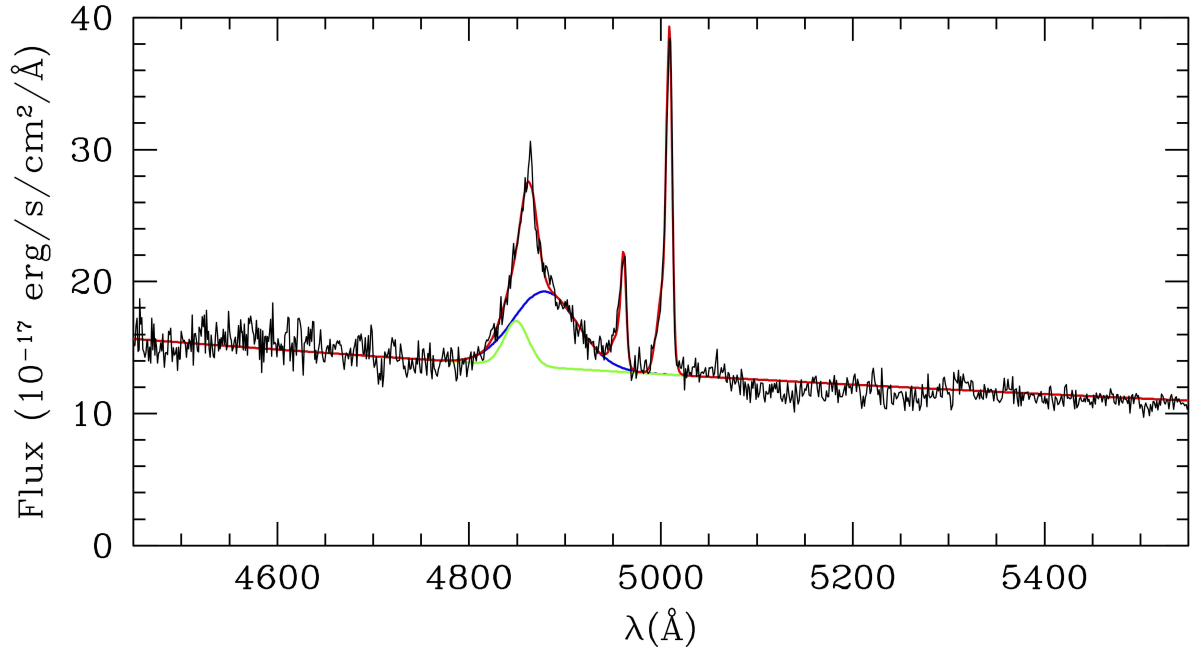


Figure B.2: **Continuum plus emission line fit** — The spectrum data is in black, total model fit in red (continuum, two broad $H\beta$ Gaussians, one narrow $H\beta$, and two Gaussians for each of the $[O\ III]$ lines), and, for emphasis, the two broad $H\beta$ components are plotted separately in blue and green.

shape of the universe (see Hogg, 1999, eqn. 20). The luminosity is found in the same way for \mathcal{M} calculated with MgII except that the flux is taken from a specific continuum wavelength, 3000\AA . I used the continuum power-law fit from `specfit` to find flux at this wavelength.

B.3 Error Propagation

There are two sources for measurement errors — emission line width (FWHM) and luminosity errors — that must be propagated in order to find total measurement error in \mathcal{M} . If the emission line was fit with a single Gaussian, the error from that fit is used

directly for FWHM. However for multiple Gaussian components, the error in FWHM, δ_W ,

$$\delta_W = \sqrt{\frac{W_1^2 \delta_{W,1}^2 + \dots + W_n^2 \delta_{W,n}^2}{W_1^2 + \dots + W_n^2}}$$

where n is the number of Gaussians used in the fit and W_i and $\delta_{W,i}$ are the FWHM and error respectively of each Gaussian. The measurement error in luminosity is found from the error in flux. From Equation B.1 the error in luminosity, δ_L , is

$$\delta_L = (4\pi D_L) \delta_F$$

Since the width and luminosity are independent of each other, we can express the error in the mass calculation (Ku, 1966) as

$$\delta_{\mathcal{M}} = \sqrt{\left(\delta_W \frac{\partial \mathcal{M}}{\partial W}\right)^2 + \left(\delta_L \frac{\partial \mathcal{M}}{\partial L}\right)^2} \quad (\text{B.2})$$

where W is the FWHM of the emission line, L is the luminosity, and δ_W and δ_L are the fit errors for FWHM and L respectively. For mass calculated using the H β emission line,

Equation 1.2,

$$\begin{aligned} \frac{\partial \mathcal{M}_{\text{H}\beta}}{\partial W_{\text{H}\beta}} &= \frac{\partial}{\partial W_{\text{H}\beta}} \left[\log \left\{ \left(\frac{W_{\text{H}\beta}}{1000 \text{km/s}} \right)^2 \left(\frac{L_{\text{H}\beta}}{10^{44} \text{ergs/s}} \right)^{0.50} \right\} + 6.67 \right] \\ &= \frac{\partial}{\partial W_{\text{H}\beta}} \left[\frac{1}{\ln(10)} \ln \left\{ \left(\frac{W_{\text{H}\beta}}{1000 \text{km/s}} \right)^2 \left(\frac{L_{\text{H}\beta}}{10^{44} \text{ergs/s}} \right)^{0.50} \right\} \right] \\ &= \frac{1}{\ln(10)} \times \frac{2}{W_{\text{H}\beta}} \end{aligned} \quad (\text{B.3})$$

and

$$\frac{\partial \mathcal{M}}{\partial L_{\text{H}\beta}} = \frac{1}{\ln(10)} \times \frac{0.50}{L_{\text{H}\beta}} \quad (\text{B.4})$$

And plugging Equations B.3 and B.4 into B.2,

$$\delta_{\mathcal{M},\text{H}\beta} = \frac{1}{\ln(10)} \sqrt{\left(\frac{2 \cdot \delta_{W,\text{H}\beta}}{W_{\text{H}\beta}}\right)^2 + \left(\frac{0.50 \cdot \delta_{L,\text{H}\beta}}{L_{\text{H}\beta}}\right)^2}$$

Similarly for \mathcal{M} using $\text{H}\alpha$ and MgII , the propagation of measurement error results in

$$\delta_{\mathcal{M},\text{H}\alpha} = \frac{1}{\ln(10)} \sqrt{\left(\frac{2.06 \cdot \delta_{W,\text{H}\alpha}}{W_{\text{H}\alpha}}\right)^2 + \left(\frac{0.55 \cdot \delta_{L,\text{H}\alpha}}{L_{\text{H}\alpha}}\right)^2}$$

and

$$\delta_{\mathcal{M},\text{MgII}} = \frac{1}{\ln(10)} \sqrt{\left(\frac{2 \cdot \delta_{W,\text{MgII}}}{W_{\text{MgII}}}\right)^2 + \left(\frac{0.47 \cdot \delta_{L,\text{MgII}}}{L_{\text{MgII}}}\right)^2}$$

Bibliography

Barrows, R. S. 2013, PhD thesis, University of Arkansas.

<http://scholarworks.uark.edu/etd/691/>

Faber, S. M., Phillips, A. C., Kibrick, R. I., et al. 2003, in Proc SPIE, Vol. 4841, Instrument Design and Performance for Optical/Infrared Ground-based Telescopes, ed. M. Iye & A. F. M. Moorwood, 1657–1669

Hogg, D. W. 1999, ArXiv Astrophysics e-prints, astro-ph/9905116

Ku, H. 1966, Journal of Research of the National Bureau of Standards C, 70C, 263.

<http://dx.doi.org/10.6028/jres.070C.025>